**Title**

Label Free Isolation and Molecular Analysis of Circulating Tumor Cells

**Author**

Dhar, Manjima

**Publication Date**

2017

UNIVERSITY OF CALIFORNIA

Los Angeles

# Label Free Isolation and Molecular Analysis of Circulating Tumor Cells

A dissertation submitted in partial satisfaction of the

requirements for the degree Doctor of Philosophy

in Bioengineering

By

Manjima Dhar

2017

# ABSTRACT OF THE DISSERTATION

## Label Free Isolation and Molecular Analysis of Circulating Tumor Cells

by

Manjima Dhar

Doctor of Philosophy in Bioengineering

University of California, Los Angeles, 2017

Professor Dino Di Carlo, Chair

Circulating Tumor Cells (CTCs) are important biomarkers for monitoring tumor dynamics and efficacy of cancer therapy. When these cells disseminate from tumors and enter the blood stream, they carry the tumor's genetic and proteomic information. They are particularly attractive because they can be obtained in a minimally invasive manner. Using microfluidic devices, we can isolate these rare cells from the background of blood cells. Here we study clinically relevant use cases of these CTCs. We characterize two aspects of CTCs: i) the PD-L1 expression levels on CTCs from non-small cell lung cancer patients undergoing immunotherapy ii) the secretion of proteases as it relates to cancer metastasis.

In the process of molecular profiling the CTCs, we use a novel label free Vortex isolation system. A modification to the original Vortex device enabled us to capture a wider size range of CTCs at a higher capture efficiency, uncovering further heterogeneity. This simple biophysical method opens doors for a range of downstream analysis.

After CTC isolation, we test the hypothesis that tumor cells secrete proteolytic enzymes to facilitate tissue invasion and spread. Given recent work suggesting CTCs can be produced by early stage tumors, MMP production by CTCs could provide a more precise biomarker of the level of metastatic activity for the disease beyond a simple CTC count. We developed a unique integrated microfluidic system able to perform three functions:

i) Isolate CTCs rapidly by size.
ii) Exchange the fluid around CTCs to both remove contaminants, and introduce a fluorogenic MMP-substrate.
iii) Encapsulate purified CTCs into a small number of microdroplets to interrogate MMPs secreted at the single-CTC level.

Total analysis from blood input to secretion assay takes minutes and preserves viability, making this system compatible with studying live cells while they retain physiologic conditions. We found that isolated CTCs from metastatic prostate cancer patients, identified through surface markers and nucleus size, release active MMPs. Assaying protease activity of circulating tumor cells will ultimately be important in uncovering the

biology of metastasis and serve as a key component of future phenotypic liquid biopsies, potentially enabling companion diagnostics for MMP inhibitor therapies currently in clinical trials.

The dissertation of Manjima Dhar is approved.

Amy Catherine Rowat

Michael Alan Teitell

Steven M Dubinett

Dino Di Carlo, Committee Chair

University of California Los Angeles

2017

# DEDICATION

This work is dedicated to Mum and Baba - the best parents a girl can ask for. You were my first teachers and my first inspiration. You lit the fire of curiosity within me, taught me how to work with dedication and passion and always had unwavering love and support.

# TABLE OF CONTENTS

# LIST OF FIGURES

# LIST OF TABLES

# ACKNOWLEDGEMENTS

Chapter 2 is adapted from “High efficiency vortex trapping of circulating tumor cells”. Biomicrofluidics 9, 64116 (2015). doi: 10.1063/1.4937895]. MD, JW, AK, CR performed experiments and analyzed data. JC and MT aided in experimental set up and data analysis. EBG, JWG, MR, MM, SSJ provided patient samples. MD, DD prepared the manuscript. SSJ, RPK, ES, DD provided guidance throughout the work and manuscript.

Chapter 3 is adapted from “Label-free enumeration, collection and downstream cytological and cytogenetic analysis of circulating tumor cells”. Scientific Reports (2016). doi:10.1038/srep35474. MD, EP, CR, DEG, performed experiments, analyzed data, and prepared the manuscript. JC, RM, RC, KH, MT aided in analyzing data. MM, JR, SSJ, EBG, JWG, NPR provided patient samples. MD, EP, ES prepared the manuscript. RPK, ES, DD provided guidance throughout the work and manuscript.

Chapter 4 is adapted from a manuscript in review “Evaluation of PD-L1 expression on vortex-isolated circulating tumor cells in metastatic lung cancer”. Scientific Reports 2017. MD, JW, JC performed experiments and analysis. MM, EBG, JWG, provided patient samples. TG. DE helped with analysis. MD, RPK, ES prepared the manuscript. RPK, DD provided guidance throughout the work and manuscript.

This work was supported by funding from the National Institutes of Health Innovative Molecular Analysis Technologies Program, and a sponsored research grant with NetScientific.

Additional acknowledgements:

I am most grateful to my advisor Dino Di Carlo for giving me the opportunity to be part of his lab. He has always been encouraging and very supportive. Many thanks to all of my labmates for their helpful discussions, advice and friendship. I want to recognize two undergraduate students Jessica Wong and Jeffrey Lam who immensely helped with this work and helped me grow as a mentor. Finally, thanks to my partner in life Manas, for always believing in me and keeping me sane outside of lab.

# VITA

EDUCATION

B.S. in Biomedical Engineering (2013), Johns Hopkins University, Baltimore, MD

RESEARCH APPOINTMENTS

Graduate Student Researcher (2013-2017), University of California, Los Angeles

Professor Dino Di Carlo, Department of Bioengineering

Undergraduate Research Assistant (2011-2013), Johns Hopkins University

Professor Aleksander Popel, Department of Biomedical Engineering

Instructor (2013-2017)

CNSI High School Nanoscience Program

# PUBLICATIONS

- *(In Progress)* Dhar M, Lam N J, Rettig M, Di Carlo D. *Functional profiling of circulating tumor cells with an integrated vortex capture and single-cell protease activity assay.*
- *(In Review)* Dhar M, Di Carlo D, Kulkarni RP. *Evaluation of PD-L1 expression on vortex-isolated circulating tumor cells in metastatic lung cancer.* Scientific Reports, 2017.
- Dhar M, Di Carlo D et al. *Label-free enumeration, collection and downstream*

*cytological and cytogenetic analysis of circulating tumor cells.* Scientific Reports, 2016.

- Dhar M, Di Carlo D, et al., *High efficiency vortex trapping of circulating tumor cells.* Biomicrofluidics, 2015.
- Che J, Yu V, Dhar M, Di Carlo D et al. *Classification of large circulating tumor cells isolated with ultra-high throughput microfluidic Vortex technology*. Oncotarget, 2016.
- Lin J, Kim D, Tse Henry, Tseng P, Peng L, Dhar M, and Karumbayaram S, Di Carlo D. High-throughput physical phenotyping of cell differentiation. Microsystems and Nanoengineering 2016.
- Finley SD, Dhar M, Popel AS. *Compartment model predicts VEGF secretion and investigates the effects of VEGF Trap in tumor-bearing mice*. Frontiers in Oncology, 2013.
- Tay AK, Dhar M, Pushkarsky I, Di Carlo D. *Research highlights: manipulating cells inside and out.* Lab on a Chip 2015.
- Kulkarni R, Che J, Dhar M and Di Carlo, D. *Research highlights: microfluidic single-cell analysis from nucleic acids to proteins to functions*. Lab on a Chip, 2014.
- Weaver W, Kittur H, Dhar M and Di Carlo D. *Research highlights: microfluidic point-of-care diagnostics*. Lab on a Chip, 2014.

# Chapter 1. Liquid Biopsy

Almost 150 years ago Australian physician Thomas Ashworth had first recorded observation of Circulating Tumor Cells (CTCs) in blood taken from the leg of a cancer patient. His observation that these cells are morphologically similar to the primary tumor laid the foundation for the burgeoning field of assays we now know as Liquid Biopsies. New technologies evolved which substantiated Ashworth's observations that CTCs which dislodge from the primary tumor site and enter blood circulation harbor genomic and proteomic similarity to primary and tertiary tumors. Today we glean further information from these cells to better understand cancer metastasis and move towards personalized medicine and systematic treatment monitoring.

The clinical relevance of CTCs has become evident from comparative studies to primary tumors. Companies such as Guardant Health has established similarities in gene alteration patterns between CTC DNA and tumor DNA. Some drugs are effective only in the presence of specific mutations such as EGFR and MET for lung cancer, and KRAS PIK3CA for breast cancer. Clinical trials on drugs such as gefitinib, erlotinib, pembrolizumab have shown greater efficacy in patients with such oncogeneic mutations [1]. Ideally a non-invasive method to profile the tumor cells would allow for continuous monitoring and help cases where tumors are not accessible or too dangerous to biopsy. The growing interest in liquid biopsy has led several groups to show that ctDNA and CTCs harbor some of these tumor specific druggable mutations, EGFR and MET in lung cancer patients.[2,3] Pre-treatment knowledge of the mutations would allow better treatment regimens, and monitoring mutations during and after treatment can help assess development of drug resistance.

Beyond looking at genomic information, assaying functional behaviors of CTCs can give us information ranging from metastatic state of the cancer to drug susceptibility. Under diseased conditions blood may contain aberrant levels of Circulating Tumor Cells (CTCs), endothelial cells, and stem cells. The measurable phenotypes of these blood components contain clinically relevant information on metastatic state of cancer. For example, CTCs exhibit higher deformability and decrease expression of cell-adhesion molecules which promote higher motility for metastasis[4–7]. Here we add CTC secretions to the measurable phenotypes. Since CTCs dislodge from various parts of the tumor or separate metastatic sites and can contain intra and inter tumor heterogeneity it is important to interrogate them at a single cell resolution. By quantifying the heterogeneous protein expression on single CTCs, we achieve a better understanding of the breath of the behavior of metastatic tumor cells.

## 1.1. Circulating tumor cells and metastasis

The process of metastasis consists of the following steps: i) Cells from the primary tumor detach from the surrounding cells by reducing their cell-to-cell adhesion.[8] ii) These cells traverse through the basement membrane and ECM fibers- collagen, elastin, proteoglycan and laminins[9] iii) squeeze between the endothelial cells and into the blood stream or lymphatic vessels. The second phase of the process requires the CTCs to degrade the ECM to pave its way to the blood vessel. Cell-secreted proteolytic enzymes that cleave extracellular matrix (ECM) proteins are implicated in cancer invasion of neighboring tissues and metastasis. For example, immunohistochemistry of invasive tumors has shown high levels of MMP2, MMP9, MMP13, MT-1[10–13].

Although these studies show the presence of MMPs, it is not necessarily informative regarding their functional state. MMPs initially exist in an inactive form. The interaction of several types of proteases leads to MMP activation and ECM degradation[14]. Investigating the state of the ultimate secreted product from these tumor cells and cells that escape the tumors would lead to better understanding of metastasis. Analysis of metastatic tumors and patient blood serum has shown significantly higher levels of matrix metalloproteases (MMPs), suggesting that CTCs may also release MMPs that allow them to degrade the ECM, and that the level of MMPs produced by CTCs could serve as a functional marker of cells that have metastasis-enabling properties. Specifically, MMP 2 and 9 are upregulated in several types of cancers [10,12,15–18]. Some work on new generations of allosteric MMP inhibitors suggest targeting this activity may be a good avenue for anti-metastasis drugs [19,20].

Liquid Biopsies show promise as a tool for studying primary and metastatic tumors. CTCs provide a noninvasive way to track the evolution of genetic and molecular changes as well as phenotype in tumor cells before, during and after therapy to understand tumor evolution or select the most effective treatment strategies. However, the low concentration of CTCs in blood for some patients (~1-

100 CTCs/ml)[21–23] introduces challenges in isolating them from a background of millions of leukocytes and billions of erythrocytes

## 1.2. Liquid biopsy technologies

Technologies that isolate CTCs must overcome the challenge of processing large volumes of blood quickly and concentrate these rare cells into manageable volumes for downstream analysis. Several cellular characteristics have been used to differentiate CTCs from leukocytes including surface protein expression, cell size, electrical properties, and cell deformability.[24]

## 1.3. Immuno-affinity based isolation

Surface markers are used to target either CTCs for positive selection or leukocytes for negative depletion.[23,25–28] In particular, the epithelial surface marker, epithelial cell adhesion molecule (EpCAM), and cytokeratin (CK) have been targeted in surface antigen-based CTC isolation and enumeration respectively. Magnetic beads conjugated to antibodies targeting surface markers are used by the CellSearch semi-automated system, Adnagen and Isoflux.[25–27] Similar concepts have been applied to coat microfluidic device walls, micropillars, and nanotubes with anti-EpCAM antibodies.[29–31] Surface marker-based capture must be tuned to the cancer type, especially since not all cancer types and CTCs have significant EpCAM expression.[32,33] To further improve capture efficiency, cocktails of antibodies targeted towards a range of surface markers can be used. However, antigen-based capture often yields difficulty in integrating with downstream assays as cells remain attached to surfaces or beads and purity may be lower due to non-specific binding. Surface expression based cell capture also limits the captured cells to only those expressing epithelial proteins, and it will miss the cells that have gone through Epithelial to Mesenchymal Transformation.

## 1.4. Physical filtration

Label free isolation techniques broaden the range of CTCs collected by removing the surface marker bias. Though size based isolation introduces a cell size bias it is possible to control the size cut off range. These label-free technologies include micro-filters, acoustophoresis, and dielectrophoresis. Some of these technologies have limited throughput and/or require pre-processing steps such as red blood cell-lysis or cell fixation, and/or often possess high level of contamination with leukocytes.[34–38] Such limitations prevent facile analysis of the CTCs for clinical information downstream.

### 1.4.1. Size based microfiltration

One of the label-free technologies that rely on the size and deformability difference between large CTCs and small blood cells is microfiltration. Microfabricated filters such as ISET (Isolation by Size of Tumor cells) and Parsortrix. Both use small microfabricated pores that allow small blood cells to pass through, and trap large CTCs.[37,39,40] The pore clogging issues and cell loss associated with ISET devices led to the modified filters or resettable traps by Beattie et al. These new filters can be manipulated to release the trapped cell periodically to prevent clogging. However the throughput for these devices decays to approximately 1ml per hour.[41] Additionally, removing the CTCs stuck to the filters remain a challenge, making downstream analysis difficult.

### 1.4.2. Acoustophoresis and Dielectrophoresis

The response of CTCs to external electrical and acoustic forces can be used to trap or manipulate them. In acoustophoresis, a pressure wave within a microchannel can deflect cell trajectories based on their size, compressibility and density. The differentiating acoustic force factor amongst CTCs and the background of WBCs and RBCs is cell size. Large cells migrate towards low pressure nodes positioned towards the center of the channel, while small cells do not migrate transversely, and can be directly towards side waste channels. The acoustic force is inversely proportional to the sample throughput; which necessitates low throughput for high efficiencies.[34,42] The differentiation between background blood cells and CTCs is low, therefore these systems require RBC lysis to increase yields. These preprocessing steps increase assay time and reduce probability of cells maintaining their physiologic condition.

The second external force that can control cell isolation is dielectrophoresis. When cells are in a nonuniform electric field, the charged ions inside cells polarize such that they are attracted towards regions of high density fields. The cell trapping is frequency dependent. However the frequency differential between CTCs and blood cells is low and thus require RBC lysis for high efficiency CTC capture.[43,44]

### 1.4.3. Size-based cell separation using inertial forces

More recently, size- and deformability-based isolation of CTCs has been demonstrated using continuous separation which relies on inertial lift forces.[21,45,46] These technologies rely solely on microchannel geometry and do not require external electric or acoustic forces. In these devices, high Reynolds numbers coupled with various channel geometries lead to inertial forces that guide large and small cell populations such that each size focuses at different locations within the microchannel cross-section, where they can be selectively collected in separate outlets. Based on the channel geometry, smaller blood cells can focus near the channel side walls while larger CTCs focus closer to the center.[47] When combining with curving channels, cells focus faster at various lateral positions in the channel cross-section. Notably, these techniques maintain high efficiency capture and viability of cells. However, these devices still suffer from low purity and, because of the continuous flow extraction of CTCs from the diluted blood, often require additional concentration steps to be compatible with downstream assay volumes.

## 1.5. References

1. Tu, M., Chia, D., Wei, F. & Wong, D. Liquid biopsy for detection of actionable oncogenic mutations in human cancers and electric field induced release and measurement liquid biopsy (eLB). *Analyst* **141,** 393–402 (2016).

2. Shaw, J. A. *et al.* Mutation Analysis of Cell-Free DNA and Single Circulating Tumor Cells in Metastatic Breast Cancer Patients with High Circulating Tumor Cell Counts. *Clin. Cancer Res.* **23,** (2017).

3. Yanagita, M. *et al.* A Prospective Evaluation of Circulating Tumor Cells and Cell-Free DNA in EGFR-Mutant Non–Small Cell Lung Cancer Patients Treated with Erlotinib on a Phase II Trial. *Clin. Cancer Res.* **22,** (2016).

4. Tse, H. T. K. *et al.* Quantitative Diagnosis of Malignant Pleural Effusions by Single-Cell Mechanophenotyping. *Sci. Transl. Med.* **5,** (2013).

5. Che, J. *et al.* Biophysical isolation and identification of circulating tumor cells. *Lab Chip* **17,** 1452–1461 (2017).

6. Nakajima, S. *et al.* N-Cadherin Expression and Epithelial-Mesenchymal Transition in Pancreatic Carcinoma. *Clin. Cancer Res.* **10,** 4125–4133 (2004).

7. Hazan, R. B., Phillips, G. R., Qiao, R. F., Norton, L. & Aaronson, S. A. Exogenous expression of N-cadherin in breast cancer cells induces cell migration, invasion, and metastasis. *J. Cell Biol.* **148,** 779–90 (2000).

8. Tran, N. L., Nagle, R. B., Cress, A. E. & Heimark, R. L. N-Cadherin expression in human prostate carcinoma cell lines. An epithelial-mesenchymal transformation

mediating adhesion withStromal cells. *Am. J. Pathol.* **155,** 787–98 (1999).

9. Ra, H.-J. & Parks, W. C. Control of matrix metalloproteinase catalytic activity. *Matrix Biol.* **26,** 587–96 (2007).

10. Groblewska, M. *et al.* Serum levels and tissue expression of matrix metalloproteinase 2 (MMP-2) and tissue inhibitor of metalloproteinases 2 (TIMP-2) in colorectal cancer patients. *Tumour Biol.* **35,** 3793–802 (2014).

11. Upadhyay, J. *et al.* Membrane type 1-matrix metalloproteinase (MT1-MMP) and MMP-2 immunolocalization in human prostate: change in cellular localization associated with high-grade prostatic intraepithelial neoplasia. *Clin. Cancer Res.* **5,** 4105–10 (1999).

12. Zhang, B. *et al.* Tumor-derived matrix metalloproteinase-13 (MMP-13) correlates with poor prognoses of invasive breast cancer. *BMC Cancer* **8,** 83 (2008).

13. Kallakury, B. V *et al.* Increased expression of matrix metalloproteinases 2 and 9 and tissue inhibitors of metalloproteinases 1 and 2 correlate with poor prognostic variables in renal cell carcinoma. *Clin. Cancer Res.* **7,** 3113–9 (2001).

14. Egeblad, M. & Werb, Z. New functions for the matrix metalloproteinases in cancer progression. *Nat. Rev. Cancer* **2,** 161–174 (2002).

15. Gondi, C. S. & Rao, J. S. Cathepsin B as a cancer target. *Expert Opin. Ther. Targets* **17,** 281–91 (2013).

16. Westermarck, J. & Kähäri, V. M. Regulation of matrix metalloproteinase expression in tumor invasion. *FASEB J.* **13,** 781–92 (1999).

17. Safranek, J. *et al.* Expression of MMP-7, MMP-9, TIMP-1 and TIMP-2 mRNA in lung tissue of patients with non-small cell lung cancer (NSCLC) and benign pulmonary disease. *Anticancer Res.* **29,** 2513–2517 (2009).

18. Kim, Y. H., Kwon, H.-J. & Kim, D.-S. Matrix metalloproteinase 9 (MMP-9)-dependent processing of βig-h3 protein regulates cell migration, invasion, and adhesion. *J. Biol. Chem.* **287,** 38957–69 (2012).

19. Manish A. Shah, Alexander Starodub, Zev A. Wainberg, Meihua Wu, Victoria Smith, Julia D. Maltzman, J. C. B. Results of a phase I study of GS-5745 in combination with mFOLFOX in patients with advanced unresectable gastric / GE junction tumors. | 2016 ASCO Annual Meeting | Abstracts | Meeting Library. *2016 ASCO Annu. Meet.* (2016).

20. Marshall, D. C. *et al.* Selective Allosteric Inhibition of MMP9 Is Efficacious in Preclinical Models of Ulcerative Colitis and Colorectal Cancer. *PLoS One* **10,** e0127063 (2015).

21. Hou, H. W. *et al.* Isolation and retrieval of circulating tumor cells using centrifugal forces. *Sci. Rep.* **3,** 1259 (2013).

22. Hosokawa, M. *et al.* Size-Based Isolation of Circulating Tumor Cells in Lung Cancer Patients Using a Microcavity Array System. *PLoS One* **8,** e67466 (2013).

23. Ozkumur, E. *et al.* Inertial focusing for tumor antigen-dependent and -independent sorting of rare circulating tumor cells. *Sci. Transl. Med.* **5,** 179ra47 (2013).

24. Chen, Y. *et al.* Rare cell isolation and analysis in microfluidics. *Lab Chip* **14,** 626–

45 (2014).

25. Riethdorf, S. *et al.* Detection of circulating tumor cells in peripheral blood of patients with metastatic breast cancer: A validation study of the CellSearch system. *Clin. Cancer Res.* **13,** 920–928 (2007).

26. Andreopoulou, E. *et al.* Comparison of assay methods for detection of circulating tumor cells in metastatic breast cancer: AdnaGen AdnaTest BreastCancer Select/Detect$^{TM}$ versus Veridex CellSearch$^{TM}$ system. *Int. J. Cancer* **130,** 1590–1597 (2012).

27. Alva, A. *et al.* Circulating Tumor Cells as Potential Biomarkers in Bladder Cancer. *J. Urol.* **194,** 1–9 (2015).

28. Casavant, B. P. *et al.* A negative selection methodology using a microfluidic platform for the isolation and enumeration of circulating tumor cells. *Methods* **64,** 137–43 (2013).

29. Stott, S. L. *et al.* Isolation of circulating tumor cells using a microvortex-generating herringbone-chip. *Proc. Natl. Acad. Sci. U. S. A.* **107,** 18392–18397 (2010).

30. Shao, N., Wickstrom, E. & Panchapakesan, B. Nanotube-antibody biosensor arrays for the detection of circulating breast cancer cells. *Nanotechnology* **19,** 465101 (2008).

31. Wang, S. *et al.* Highly efficient capture of circulating tumor cells by using nanostructured silicon substrates with integrated chaotic micromixers. *Angew. Chemie - Int. Ed.* **50,** 3084–3088 (2011).

32. Gorges, T. M. *et al.* Circulating tumour cells escape from EpCAM-based detection due to epithelial-to-mesenchymal transition. *BMC Cancer* **12,** 178 (2012).

33. Bai, L. *et al.* Peptide-based isolation of circulating tumor cells by magnetic nanoparticles. *J. Mater. Chem. B* **2,** 4080 (2014).

34. Li, P. *et al.* Acoustic separation of circulating tumor cells. *Proc. Natl. Acad. Sci. U. S. A.* **112,** 4970–4975 (2015).

35. Zheng, S. *et al.* Membrane microfilter device for selective capture, electrolysis and genomic analysis of human circulating tumor cells. *J. Chromatogr. A* **1162,** 154–161 (2007).

36. Gascoyne, P. R. C. & Shim, S. Isolation of circulating tumor cells by dielectrophoresis. *Cancers (Basel).* **6,** 545–579 (2014).

37. Vona, G. *et al.* Isolation by Size of Epithelial Tumor Cells, A New Method for the Immunomorphological and Molecular Characterization of Circulating Tumor Cells. *Am. J. Pathol.* **156,** 57–63 (2000).

38. Qin, X. *et al.* Separation of Circulating Tumor Cells from Castrate Resistant Prostate Cancer Patients using Resettable Cell Traps. *Lab Chip* **15,** 2278–2286 (2015).

39. Yusa, A. *et al.* Development of a new rapid isolation device for circulating tumor cells (CTCs) using 3D palladium filter and its application for genetic analysis. *PLoS One* **9,** (2014).

40. Chudziak, J. *et al.* Clinical evaluation of a novel microfluidic device for epitope-

independent enrichment of circulating tumour cells in patients with small cell lung cancer. (2015). doi:10.1039/C5AN02156A

41. Beattie, W., Qin, X., Wang, L. & Ma, H. Clog-free cell filtration using resettable cell traps. *Lab Chip* **14,** 2657–2665 (2014).

42. Augustsson, P., Magnusson, C., Lilja, H. & Laurell, T. Acoustophoresis in Tumor Cell Enrichment. *Circ. Tumor Cells* 227–248 (2016). doi:10.1002/9781119244554.ch10

43. Gascoyne, P. R. C., Noshari, J., Anderson, T. J. & Becker, F. F. Isolation of rare cells from cell mixtures by dielectrophoresis. *Electrophoresis* **30,** 1388–98 (2009).

44. Voldman, J. Electrical forces for microscale cell manipulation. *Annu. Rev. Biomed. Eng.* **8,** 425–54 (2006).

45. Bhagat, A. A. S., Hou, H. W., Li, L. D., Lim, C. T. & Han, J. Pinched flow coupled shear-modulated inertial microfluidics for high-throughput rare blood cell separation. *Lab Chip* **11,** 1870–1878 (2011).

46. Hur, S. C., Henderson-MacLennan, N. K., McCabe, E. R. B. & Di Carlo, D. Deformability-based cell classification and enrichment using inertial microfluidics. *Lab Chip* **11,** 912–20 (2011).

47. Amini, H., Lee, W. & Di Carlo, D. Inertial microfluidic physics. *Lab Chip* **14,** 2739–61 (2014).

# Chapter 2. High Efficiency Vortex Trapping of Circulating Tumor Cells

Trapping of larger cells in laminar microvortices has demonstrated the ability to quickly and passively enrich CTCs at high purity from a large volume of blood, and concentrate these cells in < 300μL. The Vortex Chip designed in our previous work efficiently captures cells larger than ~18μm in diameter, which is suitable to isolate many CTCs. However, this initial chip design may not trap some smaller CTCs. Many factors, including the geometry of the channels leading into the reservoirs, and the structure of the reservoirs themselves affect this size cut-off.

Here, we study the effects of channel geometry on tuning the efficiency, stability, and size cut-off for capture in the Vortex Chip – and we introduce the Vortex HE (High Efficiency) Chip. Vortex HE has higher efficiency capture for cells in a smaller size range (>12μm) than the Vortex Chip. This enables the capture of additional CTCs in patients with lung, prostate, and breast cancer. The ability to isolate a broader range of CTCs can better represent cellular diversity due to intra- and inter-tumoral heterogeneity. Capturing additional rare mutants could aid in predicting response to treatment.[1–4] Importantly, although the cut-off in particle size is reduced, the Vortex HE mechanism maintains a highly pure sample, which benefits downstream molecular analyses.

## 2.1. Theoretical background

When fluid with sufficient momentum travels through narrow entry channels that expand into large reservoirs, vortices are formed within the reservoirs. Cells that travel through the narrow entry channels migrate across fluid streamlines and into these predictable laminar microvortices (Figure 2-1). Vortex formation and structure depends on the Reynolds number (Re) of the entry channel. Here $\mathrm{Re} = \frac{\rho U D_h}{\mu}$ , and ρ, U, μ are the density, mean velocity and dynamic viscosity of the fluid respectively. $D_h$ is the hydraulic diameter of the channel, with $D_h = \frac{2WH}{W+H}$ , where W is the width and H is the height of the channel. Two components critical for vortex trapping are a high number of particles entering into the vortices (entry) and the stable maintenance of trapped particles within the vortices (stability). First, particles must laterally migrate across the mainstream flow and cross the boundary of the vortex (the separatrix), due to fluid dynamic forces. These particles can then begin to circulate within the vortex. Second, these particles must be stable and maintain an orbit over several minutes within the vortex. Perturbations in the orbit of a particle could lead the particle to follow a trajectory that again crosses the separatrix and leaves the vortex trap to go back in the main flow.

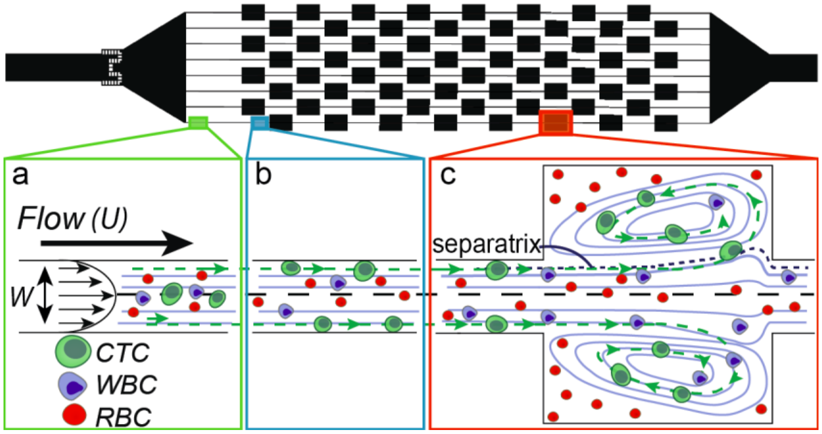

**Figure 2-1 Microfluidic device design.** The Vortex HE device has 8 reservoirs in series and 8 in parallel. a) Initially the red blood cells (RBCs), white blood cells (WBCs) and CTCs are distributed throughout the channel cross-section. b) After traveling approximately 500µm, the larger cells (CTCs) that experience higher inertial lift force migrate towards the channel walls. c) The larger CTCs located near the wall experience enough lift force to enter the reservoir and remain stably trapped, while WBC and RBCs either do not enter the reservoirs or do not remain trapped and return to the main flow.

Particle entry into reservoirs occurs due to shear-gradient lift force that acts down the parabolic profile developed in the entry channel.[5] The force scales as $F_L = \frac{f_L \rho U^2 a^3}{W}$ , when *a/W* is close to 1.[5] Here $f_L$ is the lift coefficient determined by the parabolic flow profile, $\rho$ is the density of the fluid, *U* is the maximum fluid velocity, *a* is the particle diameter, and *W* is the width of the channel in the entry region prior to the reservoir. This force directs particles to cross the separatrix and enter the reservoir, because the parabolic profile developed in the entry channel is maintained for some distance downstream in the vortex region. Smaller particles do not experience enough shear-gradient lift force, and thus do not enter the reservoirs without other inter-particle collisions or hydrodynamic disturbances leading to entry. Equation for $F_L$ indicates that we can increase the shear-gradient lift force by decreasing the channel width (*W)*, while maintaining a similar or larger flow velocity (*U*). This leads to a sharper parabolic flow profile and is expected to allow smaller particles to migrate across the separatrix as well and enter the reservoirs, where they may become stably trapped.

Once a particle enters into a reservoir, a variety of factors are expected to affect the particle stability. Inter-particle collisions or hydrodynamic interactions could disturb particles from stable orbiting streamlines within a vortex. Although hypothesized to affect trapping, no previous work has investigated the effect of background particle concentration on orbit stability and resultant effects on trapping efficiency. The volume capacity of the reservoir influences the density of the particles trapped and likelihood of inter-particle interactions. The parabolic velocity profile also decays downstream of the reservoir such that the shear gradient lift force that acts to restore trapped particles into stable orbits diminishes towards the end of the reservoir. This effect would become more pronounced when the reservoir is very long (Figure 2-2).[6]

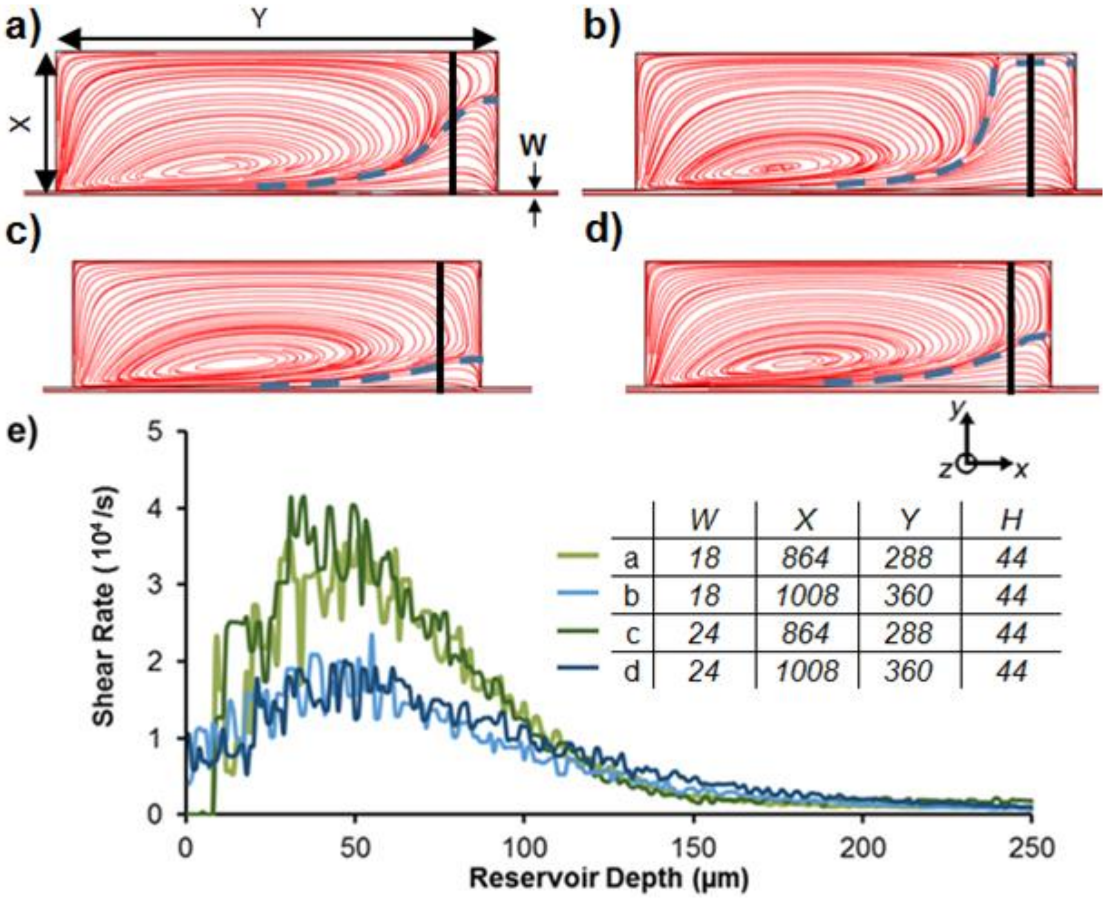

| | W | X | Y | H |
|---|---|---|---|---|
| a | 18 | 864 | 288 | 44 |
| b | 18 | 1008 | 360 | 44 |
| c | 24 | 864 | 288 | 44 |
| d | 24 | 1008 | 360 | 44 |

**Figure 2-2. Fluid dynamic differences as a function of reservoir dimensions.** a-d) A 3D COMSOL simulation of the vortex devices was performed with different channel and reservoir dimensions, while the channel height and Re were kept constant, at 44µm and 160 respectively. The largest reservoir has a longer separatrix region (highlighted by dashed blue line) which likely contributes to particle exit from orbits. e) The shear rate near the separatrix (indicated by the vertical black line at 90% of the length of the reservoir: 777µm for the 864x288 reservoir and at 907µm for the 1008x360 reservoir) decreases slightly with increasing reservoir size. The gradient of the shear rate - which corresponds to the force - also decreases with

increasing reservoir size. This occurs because the parabolic profile of the main stream decays down the reservoir, this reduces the inward force and contributes to lower capture as seen in experiments. W, Y, X, H respectively represent the channel width, reservoir width, reservoir length and device height. All units are in µm.

## 2.2. Methods

### 2.2.1. Microfluidic device fabrication

Devices were made with the polymer polydimethylsiloxane (PDMS) using replica molding. The mold structure on a silicon wafer spin coated with KMPR 1050 (Microchem) was defined using photolithography. A spin speed of 2900 rpm resulted in 44µm heights and 1700rpm for 70µm heights measured with a Dektak profilometer. The PDMS device was made with Sylgard 184 Elastomer (Dow Corning Corporation) with a cross-linker to polymer ratio of 1:10, and cured at 60°C for 21 hours. The devices were cut from the mold, and a punched using a 1.5mm TiN Coated biopsy needle. The PDMS layer and a glass slide were $O_2$ plasma treated using an Oxford Technics RIE (for 30 seconds, at 500 mTorr, 80 Watt power) before being bonded together to enclose the microchannels.

### 2.2.2. Study of particle entry mechanism into reservoirs

Polydisperse PDMS particles were made with silicone crosslinker and base polymer in a 1:10 ratio. 1ml of PDMS was mixed with 50ml of 0.01% Triton-X in DI water, to stabilize PDMS droplets while curing and to form solid beads. The mixture was shaken in a vortexer for 5 minutes. The beads were cured at 60°C for 24 hours.

PDMS particles less than 20µm were separated using a 20µm filter. Dilute polydisperse particles with a concentration of ~2500 particles per ml were infused into each device. Particle entry into reservoirs was quantified by analyzing high speed video of the particles as they entered or passed the reservoirs. The length of video analyzed was determined such that the same volume of fluid would be analyzed for each device, independent of flow rate used. Videos from six reservoirs were studied. A phantom v2010 (Vision Research) high speed camera was used at a frame rate of 9000 frames per second. A semi-automated image processing algorithm developed in MATLAB was used to find the number and size of particles that either enter or pass by the reservoir. Entry analysis was performed for 3 devices with different channel widths and similar aspect ratios (W40 and H70, W24 and H44, W18 and H44). The flow rates used for the entry study correspond to those which yielded the highest capture efficiency for each device.

### 2.2.3. Stability analysis of particle orbits

We studied the stability of particles within their orbits by tracking the motion of one 20 µm polystyrene particle in the presence of background particles consisting of healthy whole blood, diluted to various ratios. Polystyrene beads were easily tracked, even among a high background of RBCs, due to the large difference in their refractive index from the surrounding cells. Diluted healthy whole blood were used to vary the level of perturbation in the system due to particle-particle interactions. A high speed camera (Phantom V2010, Vision Research) was used to capture videos at 3300 frames per second to characterize the orbit dynamics for one 20µm bead trapped in a reservoir at a time. The plugin Mosaic Suite in ImageJ was used to track the particle trajectories.[8] A total of 250 trajectories were analyzed for 5 different reservoirs. The perturbation of the trajectories was defined by the transverse variance in the y direction of the trajectories. A cross section of the trajectories was taken as shown by the orange box in (Figure 2-3b). The set of intersections of the trajectories through one x location (shown in Figure 2-3b as a gray dashed lined) fit a Gaussian curve. The variance of the Gaussian is used to represent the variance of the trajectory and quantifies stability. The most stable trajectory would yield close to 0 variance, as shown in the graph of 0 RBCs in Figure 2-3b. The flow rates used were 2.62ml/min for the devices with W24 and 4ml/min for the devices with W40.

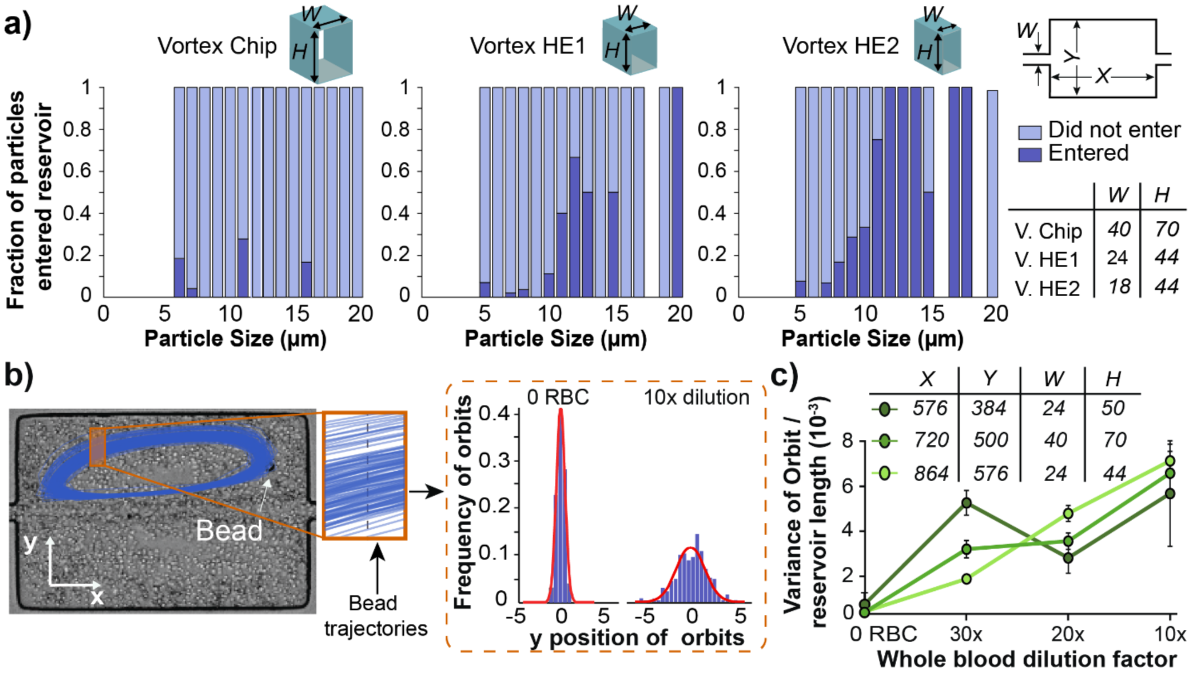

**Figure 2-3. Particle entry and orbit perturbation analysis**. a) Size distribution of particle entry depends on entry channel dimensions. The fraction of particles that enter the reservoir is the ratio between the number of particles of a particular size that entered the reservoir and the total number of particles of that size that were observed in the entry channel (dfark blue bars). The light blue bars are the fraction of particles that did not enter the reservoirs. Blank spaces indicate no particles of that size. N = 6 reservoirs were used for each device. b) Histograms of the points of intersection of a trajectory with one x position are shown. This is used to calculate a variance in intersection position which quantifies the perturbation of the trajectory from a single consistent trajectory (most stable particles having a variance of 0). c) Orbit variance analysis for 20µm beads in PBS and 3 dilutions of blood, for N = 5 reservoirs.

### 2.2.4. Cell line preparation

The non-small cell lung cancer line A549 was used to model smaller cancer cells. These cell lines ranged from 11-27µm in diameter when analyzed using brightfield imaging (Zeiss Axiovert, 10X objective) to characterize size. The prostate cancer cell line, VCaP, and breast cancer cell lines MDA-MB-231 were also used to validate vortex HE devices.. A549 cells were grown in RPMI media supplemented with 10%fetal bovine serum (FBS) and 1% penicillin-streptomycin- glutamine (P/S). MDA-MB-231 cells and VCaP cells were grown in DMEM, 10% FBS, and 1% P/S. Once the cells were semi confluent, they were lifted from their adherent layer using 0.25% Trypsin EDTA (Gibco) and 3 minutes incubation at 37°C. The trypsin was neutralized with media and cells were spun down at 2500 rpm for 4 minutes, the trypsin and media were removed and the cells were suspended back in media before processing.

### 2.2.5. Cell line spiking with PBS and blood

The vortex devices were operated using the procedure from Sollier et al.[53] For capture efficiency tests, the concentration of cells in suspension was determined using a hemocytometer, and appropriately diluted to 6000 cells per ml. Approximately 300 cells were spiked into 5ml of PBS and processed through the device to achieve a final concentration of 60 cells/ml. After collection in well plates, these cells were stained with 0.5µl of 1µg/ml of Hoechst dye dissolved in water for 15 minutes, before imaging and enumeration. In order to mimic isolation of CTCs from blood, 300 cells were spiked into 0.5 or 1ml of whole blood and diluted in PBS to 10ml total volume, for a 20x or 10x blood dilution respectively. After processing, cells were fixed with 2% paraformaldehyde (Electron Microscopy Sciences) for 10 minutes, permeabilized with 0.4% v/v Triton X-100 dissolved in DI water (Research Products International Corp) for 7 minutes, blocked with 5% Goat Serum dissolved in PBS (Invitrogen) for 10 minutes and stained with 0.005 mg/ml DAPI (Molecular Probes), 0.05 mg/ml anti-CD45-PE (BD Biosciences, HI30), 0.025 mg/ml anti-CK-FITC (BD Biosciences, clone CAM5.2), 0.025 mg/ml anti-Pan-CK-FITC (MACS Miltenyi, clone 3-6H5), and 0.025 mg/ml anti-CK -FITC (eBioscience, clone AE1/AE3) for enumeration. Clinical samples from lung cancer and breast cancer patients were also stained with 0.0002 mg/ml anti-Vimentin (Abcam, clone V9) and 0.005 mg/ml anti-N-Cadherin (Abcam, clone EPR1791-4) to evaluate EMT status of

CTCs. Prostate samples were also stained with 0.01 mg/ml anti-PSA (Dako, polyclonal). Capture efficiency and capture purity were calculated as follows:

$$\text{Capture Efficiency} = \frac{\#\text{ of cancer cells collected}}{\#\text{ of cancer cells in control well}} \qquad \text{Equation (4)}$$

$$\text{Purity} = \frac{\#\text{ of cancer cells}}{\#\text{ of cancer cells}+\#\text{ of WBCS}} \qquad \text{Equation (5)}$$

### 2.2.6. Cell viability and proliferation assay

Short term viability and longer term proliferation assays were conducted with A549 cells. Approximately 300 A549 cells were spiked into 5ml of PBS, processed through Vortex HE1 and HE2 devices, and collected in well plates. As a control, A549 cells were directly transferred into the well plate with cell media, without being processed through the device. For viability assays, cells were stained with 1µl of 0.01mg/ml Calcein AM and 2µl of 1mg/ml of Propidium Iodide (PI) post processing. The cells were collected in the well plate, imaged and enumerated. Live cells were CalceinAM+/PI- dead cells were CalceinAM±/PI+. For the cell proliferation assay, the cells were incubated at 37°C with 5% $CO_2$ and monitored every day for 4 days.

### 2.2.7. Patient studies

All blood samples were obtained with informed consent from patients and healthy donors, according to UCLA IRB#11-001798 and Stanford IRB#5630. A total of 3ml of blood was diluted 20X to 60 ml and processed through the Gen1 control device operated at 4ml/min and a separate 3 ml sample (60 ml diluted) was processed through the HE1 (new high efficiency device, operated at 2.6ml/min). Age-matched healthy donors were processed in a similar manner, with 1 male control for prostate, 1 female control for breast and an additional control for lung.

Blood samples were stained using the same procedures as cell lines spiked in blood. After staining, each well was imaged using a Photometrics CoolSNAP HQ2 CCD camera mounted on an Axio Observer.Z1 microscope (Zeiss), with an ASI motorized stage operated with Zen software. The samples were enumerated manually by two reviewers. CTCs collected from lung and breast samples were classified by DAPI+/CK+/CD45- or DAPI+/CK-/CD45- with a nucleus larger than 9µm and a high nuclear to cytoplasm ratio[57]. The 9µm size cut off metric is based on a large nuclear size classified as malignant in tumor cytomorphological analysis. CTCs from prostate samples were classified according to the same criterion in addition to being DAPI+/CK-/CD45-/PSA+. Detailed enumeration criteria are shown in Figure S8.

| Cancer | Stage | Type | Age | Gender |
|---|---|---|---|---|
| Lung | Stage IV | NSCLC | 70 | M |
| Lung | Stage IV | NSCLC | 49 | F |
| Lung | Stage IV | NSCLC | 66 | M |
| Prostate | Metastatic | Castration-resistant | 69 | M |
| Prostate | Metastatic | Castration-resistant | 73 | M |
| Prostate | Metastatic | Castration-resistant | 46 | M |
| Breast | Stage IV | ER+ PR+ HER2- | 39 | F |
| Breast | Stage IV | ER- PR- HER2- | 63 | F |
| Breast | Stage IV | ER- PR- HER2+ | 52 | F |
| Healthy 1 | N/A |  | 72 | M |
| Healthy 2 | N/A |  | 51 | M |
| Healthy 3 | N/A |  | 80 | F |

**Table 2-1. Patient sample information.** CTCs were collected from three types of cancer patients: Non Small Cell Lung Cancer (NCSLC), breast cancer, and prostate cancer. For each patient a total of 3ml of blood was processed through the Vortex HE1 and a separate 3 ml was processed through the Vortex Chip. Age-matched healthy donors were processed in a similar manner, with one male control for prostate, one female control for breast, and an additional control for lung. Cancer type, cancer stage, age and gender of the patients who consented and gave blood in this study.

## 2.3. Results and Discussion

### 2.3.1. Decoupling entry versus stability of particles in vortices

In agreement with predictions from the equation for $F_L$, we found that devices with smaller channel width and higher maximum velocity improved particle migration into the reservoirs. When maintaining a constant Reynolds number of 160 between devices, the Vortex HE2 design with channel width of 18µm and height of 44µm had the highest fraction of particles enter reservoirs, compared to Vortex HE1 with a channel width 24µm and height of 44µm (Figure 2-3a). The entry of particles in the Vortex Chip device was analyzed as well for reference (width 40µm and height of 70µm). Vortex Chip was operated at Re 150, which is the optimal Re at which the most particles can be trapped in this device.[9] In a channel with smaller cross sectional area, the maximum velocity within the channel is much higher for a constant Reynolds number. The smaller channel width also contributes to a sharper parabolic flow profile. These factors lead to a higher shear-gradient lift force experienced by all particles. As Figure 2-3a shows, 3 times more fraction of the particles in the size range 8-11µm can enter the HE1 and 7 times more can enter HE2 devices than Vortex Chip. Our observations indicate that as *a/W* increases, entry in reservoir increases as well, which is consistent with previous reports that indicated increased entry as *a/W* approaches 1.[5]

The results from particle entry suggest that the particle entry mechanism is mainly dominated by the entry channel dimensions, but is independent of reservoir size. The fraction of particles that enter devices with channel width 18µm and 24 µm but with smaller reservoirs remained similar as with larger reservoirs (Figure 2-4).

Once particles enter the reservoir, they must remain stably trapped in their orbit to be captured. We found that the stability of particle orbits increases with decreasing background levels of blood cells. We characterize the perturbation of a bead from its stable orbit by the variance of a Gaussian fit to a defined portion of its trajectory (Figure 2-3b). Variance for 20µm polystyrene bead orbits with a background of $2.5\times10^5$ RBCs (corresponding to 20x dilution) was half of the background level of $5\times10^5$ RBCs (corresponding to 10x dilution). Figure 2-3c indicates that orbit stability is independent of reservoir dimensions. The dilution of blood seems to be the main factor influencing stability. Lower orbit perturbations are expected to increase stability of trapping, and reduce the likelihood of particles to again cross the separatrix and enter the main flow once they have entered the vortex trap. Previous studies have demonstrated that the capture efficiency of cells spiked in blood increases with the dilution of blood,[9] which we now show is partly due to changes in the orbit variance with increasing background cell levels. Based on these results, further studies with CTC isolation in this work were performed with 20x diluted blood.

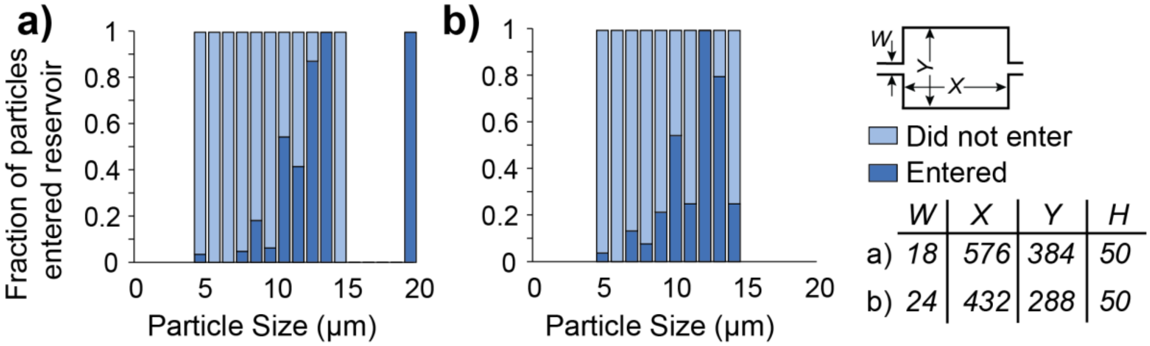

| | W | X | Y | H |
|---|---|---|---|---|
| a) | *18* | *576* | *384* | *50* |
| b) | *24* | *432* | *288* | *50* |

**Figure 2-4. Particle entry in devices with smaller reservoirs**. The fraction of particles that enter the reservoir represents the number of particles of a given size that entered the reservoir (dark blue bars) over the total number of particles of that size that went through the device. The dark blue counts are the particles entering the reservoirs while the light blue are the fraction of particles within that bin that did not enter the reservoirs. The blank spaces indicate that no particles of that size were observed in the whole video. The distribution of total number of particles present in the system remained comparable. Here the reservoir dimensions were reduced as well as the channel dimensions. W, Y, X, H respectively represent the channel width, reservoir width, reservoir length and device height. All units are in µm. N = 6 reservoirs.

### 2.3.2. Device validation with cell lines

The results from particle entry experiments indicate that a reduced channel width, when Reynolds number is kept constant, may enhance capture efficiency of cells. We tested our hypothesis with A549 cell lines spiked in PBS, which have reduced capture efficiency with Vortex Chip due to their smaller size.[11] The capture efficiencies of two devices with constant height of 44µm, constant Re of 160, and differing widths of 18µm (HE2) and 24µm (HE1) show that the device with the smallest width has the highest capture efficiency of 69% (Figure 2-5a), a 7 fold increase over Vortex Chip. The Re of 160 is used because it has the highest capture out of the range tested (Figure 2-6). Increased efficiency is due to capture of more cells and cells of smaller sizes. Although the average diameters of cells caught by

HE devices and Vortex Chip remain constant at approximately 18 µm, the minimum diameter of cells caught by HE1 is 11µm and HE2 is 13µm while Vortex Chip is higher at 15µm. Other device parameter variations such as changing the height to 50µm while maintaining the width at 18µm does not improve capture significantly (Figure 2-6).

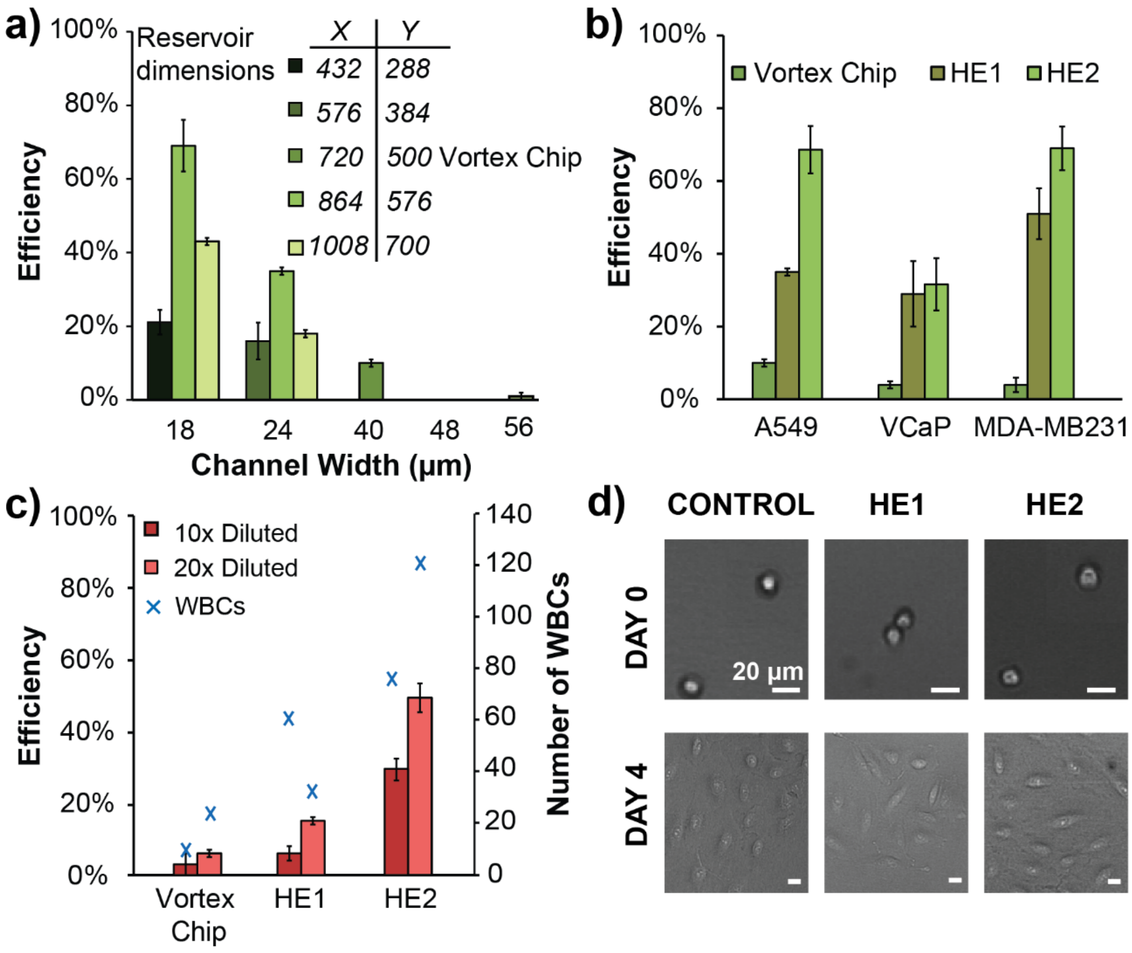

**Figure 2-5 Vortex HE provides higher efficiency capture for cancer cell lines.** a) Comparison of A549 capture efficiency of devices with different entry channel widths and reservoir sizes (N = 3). b) Vortex HE devices are able to capture other cancer cells at higher efficiencies than Vortex Chip (N = 3). c) A549 cells were spiked in diluted whole blood. HE devices outperform the Vortex Chip for both 10x and 20x dilutions of blood (N = 3). d) A549 cells are able to proliferate well after being processed through the HE devices.

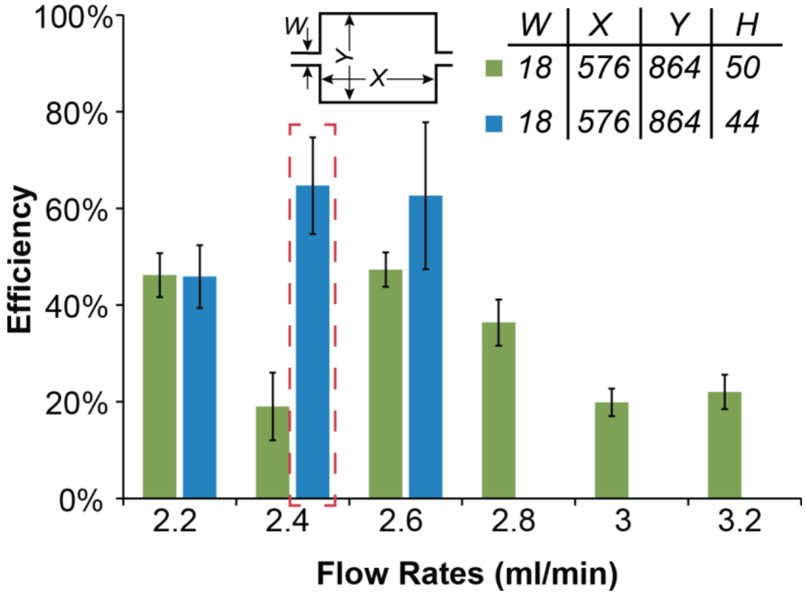

**Figure 2-6. Effects of height and flow rate on capture efficiency of A549 in PBS.** The scaled down entry channel width is coupled with a larger reservoir size to improve capture efficiency. W, Y, X, H respectively represent the channel width, reservoir width, reservoir length and device height. All units are in µm. The height of the device is very sensitive. We find that the height of 44µm performs better than the 50µm height. Various flow rates were also tested. The optimal flow rate is 2.4 ml/min for 44µm height, which corresponds to a Reynolds number of 160. N = 3.

The results from A549 capture experiments are consistent with the expectations from equation for $F_L$. When the width of the entry channel is decreased from the original 40µm to 18µm, $U$ is increased from 3m/s to 6m/s; we can assume $f_L$ is approximately equal in both cases. Thus lift force increases by a factor of 9 from the Vortex Chip to HE2 and by a factor of 4.6 from Vortex Chip to HE1. The higher lift force helps particles cross the main streamline and increases their probability of entering the reservoirs. Further reducing the channel cross sectional area could potentially yield better results, however higher pressure and device clogging would introduce operational issues.

In addition to the entry channel, the reservoir size also plays a role in capture efficiency. We find that scaling reservoir size down with channel widths of 18µm or 24µm only incrementally increases capture efficiency (Figure 2-7). However, a drastic improvement in capture occurs when we couple a narrow channel with a larger reservoir size of 864 x 576µm (Figure 2-5a). The increase in capture with the larger reservoirs may also result from the higher volume capacity. A larger reservoir can hold the same or greater amount of particles as a smaller reservoir while reducing the probability of inter-particle interactions.

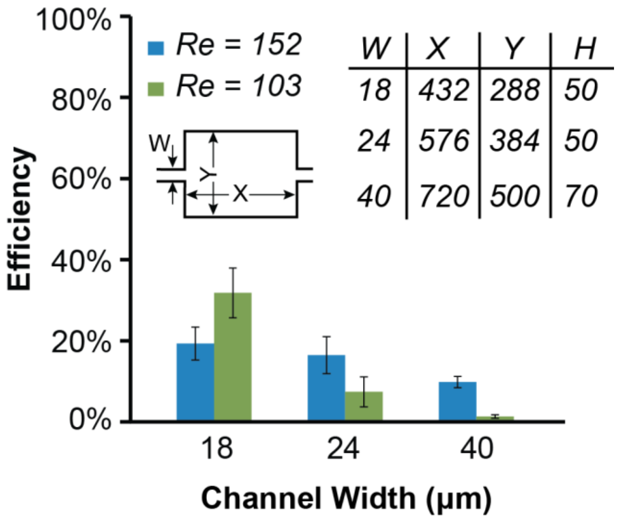

**Figure 2-7. Optimal flow rate for capture of A549 lung cancer cells in uniformly scaled devices**. W, Y, X, H respectively represent the channel width, reservoir width, reservoir length and device height. All units are in µm. Two different Reynolds numbers were tested on each of these scaled devices. These devices had scaled down reservoir and channel dimensions compared to Vortex Chip. N = 3.

Further increasing the reservoir dimensions leads to less capture. We use a COMSOL simulation to show that the largest reservoir (700 x 1008 µm) has a greater part of the separatrix entering the reservoir than in slightly smaller reservoirs (Figure 2-2). Particles circulating in the reservoirs may have more opportunity along the separatrix boundary to leave the vortex trap because the separatrix region increases in length in the larger reservoirs. As the reservoir size increases, the parabolic shape of the main entry flow also readjusts leading to loss of lift-inducing curvature and reduces restoration force on a particle. These factors likely contribute to particles leaving reservoirs and a reduction in particle capture (Figure 2-5a).

Consistent with entry and stability considerations, we find that Vortex HE effectively captures a broader size range of cancer cells from diluted whole blood. A549 cells were spiked in different dilutions of healthy blood and processed through Vortex Chip, HE1 and HE2 devices. For all 3 devices, the capture efficiency was higher with 20x diluted blood compared to 10x dilution, with up to 8 times better capture efficiency for device HE2 and 2.5 times better capture for device HE1. Though the number of WBCs captured by the new devices is higher than Vortex Chip, the purity of these devices remains comparable because the number of cancer cells captured concomitantly increases in the HE devices. In fact, the purity of the HE1 device is 66% which is higher than the 46% purity seen in the Vortex Chip for 20x diluted blood. On average when using 20x diluted blood, the HE1 device and Vortex Chip capture comparable numbers of WBCs, and HE1 captures higher numbers of cancer cells.

### 2.3.3. Cell proliferation assay

The Vortex HE device operates at a higher velocity and subsequently applies higher shear stress on the cancer cells. Such stress could negatively affect the cells. To assess this hypothesis, we investigated the viability and proliferation of the cells collected through the HE devices. Live/dead staining shows cells processed through the HE1 and HE2 devices have a 96% ± 7% and 96% ± 3% (N = 3) viability respectively immediately after processing. Figure 2-5d confirms that despite higher velocity and shear stress, cells collected with Vortex HE1 or HE2 were able to grow over 4 days. These confirm that higher velocity and shear stress do not affect viability or proliferation.

### 2.3.4. CTC enrichment from clinical samples

The capability of the higher efficiency devices to capture CTCs was evaluated with blood samples from patients diagnosed with three common types of cancer. Blood samples from three non-small cell lung cancer (NSCLC) patients, three prostate cancer patients, and three breast cancer patients were processed (Table 2-1), as well as blood samples from healthy donors of the same age. We selected the Vortex HE1 device for capture of CTCs from cancer patient samples because the HE1 device is less prone to channel clogging than HE2 due to slightly larger channels and filter designs, making it usable for a longer processing time and larger blood sample volume. The same samples were also processed through the previous Vortex Chip for comparison. These samples were stained for cytokeratins (CK), expressed in many cancer cells of epithelial origin, CD45 to identify WBCs, and DAPI to stain nuclei.

All three lung, all three prostate and two of three breast cancer samples had higher numbers of CTCs captured with the Vortex HE1 device than with the Vortex Chip (Figure 2-8a). When compared to the Vortex Chip device, the HE1 device captured on average 4 fold more total cells from cancer patients. A few cells that fit the criterion for CTCs were also seen in healthy samples, which can be used as a baseline threshold for disease. For healthy samples, the HE1 device captured on average two fold more cells than the Vortex Chip. Therefore, separate healthy thresholds have to be defined for each device. The maximum number of cells defined as CTCs found in the healthy samples was used as the threshold for each device. The threshold for Vortex HE and Vortex Chip is 1.5 CTCs/ml and 0.33 CTCs/ml respectively. Both devices identified CTCs above threshold in 67% of the cancer patients. A size distribution of the CTCs collected shows that 60% of the CTCs Vortex HE1 collects are below 15µm, whereas 30% of the CTCs captured by Vortex Chip are in this range (Figure 2-2). Capturing additional cells can aid in downstream molecular analysis and in sampling a larger section of tumor heterogeneity.

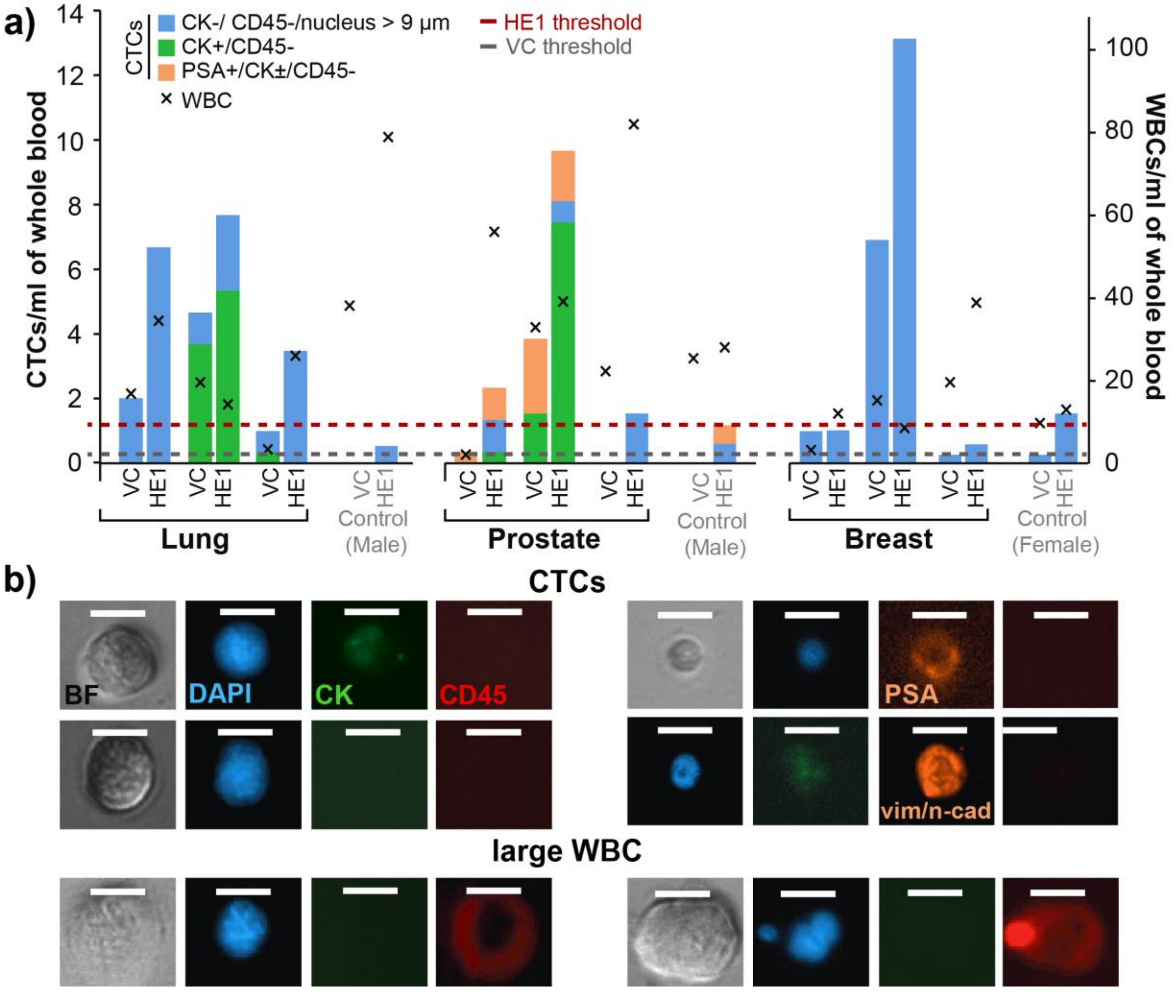

**Figure 2-8. Vortex HE provides improved capture performance for cancer patient samples**. a) Three blood samples each from lung, prostate and breast cancer patients were collected and processed to compare the performance of Vortex Chip and HE1 devices. The HE1 device is able to collect more CTCs than Vortex Chip. Age matched samples from two male and one female donors were used to set baseline thresholds. b) Example of CTCs found from lung, breast, and prostate cancer patients (rows 1, 2, 3 respectively). The 4th row shows a lung CTC expressing EMT markers. The 5th row shows an example of a rare large CD45+ cell that was collected and counted as WBCs.

Interestingly, the HE1 device was able to capture rare CD45+ cells larger than normal WBCs for one breast cancer and one prostate cancer patient. These cells, which were not seen in our previous studies using the Vortex Chip, were larger than 20µm, CD45+ and showed a low nuclear to cytoplasm ratio (Figure 2-8b). These cells could potentially be rare circulating macrophages, which has been observed by others as well.[12] The HE1 device may be capturing a rare population of WBCs that circulate in the blood stream in specific patients and conditions. Further investigations could potentially reveal new metrics for assessing disease states based on the number of rare large circulating cells beyond CTCs, which are effectively isolated with the new design.

We also found a subset of CTCs from all three cancer types that lacked cytokeratin expression (DAPI+, CD45-, large N/C ratio,). To further characterize these CTCs, we investigated whether these cells possessed markers consistent with an epithelial to mesenchymal transition (EMT). Using a vimentin/n-cadherin cocktail, immunostaining revealed that one lung and one breast cancer patient each had one cell that was negative for CK and positive for vimentin and/or n-cadherin. One lung cancer samples also contained 7 cells that were positive for both vimentin/ncadherin and CK. Only cells collected from Vortex HE had EMT markers. These results indicate that Vortex HE is able to capture some rare CTCs that have transitioned to a mesenchymal state.

## 2.4. Conclusion

We demonstrate that cell size cut-off in vortex-mediated rare cell trapping can be effectively controlled through the entry channel dimensions. The ability to tune particle size cut-off allows development of Vortex Chips for specific applications. Highest capture efficiency can be achieved using devices with the narrowest entry channel dimensions, however sample purity and ease of processing are reduced. As such, this device may be most ideal for isolating cancer cells from dilute solutions such as pleural fluids. Intermediate entry channel dimensions (Vortex HE1 Chip) enable capture of a broader size range of CTCs while maintaining the higher purity of previous devices. Capturing a larger distribution of the CTC population along with high purity should enable a deeper look into the genomic landscape of CTCs as they relate to primary and metastatic tumors. Ultimately, these devices could be used to prepare liquid biopsies for a range of applications: to better personalize drugs to the patient's mutational or phenotypic landscape as well as monitoring of therapeutic efficacy and development of resistance mutations or phenotypes.

## 2.5. References

1. Gerlinger, M. *et al.* Intratumor Heterogeneity and Branched Evolution Revealed by Multiregion Sequencing. *New England Journal of Medicine* **366,** 883–892 (2012).
2. Bai, H. *et al.* Detection and Clinical Significance of Intratumoral EGFR Mutational Heterogeneity in Chinese Patients with Advanced Non-Small Cell Lung Cancer. *PLoS One* **8,** e54170 (2013).
3. Chen, Z.-Y. *et al.* EGFR Mutation Heterogeneity and the Mixed Response to EGFR Tyrosine Kinase Inhibitors of Lung Adenocarcinomas. *The Oncologist* **17,** 978–985 (2012).
4. Martelotto, L. G., Ng, C. K., Piscuoglio, S., Weigelt, B. & Reis-Filho, J. S. Breast cancer intra-tumor heterogeneity. *Breast Cancer Res.* **16,** R48 (2014).
5. Mach, A. J., Kim, J. H., Arshi, A., Hur, S. C. & Di Carlo, D. Automated cellular sample preparation using a Centrifuge-on-a-Chip. *Lab Chip* **11,** 2827–34 (2011).
6. Gql, T., Gql, T. H. E. & Table, R. Supplementary Material. 1–9
7. Friend, J. & Yeo, L. Fabrication of microfluidic devices using polydimethylsiloxane. *Biomicrofluidics* **4,** 26502 (2010).
8. Sbalzarini, I. F. & Koumoutsakos, P. Feature point tracking and trajectory

analysis for video imaging in cell biology. *J. Struct. Biol.* **151,** 182–195 (2005).

9. Sollier, E. *et al.* Size-selective collection of circulating tumor cells using Vortex technology. *Lab Chip* **14,** 63–77 (2014).
10. Che, James, Yu, Victor, Dhar, Manjima, Rennier, Corinne, Matsumoto, Melissa , Heirich, Kyra, Garon, Edward B, Goldman, Jonathan, Rao, Jianyu, Jeffrey, Stefanie S., Kulkarni, Rajan P, Sollier, Elodie, and Di Carlo, D. Classification of large circulating tumor cells isolated with ultra-high throughput microfluidic Vortex technology. *Cancer Res.*
11. Jiang, R. De, Shen, H. & Piao, Y. J. The morphometrical analysis on the ultrastructure of a549 cells. *Rom. J. Morphol. Embryol.* **51,** 663–667 (2010).
12. Adams, D. L. *et al.* Circulating giant macrophages as a potential biomarker of solid tumors. *Proc. Natl. Acad. Sci. U. S. A.* **111,** 3514–9 (2014).

# Chapter 3. Label Free Counting of CTCs

Regardless of the CTC collection approach, the current standard for enumerating CTCs involves immunofluorescence staining to visualize specific markers for CTCs and WBCs – a method with significant limitations. While this standard is evolving, in general, cytokeratin (CK) and/or EpCAM markers are used to identify CTCs while CD45 is used for WBCs[1]. White blood cells staining positive for both CD45 and CK may be isolated[2], and have been identified as granulocytes with additional CD66b staining[3,4]. On the other hand, some large cells negative for both CD45 and CK have also been reported. Such double staining or lack of any CK/EpCAM stain makes classification of these cells difficult [5–7]. In addition, several experimental factors can affect immunofluorescence analysis. These include variation in the antibodies used (sensitivity, clones, fluorophores), staining protocol, and lastly the image analysis methodology. In addition to these experimental issues, immunostaining based enumeration is time-consuming and costly. Simple analysis methods would enable a rapid and low-cost count for more efficient use of downstream resources on samples with large cell burdens. Other staining methods that offer more detailed characterization of isolated CTCs include in situ hybridizations (FISH). FISH can be used to identify mutations within individual cells. Such cytopathological studies are expensive and time consuming. Having a system determine if enough CTCs are present in the sample to further pursue the analysis would be cost effective and helpful. Here we describe an in-flow counting method that can be used downstream of vortex capture.

In-flow counting enables a rapid assessment of the cancer-associated large circulating cells in a sample within minutes to determine whether standard downstream assays such as cytological and cytogenetic analyses that are more time consuming and costly are warranted. Using our platform integrated with these workflows, we analyzed 32 non-small cell lung cancer (NSCLC) and 22 breast cancer patient samples, 77.8% of the patients had above healthy threshold of CTC counts using automated in flow counting, which correlated with cytology and immunofluorescence counts.

## 3.1. In-flow and label-free counting of large circulating cells

Because of the high purity isolation achieved with the Vortex HT Chip, we investigated counting of all isolated large cells as a measure of abnormal malignant processes[9,3]. A high large cell count, whatever the origin of these cells, could then indicate that downstream label-based enumeration assays would be warranted. For this purpose, we developed an in-flow counting system to enumerate the number of cells trapped and released by the Vortex HT chip before their collection at the chip outlet (Figure 3-1). The system achieved high-speed brightfield imaging of released cells followed by image analysis to identify and extract morphological features for each cell. We trained the image analysis algorithm to identify cancer cells by first capturing A549 lung cancer cells spiked in PBS in the vortex traps and enumerating the released cells, before progressing to clinical patient samples. Accepted ranges for cell diameter, solidity, axial ratio and pixel intensity distribution were determined, based on the in-flow morphology of A549 cells. Cell diameter ranged from 12 to 55 µm, solidity ranged from 0.7 to 1, axial ratio ranged from 1 to 1.8, and the pixel intensity range within the cell was 0-20,000. Following this training and to evaluate the performance of our label-free approach, A549 cells (10 to 600) were spiked into 5 mL of PBS and processed through the Vortex HT Chip. The captured cells were simultaneously enumerated in-flow and following collection in a well plate followed by DAPI staining. The DAPI staining was used to determine location of the cell, and the brightfield image was used to measure the size of the cell. Figure 2A indicates a high correlation ($R^2$=0.97) and unity relationship (y=1.02x) between the number of cells counted with in-flow counting using an automated script and the number of cells enumerated after staining in the well plate, and supported the accuracy of our counting method.

We next applied this approach to counting the cells in NSCLC patients and age-matched healthy blood samples. Samples from nine NSCLC patients and five healthy controls show a strong linear correlation between automated cell counts and well plate counts (Figure 2.B), with a slight overcounting bias for the automated count (y=1.04x). A gallery of cells imaged in-flow is shown in Figure 3-4. Cell counts from healthy samples can be used as a threshold to define patients with abnormal numbers of large cells above this healthy background. Using automated counting, a healthy threshold can be defined at 3.15 cells/mL (mean+2SD), leading to 7/9 (77.8%) of NSCLC patients with automated cell counts above the healthy threshold. Using well-plate cell counts, the healthy threshold can be defined at 7.7 cells/mL, with 3/9 (33%) of the patients above the threshold. For both counting approaches, patients L5, L8, and L9 were above threshold while patients L3 and L6 were below.

Patient L7 is just below the threshold using well-plate-counts (7.25 cells/mL) but above the threshold according to automated-counting (7.63 cells/mL). These data validate the ability of automated-counting to yield rapid label-free enumeration of large cells following Vortex trapping, which are present at higher levels in NSCLC patients.

## 3.2. High-speed, label-free cell imaging and automated cell analysis script

A high-speed camera was used to collect videos of cells during their release from the vortices and as they flowed past the imaging region (a portion of the outlet channel). The resulting video images were then analyzed using a custom image processing algorithm (Figure 3-1). Videos were collected using a 10X brightfield Nikon objective lens mounted on a Phantom v2010 high-speed camera and controlled through a Phantom Camera Control and Software (Vision Research Inc). For each incident cell, a collection of images (256 x 376 pixels) was captured (6006 frames per second) for a total of 15 seconds. The cells appeared 6 times in the viewing window to ensure that none were missed. The focal plane was manually adjusted prior to sample injection, using the walls of the exit channel area as a reference. To initiate the release of the trapped cells, the flow rate was stopped and 15s of video was recorded concomitantly. Majority of the cells are released within this time frame as shown in Figure 3-5. Cells remained in focus when recording a region downstream near the outlet because here we avoid a large hydrodynamic pressure buildup during operation. The depth of focus of the 10x Nikon objective used was 8.5µm and, given the large depth of focus, small shifts out of the focal plane were not found to significantly affect the size calculations when imaging of these cells.

The image processing algorithm identifies cells by their morphology. Objects are detected using a background subtraction method. Briefly, the intensity values of an empty frame are subtracted from each ensuing image of the video, which eliminates the background image and yields traces of incident particles in the frames in which they appear (Figure 3-3). In our algorithm that detects object boundaries first each image is scaled by a factor of 3 with interpolation. The images are converted to binary, and the particle traces are then filled with morphological closing (dilation followed by erosion) to be measured for their diameter, solidity (area/convex hull, where convex hull is the smallest enclosed convex region around the object), axial ratio (major axis/minor axis), and cell interior pixel intensity distribution. Data were thresholded for diameter greater than 12 µm and less than 55 µm. A detailed description of these parameters is provided in Figure 3-2C. These parameters were determined during control experiments with lung cancer cell lines. The detected objects are displayed in a matrix. These results give us information concerning the number of cells collected and their morphologies.

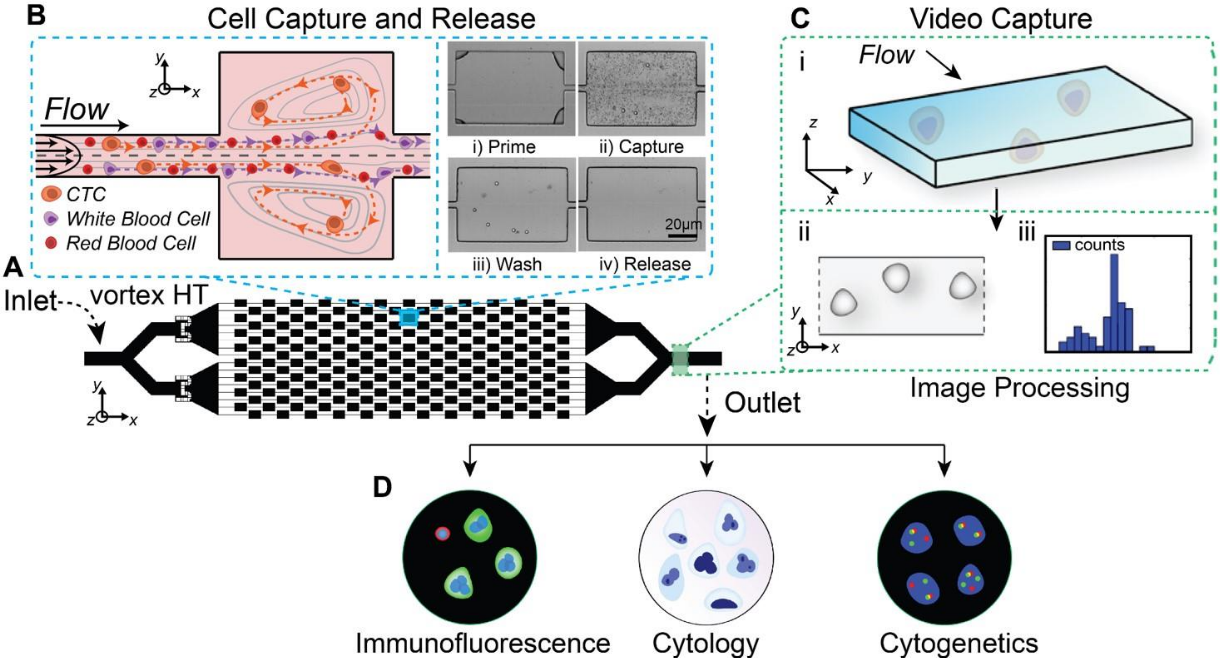

**Figure 3-1. Label-free isolation and enumeration of CTCs followed by downstream analysis.** (A) The Vortex HT chip is used to capture CTCs in vortices formed in microfluidic reservoirs. (B) After a priming step, CTCs are selectively trapped by size in the microscale vortices, RBCs and WBCs are washed away with a clean buffer, then remaining larger trapped cells are released into well plates or slides. (C) A region of the outlet channel is recorded to image the released cells in-flow for enumeration. An algorithm is used to process the video, determine morphological features of cells collected, and enumerate based on morphological thresholds. (D) The output from the video analysis allows the user to determine whether to perform downstream analysis. This could include immunofluorescence, cytology and cytogenetic analyses.

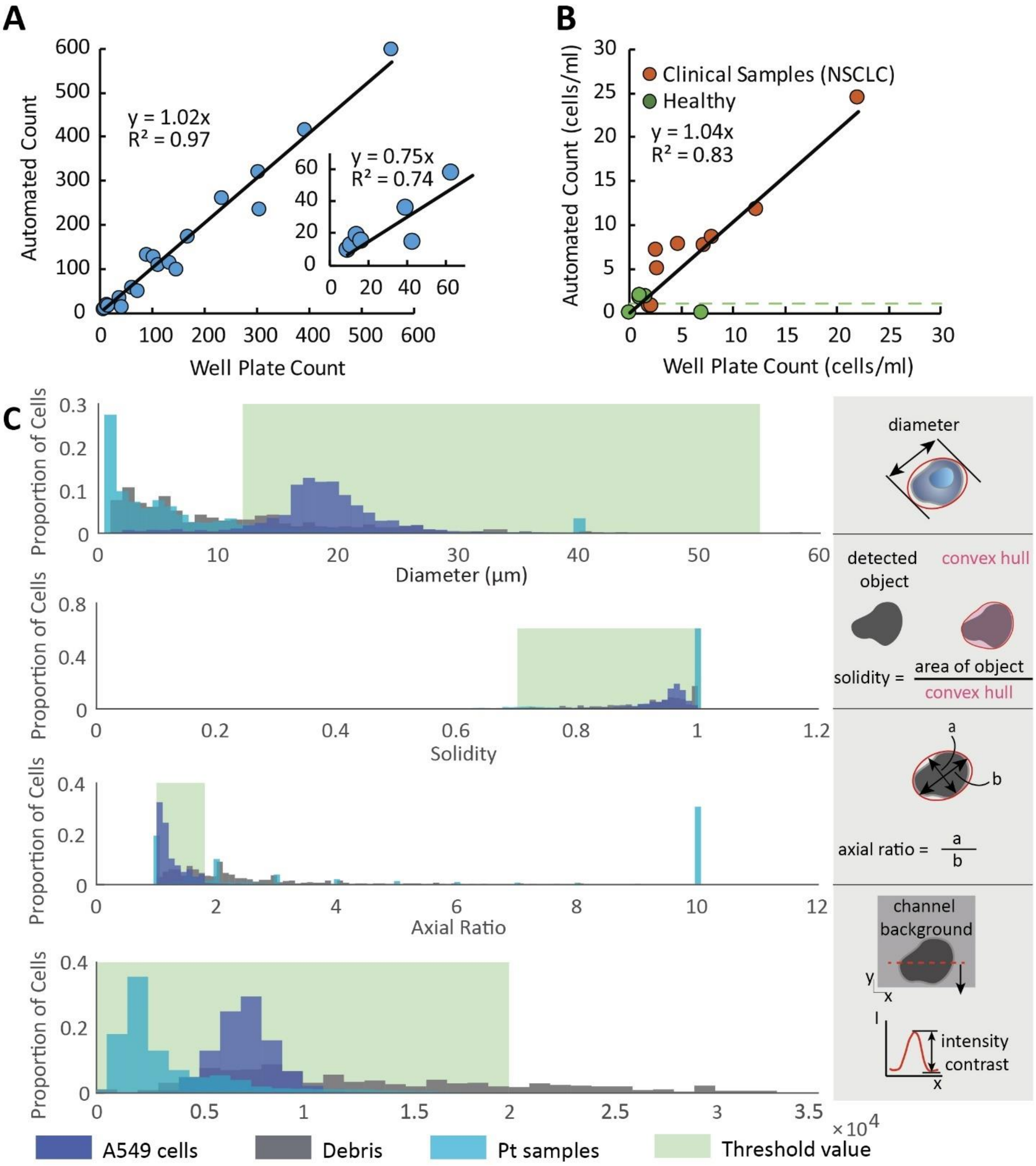
A
Automated Count
Well Plate Count
y = 1.02x
R² = 0.97
y = 0.75x
R² = 0.74
0
100
200
300
400
500
600
0
20
40
60
B
Automated Count (cells/ml)
Well Plate Count (cells/ml)
Clinical Samples (NSCLC)
Healthy
y = 1.04x
R² = 0.83
0
5
10
15
20
25
30
C
Proportion of Cells
Diameter (μm)
Solidity
Axial Ratio
×10^4
diameter
detected object
convex hull
solidity = area of object / convex hull
a
b
axial ratio = a / b
channel background
y
x
I
x
intensity contrast
A549 cells
Debris
Pt samples
Threshold value

**Figure 3-2. In-flow label-free counting of large cells.** (A) The in-flow counting algorithm was validated with A549 cell lines. 10-600 cells were initially spiked into 5 mL of PBS and processed. A correlation of $R^2$=0.97 was found between the number of cells identified per the algorithm and the number of cells manually counted in the well plate. Inset axes show cells per mL. (B) This method was used to enumerate 9 NSCLC patient samples (L1-9), and 5 samples from healthy donors (H1-5). Only cells larger than 12 µm were counted for the well plate. The counting criteria for the cells imaged in-flow included ranges for cell diameter, circularity, axial ratio, and specific pixel intensity distribution defined with A549 cells. (C) The counting criteria for the cells imaged in-flow included threshold ranges for cell diameter, solidity, axial ratio, and specific pixel intensity distribution. The thresholding order is given in the four histograms. All parameters for all objects that were detected is shown before thresholding was performed. Clinical blood samples had a larger proportion of debris compared to A549 spiked in blood.

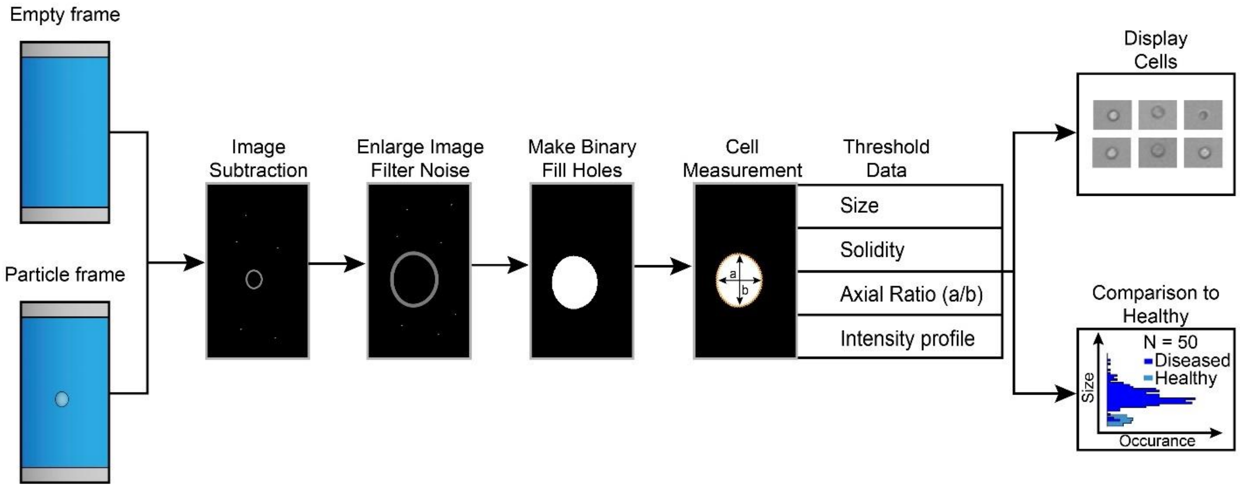

**Figure 3-3 Custom Image Processing.** A custom image processing algorithm was used to identify cells by their morphology. Objects are detected using a background subtraction method, where the intensity values of an empty frame are subtracted from each ensuing image of the video. Each image is first enlarged by a factor of 3 with interpolation. The images are then converted to binary, and the particle traces are filled with morphological closing (dilation followed by erosion) and measured to determine their diameter, solidity, axial ratios (major axis/minor axis), and cell interior pixel intensity distribution. The data is then thresholded for diameter greater than 12 µm and less than 55 µm. The solidity ranged from 0.7 to 1.0 and the axial ratio ranged from 1 to 1.8. A matrix of cell images and size histograms of cells are shown in the output.

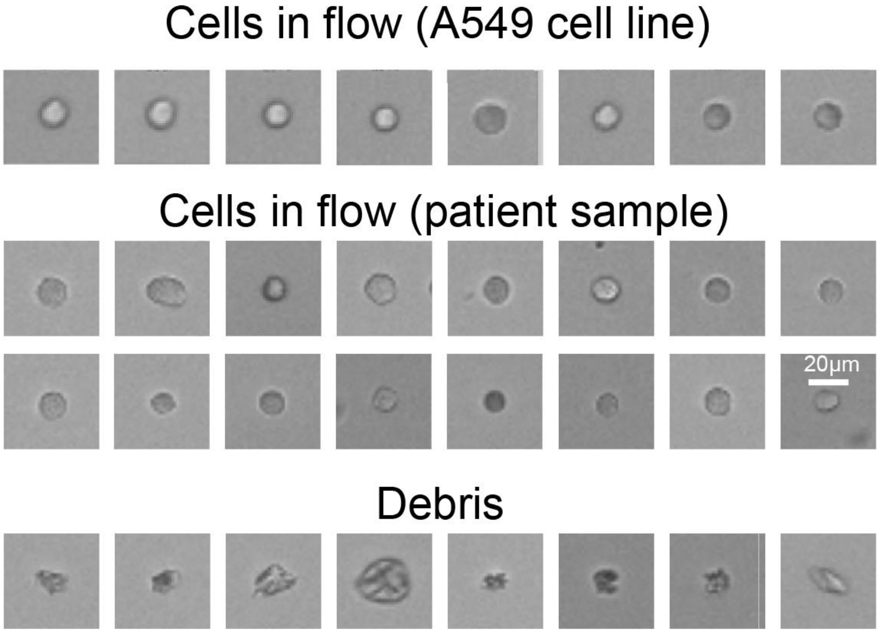

**Figure 3-4. Gallery of cells in-flow.** Cells collected from patient samples were imaged in-flow using bright-field high-speed microscopy. All objects found were thresholded for diameter greater than 12 μm and less than 55 μm. The solidity ranged from 0.7 to 1.0 and the axial ratio ranged from 1 to 1.8. This gallery gives an example of objects that would be classified as cells or as debris respectively.

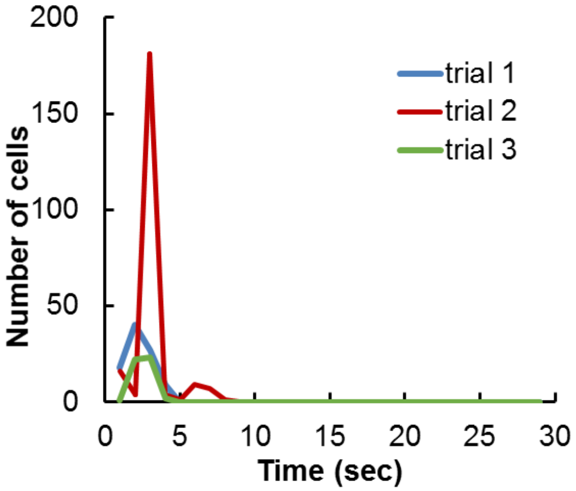

**Figure 3-5. Release time of cells from vortices.** The majority of cells are released from vortices within the first five seconds, while recording is performed over 15 seconds.

## 3.3. Conclusions

We have demonstrated the utility of Vortex trapping technology as a platform to enable extraction of CTCs and interfacing with downstream assays of clinical importance. Our cell capture approach enables the coupling of label-free cell enumeration in-flow based on bright field images with various standard assays downstream, such as cytology and cytogenetics. In-flow microfluidic cytological staining could also enhance such assays in the future, enabling rapid counts[10]. A simple count of tumor-associated large circulating cells obtainable within minutes after processing could avoid costly immunofluorescence-based enumeration as used currently, as well as indicate downstream assays for the subset of samples with sufficient numbers of cells, also avoiding wasted time and costs.

All cells collected can be counted in-flow, without the need for any cell-specific labels and remain unaltered, allowing cells to be collected off-chip for further characterization assays, such as cytology, cytogenetics, genomic profiling, transcriptomic and drug assays, and even conventional immunofluorescence. More importantly, these results introduce label-free analysis as a potential method to rapidly identify patient samples with high cell counts directly compatible with downstream assays (e.g. cytology, FISH, genetic analysis, or further immunostaining), or conversely, limit the use of valuable resources on samples without significant diagnostic cells. Although these initial data are promising, additional patient samples from a variety of cancer types and cancer stages are needed to validate the approach further. Further, direct single-cell comparisons between morphological and immunofluorescence staining for CTCs would be interesting to investigate in the future, and should be enabled by high-speed imaging cytometry technology[11].

## 3.4. References

1. Patriarca, C., Macchi, R. M., Marschner, A. K. & Mellstedt, H. Epithelial cell adhesion molecule expression (CD326) in cancer: A short review. *Cancer Treat. Rev.* **38,** 68–75 (2012).

2. Streicher, J., Fabian, B., Herkner, K., Pointner, H. & Bayer, P. M. Anticytokeratins are a potential source of false-positive indirect immunofluorescence assays for C-ANCA. *J. Clin. Lab. Anal.* **12,** 54–9 (1998).

3. Che, J. *et al.* Classification of large circulating tumor cells isolated with ultra-high throughput microfluidic Vortex technology. *Oncotarget* **7,** 12748–12760 (2016).

4. Karabacak, N. M. *et al.* Microfluidic, marker-free isolation of circulating tumor cells from blood samples. *Nat. Protoc.* **9,** 694–710 (2014).

5. Went, P. T. *et al.* Frequent EpCam protein expression in human carcinomas. *Hum. Pathol.* **35,** 122–8 (2004).

6. Mikolajczyk, S. D. *et al.* Detection of EpCAM-Negative and Cytokeratin-Negative Circulating Tumor Cells in Peripheral Blood. *J. Oncol.* **2011,** 252361 (2011).

7. Serrano, M. J. *et al.* EMT and EGFR in CTCs cytokeratin negative non-metastatic breast cancer. *Oncotarget* **5,** 7486–7497 (2014).

8. Shaw, A. T. *et al.* Effect of crizotinib on overall survival in patients with advanced non-small-cell lung cancer harbouring ALK gene rearrangement: a retrospective analysis. *Lancet Oncol.* **12,** 1004–1012 (2011).

9. Sollier, E. *et al.* Size-selective collection of circulating tumor cells using Vortex technology. *Lab Chip* **14,** 63–77 (2014).

10. Tan, S. J., Yobas, L., Lee, G. Y. H., Ong, C. N. & Lim, C. T. Microdevice for the isolation and enumeration of cancer cells from blood. *Biomed. Microdevices* **11,** 883–892 (2009).

11. Diebold, E. D., Buckley, B. W., Gossett, D. R. & Jalali, B. Digitally synthesized beat frequency multiplexing for sub-millisecond fluorescence microscopy. *Nat. Photonics* **7,** 806–810 (2013).

# Chapter 4. PD-L1 Expression on CTCs

## 4.1. Introduction

Clinically relevant molecular analysis of CTCs involves studying the response of CTCs to immune stress. In certain immunogenic tumors, tumor infiltrating lymphocytes invade the periphery of the tumor and try to launch an attack against the tumor cells. The immune response to cancer involves a complex network of cellular interactions. Antigen presenting cells (APCs) can recognize neoantigens from some immunogenic tumors (1, 2). These APCs help activate cytotoxic T-cells, helper T-cells and natural killer cells. All of these components work in concert against tumor cells. However, many metastatic tumors such as in non-small cell lung cancer (NSCLC) have adopted methods to evade immune detection and/or clearance (3). One of the recently discovered pathways that tumors use is the overexpression of programmed cell death ligand 1 (PD-L1). PD-L1 binds to PD-1 on T-cells and suppresses its activity (4, 5). Immunotherapy based on inhibition of PD-1 or PD-L1 represents a breakthrough in the treatment of advanced cancers, particularly lung, renal, and melanoma cancers. Although only a minority of patients have clinical response, those that do often have a durable and lasting response (6-12).

Finding biomarker predictors of response to PD-L1 blockade has proven challenging. Even within the immunotherapy trial cohorts, the response varies based on the activated T-cells the patient has and PD-L1 expression level on the tumor (6-10). Some studies have suggested that the level of PD-L1 expression on the initial tumor tissue can predict positive response, while other studies suggest that the level of infiltrating CD8+ lymphocytes are also significant predictors of response (7, 10, 13). Past studies of renal cancer show tumors with high PD-L1 levels respond, while those with low levels do not respond (10). Based on these findings, a clinical trial for anti-PD1 (pembrolizumab) was conducted where NSCLC patients were screened based on expression levels of PD-L1 on the primary tumor (7, 14). Response rate, progression free survival and overall survival with PD-1 inhibitors were greater in tumors with high tumor PD-L1 expression (7, 11). Although current guidelines call for anti-PD1 therapies after failure of standard chemotherapy, these are rapidly changing and recent phase I trial data suggests that anti-PD1 therapies may be effective as first line therapy (15). First line therapy is especially promising for patients with higher PD-L1 expression on their biopsies and is associated with improved responses (7).

Several challenges exist in screening patients with only an invasive biopsy of the primary tumor. Biopsies allow sampling from limited sections of the tumor at one time point, which may not detect tumor heterogeneity. Furthermore, especially for lung cancer, the biopsy tissue may be limited or may have been taken much earlier in the cancer’s course (i.e. before it became metastatic). This is because repeat biopsies are avoided due to potential serious complications. If a biopsy is limited to the primary tumor only at one time point, it also does not allow evaluation of other metastasized tumor sites, and the primary tumor may not necessarily be representative of the metastatic sites. As reported, some patients whose primary tumor was negative for PD-L1 still responded well to anti PD-1 treatment, potentially because the biopsy may not have captured the heterogeneous expression of PD-L1 on the tumor (7). Biopsy of multiple sites or serial biopsies during treatment could address some of these issues, however it may not be feasible due to the invasiveness of the procedure and the potential risks to the patient. In this regard, PD-L1 expression on circulating tumor cells (CTCs) could aid in screening and monitoring patients (16). CTCs are tumor cells that are shed from various locations of the primary and/or metastatic tumors (17-19). As such, they may inherently better represent the spectrum of genetic and epigenetic variability within a patient's tumors. Additionally, following PD-L1 levels overtime on CTCs may potentially yield information about modulation of tumor PD-L1 expression in the presence of inhibition of the PD-1/PD-L1 interaction.

There have been few studies to explore PD-L1 expression on CTCs, either in breast cancer (15) or in bladder cancer (20) and another examining nuclear PD-L1 expression in colon and prostate CTCs (16, 21). To our knowledge, only one recent study from Nicolazzo et al. is evaluating PD-L1 expression in NSCLC CTCs and examining PD-L1 expression in the context of active immunotherapy treatment, particularly PD-1/PD-L1 inhibition (nivolumab in their study) (22). Most of these previous studies utilized specific surface markers for the CTC capture, either with CellSearch or with similar magnetic bead technology, and did not isolate cells in a manner that is unbiased to surface expression. There are still other knowledge gaps, particularly in how PD-L1 expression on CTCs correlates with expression on tumor biopsies, what method to use for quantifying PD-L1 expression, on both CTCs and tumor biopsies, and how PD-L1 expression on CTCs varies, both at time of initial treatment and as therapy continues.

Here, we evaluate the PD-L1 expression on 31 CTC-containing samples, obtained from 22 patients with metastatic NSCLC who were scheduled to receive or were receiving PD-1 or PD-L1 inhibitors, including 11 metastatic NSCLC patients scheduled to receive the anti-PD-1 treatment pembrolizumab (one patient ended up receiving erlotinib) (Table 4-1). Most patients were evaluated for CTC collection prior to treatment or at the beginning of the second cycle of treatment. For patients receiving pembrolizumab or erlotinib, we compared the quantitative expression of PD-L1 to levels on tumor biopsies taken before treatment when available (N=4) and correlated with response as measured by progression free survival (PFS). Tumors of patients receiving pembrolizumab were originally graded as positive for PD-L1 as this was one of the initial inclusion criteria for receiving this therapy.

Our findings suggest that PD-L1 expression on CTCs may be a valuable adjunct biomarker in assisting to predict those who are likely to have improved response to PD-1/PD-L1 inhibition in NSCLC and may be useful for other cancers in which PD-1/PD-L1 inhibitors may be given. Furthermore, an increase in CTC count with concomitant loss of or change in PD-L1 expression may herald loss of efficacy of PD-1 inhibition, which may be very useful in cases where repeat biopsies are not possible, such as in lung cancer or other internal malignancies.

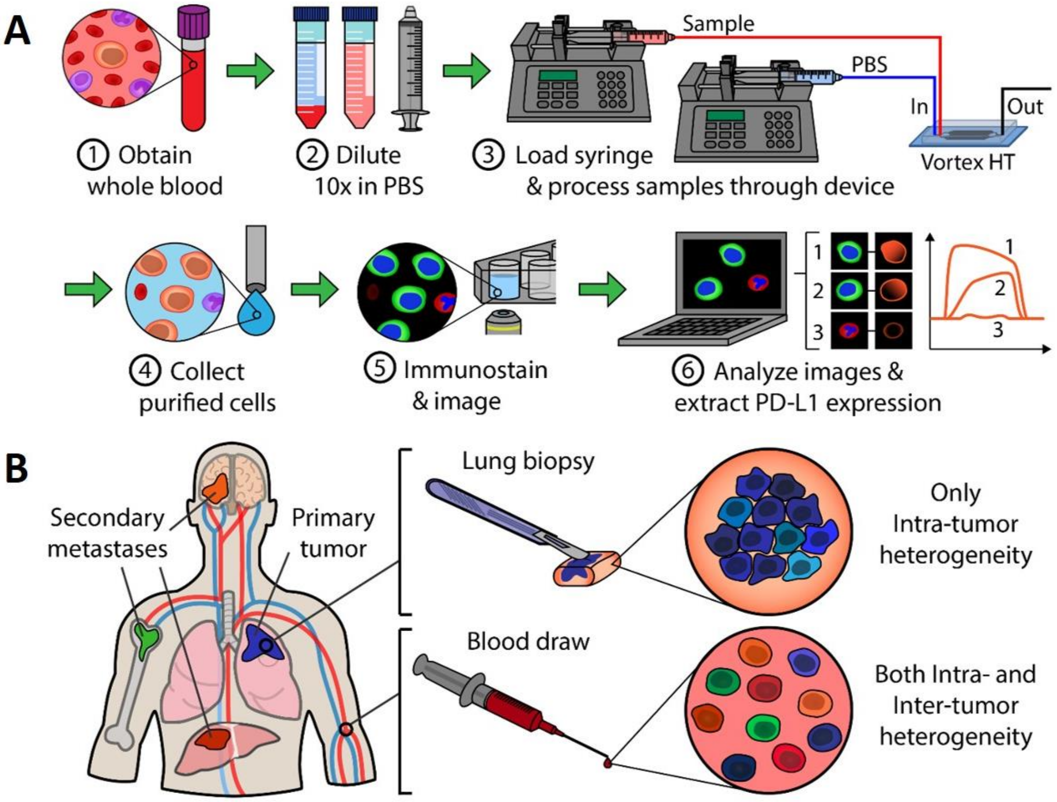
A
Sample
PBS
In
Out
Vortex HT
① Obtain whole blood
② Dilute 10x in PBS
③ Load syringe & process samples through device
④ Collect purified cells
⑤ Immunostain & image
1
2
3
1
2
3
⑥ Analyze images & extract PD-L1 expression
B
Secondary metastases
Primary tumor
Lung biopsy
Only Intra-tumor heterogeneity
Blood draw
Both Intra- and Inter-tumor heterogeneity

**Figure 4-1. Workflow for evaluation of PD-L1 expression on patient CTC and matched tumor biopsy.** (A) CTC Workflow. ① Blood is collected from cancer patients and processed through Vortex technology to enrich for CTCs. ② Blood is diluted 10X with PBS and ③ injected through the microfluidic device with syringe pumps. ④ Purified cells are collected into a 96 well-plate, where they are ⑤ stained with immunofluorescence markers and imaged. ⑥ Fluorescence intensity can be analyzed and PD-L1 gene expression quantified. (B) Tumor biopsy workflow: In parallel of the CTC workflow, lung biopsies were analyzed for PD-L1 expression. While biopsy provides information on the intra-tumor heterogeneity, only the CTCs present in a blood draw can cover both intra and inter-tumor heterogeneity.

## 4.2. Methods

### 4.2.1. Patient cohort and blood donation

This study included 32 volunteers for blood donation, 22 metastatic NSCLC patients and 10 healthy donors (Table 4-1). Among the 22 patients, 10 NSCLC patients were receiving anti-PD-1 treatment, pembrolizumab, 9 NSCLC patients receiving anti-PD-1 treatment nivolumab (Bristol-Myers Squibb), and 2 NSCLC patients receiving anti-PD-L1 treatment avelumab (EMD Serono). 1 patient was evaluated for treatment with pembrolizumab but eventually received erlotinib. For 2 patients (patients #16 and 19), blood was collected at several time points; 5 times for patient 16 (before the treatment, and 4 follow-up draws) and 6 times for patient 19 (after the first dose, 4 follow-up draws, after the treatment).

As this was a pilot study, samples were evaluated at different time points, though effort was made to collect blood samples prior to any treatment commencing or within three weeks of starting treatment. Of these 31 patient samples, 17 were sampled prior to commencing treatment, 2 were sampled after the first dose after two weeks, while the remaining 11 were taken at various time points while on treatment and 1 after the treatment. All patients receiving pembrolizumab were categorized as having positive PD-L1 expression in their original tumor biopsies (7). 4 matched biopsies were available for analysis for this study.

After obtaining informed consent according to UCLA IRB approved protocol (IRB #11-001798), 6-10 cc of blood were collected from each patient in EDTA tubes. Collected samples were processed to isolate CTCs within four hours of collection. Blood samples from healthy volunteers (n=10) of various ages were similarly processed.

| No. | Sex | Age | Type | Treatment | Time | Biopsy? | CTCs | Vol. | CTCs/mL | (PDL1+) | (PDL1-) | (UD) | WBCs/mL |
|---|---|---|---|---|---|---|---|---|---|---|---|---|---|
| P 01 | M | 61 | squamous | Pembrolizumab | Pre | √ | 47 | 6 | 7.83 | 4.83 | 2.83 | 0.16 | 60 |
| P 02 | M | 59 | adeno. | Pembrolizumab | Pre | - | 35 | 6 | **5.83** | 5 | 0.83 | - | **6** |
| P 03 | F | 77 | adeno. | Ipilimumab, Nivolumab | Pre | - | 44 | 8 | **5.5** | 0 | 5.5 | - | **17** |
| P 04 | M | 67 | adeno. | Nivolumab | Pre | - | 28 | 6 | **4.67** | 2.83 | 1.83 | - | **56** |
| P 05 | F | 59 | adeno. | Pembrolizumab | Pre | **√** | 19 | 6 | **3.17** | 1.5 | 1.66 | - | **18** |
| P 06 | F | 61 | adeno. | Erlotinib | Pre | **√** | 24 | 8 | **3** | 2 | 1 | - | **1** |
| P 07 | F | 77 | adeno. | Pembrolizumab | Pre | **√** | 19 | 9 | **2.11** | 0.33 | 1.77 | - | **11** |
| P 08 | F | 87 | adeno. | Ipilimumab, Nivolumab | Pre | - | 16 | 8 | **2** | 0 | 2 | - | **93** |
| P 09 | F | 91 | adeno. | Ipilimumab, Nivolumab | Pre | - | 10 | 8 | **1.25** | 0 | 1.25 | - | **18** |
| P 10 | M | 65 | adeno. | Ipilimumab, Nivolumab | Pre | - | 3 | 8 | **0.38** | 0 | 0.38 | - | **11** |
| P 11 | M | 66 | adeno. | Ipilimumab, Nivolumab | Pre | - | 2 | 6 | **0.33** | 0.16 | 0.16 | - | **19** |
| P 12 | F | 60 | adeno. | Ipilimumab, Nivolumab | Pre | - | 2 | 7 | **0.29** | 0 | 0.29 | - | **27** |
| P 13 | M | 65 | adeno. | Pembrolizumab | Pre | - | 1 | 6 | **0.17** | 0 | 0.17 | - | **23** |
| P 14 | M | 64 | adeno. | Pembrolizumab | Pre | - | 1 | 9.8 | **0.1** | 0.1 | 0 | - | **2** |
| P 15 | F | 75 | squamous | Ipilimumab, Nivolumab | Pre | - | 0 | 6 | **0** | 0 | 0 | - | **13** |
| P 16 – 1 | M | 62 | squamous | Avelumab | Pre | - | 20 | 6 | **3.33** | 3 | 0 | 0.33 | **10** |
| P 16 – 2 |  |  |  |  | On treatment | - | 5 | 8 | **0.62** | 0.5 | 0.12 | - | **10** |
| P 16 – 3 |  |  |  |  |  | - | 11 | 6 | **1.83** | 1.83 | 0 | - | **5.3** |
| P 16 – 4 |  |  |  |  |  | - | 31 | 8 | **3.87** | 3.5 | 0.12 | 0.25 | **14.9** |
| P 16 – 5 |  |  |  |  |  | - | 6 | 6 | **1** | 1 | 0 | - | **10** |
| P 17 | M | 78 | adeno. | Pembrolizumab | Pre | - | 3 | 8 | **0.38** | 0.125 | 0.25 | - | **13** |
| P 18 | M | 82 | adeno. | Ipilimumab, Nivolumab | After 1st dose | - | 1 | 6 | **0.17** | 0.17 | 0 | - | **19** |
| P 19 – 1 | M | 69 | squamous | Pembrolizumab | After 1st dose | - | 4 | 6 | **0.67** | 0 | 0.67 | - | **9.33** |
| P 19 – 2 |  |  |  |  | On treatment | - | 6 | 8 | **0.75** | 0.5 | 0.25 | - | **3.75** |
| P 19 – 3 |  |  |  |  |  | - | 1 | 8 | **0.12** | 0 | 0.12 | - | **17.62** |
| P 19 – 4 |  |  |  |  |  | - | 58 | 6 | **9.67** | 1.33 | 8.33 | - | **16.83** |
| P 19 – 5 |  |  |  |  |  | - | 8 | 8 | **1** | 0.62 | 0.25 | 0.12 | **7.5** |
| P 19 – 6 |  |  |  |  | After | - | 1 | 6 | **0.17** | 0.17 | 0 | - | **20.5** |
| P 20 | M | 76 | adeno. | Pembrolizumab | On treatment | - | 43 | 6 | **7.16** | 0.16 | 6.83 | 0.16 | **30** |
| P 21 | F | 51 | adeno. | Avelumab | On treatment | - | 24 | 6 | **4** | 0.5 | 3.5 | - | **20** |
| P 22 | M | 74 | squamous | Pembrolizumab | On treatment | - | 2 | 8 | **0.25** | 0 | 0.25 | - | **5** |
| HD 01 | F | 57 | Healthy | - | - | - | 2 | 4 | **0.5** | - | - | - | **14** |
| HD 02 | M | 55 | Healthy | - | - | - | 5 | 4 | **1.25** | - | - | - | **30.75** |
| HD 03 | M | 20 | Healthy | - | - | - | 0 | 2 | **0** | - | - | - | **18.5** |
| HD 04 | M | 23 | Healthy | - | - | - | 2 | 6 | **0.33** | - | - | - | **12** |
| HD 05 | M | 35 | Healthy | - | - | - | 5 | 6 | **0.83** | - | - | - | **19.3** |
| HD 06 | F | 69 | Healthy | - | - | - | 6 | 6 | **1** | - | - | - | **17.3** |
| HD 07 | F | 77 | Healthy | - | - | - | 2 | 6 | **0.33** | - | - | - | **27.6** |
| HD 08 | F | 41 | Healthy | - | - | - | 4 | 6 | **0.66** | - | - | - | **21.3** |
| HD 09 | M | 69 | Healthy | - | - | - | 1 | 6 | **0.16** | - | - | - | **29** |
| HD 10 | F | 60 | Healthy | - | - | - | 3 | 6 | **0.5** | - | - | - | **13.83** |

**Table 4-1. Patient cohort, clinical information, and cell enumeration.** 31 patient blood samples and 10 healthy donor samples were processed through Vortex technology. These 31 samples were collected from 22 different NSCLC patients: 5 squamous, 17 adenocarcinoma, with 17 blood samples collected pre-treatment, 2 after the first cycle, and 11 during the treatment. 15 samples had ≥ 10 CTCs and were considered for further study, with 4 of them having a biopsy of the primary tumor available. (PDL1+), (PDL1-) and (UD) respectively indicate the number of CTCs per mL that are either identified as PD-L1 positive, PD-L1 negative or undetermined.

### 4.2.2. Isolation of CTCs using Vortex technology

We used a microfluidic device for rapid, size-based capture of CTCs from blood called the Vortex HT chip, as previously described by the authors (23) (Figure 4-1.A). The Vortex HT chip utilizes inertial microfluidic flow to isolate CTCs within microscale vortices. Captured cells are then released and collected off-chip in a well plate for fixation and immunostaining.

### 4.2.3. Cells lines and WBCs

Lung cancer cell line staining controls A549 (adenocarcinoma), H1703 (squamous carcinoma) and H3255 (adenocarcinoma) were cultured in RPMI media supplemented with 10% FBS and 1% pen/strep. Hela cells were cultured with DMEM media supplemented with 10% FBS and 1% pen/strep. At 70% confluence, cells were harvested using 0.25% trypsin and fixed with 2% paraformaldehyde. White blood cells (WBC) were isolated from healthy blood using RBC lysis buffer (eBioscience). WBCs were similarly fixed with 2% paraformaldehyde. During each staining experiment, an aliquot of each of these fixed cell solutions were stained in the same well-plate alongside with the CTC samples for normalization.

### 4.2.4. Immunofluorescence staining of circulating tumor cells

Collected cells were fixed with 2% paraformaldehyde (Electron Microscopy Sciences) for 10 min, permeabilized with 0.4% v/v Triton X-100 (Research Products International Corp) for 7 min, blocked with 5% goat serum (Invitrogen) for 30 min. To identify CTCs, cells were labelled for 40 minutes at 37ºC with 4,6-diamidino-2-phenylindole (DAPI) (Life Technologies), anti CD45-phycoerythrin (CD45-PE, Clone HI30, BD Biosciences), and a cocktail of primary antibodies to identify cytokeratin (CK) positive cells (Pan-CK clone AE1/AE3, eBioscience, clone CK3-6H5, Miltenyi Biotec, and CK clone CAM5.2, BD Biosciences). To identify PD-L1 levels, cells were also stained with anti-PDL1 antibody (ProSci Inc), A secondary antibody labeled with Alexa Fluor 647 was used as the fluorescent reporter for the PD-L1 antibody. One set of control cells consisting of A549, H1703 and healthy white blood cells (WBCs) were stained along with each patient sample. These controls were necessary to normalize for the staining process, antibody batch, and microscope conditions over the length of the study and report fluorescent intensities that could be compared between CTCs from many samples. The staining protocol for PDL1 was optimized to positively stain lung cancer cell lines (Figure 4-4). After staining, the cells were imaged (Axio Observer Z1, Zeiss) and manually enumerated using specific classification criteria. We identified CTCs in patient samples based on

DAPI+/CK+/CD45-, or DAPI+/CK-/CD45-/ along with cytopathological features of malignancy as described previously (23). All CTC and WBC counts were checked by two independent reviewers (Table 4-1). PD-L1 expression on these CTCs was quantified using a semi-automated algorithm as described below. Some CTCs could not be evaluated for PD-L1 expression (identified as “UD” in Table 4-1) due to the presence of fluorescent debris overlapping the cells in the PD-L1 Cy-5 channel.

### 4.2.5. Immunohistochemistry of lung tumor biopsies

Immunohistochemistry was performed by the UCLA TPCL Pathology core. Briefly, thin tumor sections were cut from paraffin tissue blocks of biopsies obtained prior to treatment (Figure 4-1.B). The slides were deparaffinized in xylene and re-hydrated through graded ethyl alcohols (100% x3, 95%x2) to distilled water; initially xylene for about 10 min and the remaining treatments for 1 minute each with agitation. Antigen retrieval was performed in a pressure cooker (5 minutes at max temperature) in high pH Tris-EDTA buffer and samples were cooled for 15 minutes at room temperature after pressure returned to atmospheric pressure. The slides were incubated with primary antibody (rabbit monoclonal anti-PDL1 clone SP142, Sina Biological, at 1/200 dilution) for 60 minutes followed by anti-rabbit, horseradish peroxidase polymer (Refine detection kit from Leica) for 15 minutes. The slides were washed with buffer after each of the primary antibody and polymer steps and then incubated with hydrogen peroxide/diaminobenzidine for 10 minutes. Cells were counterstained with hematoxylin. Biopsy tissues were only available for analysis from 4 patients.

### 4.2.6. Quantification of PD-L1 levels on CTCs and tumor samples

In order to quantify PD-L1 expression on CTCs, we developed a semi-automated imaging algorithm using a custom MATLAB script. The script was used to quantify the cell sizes and normalized fluorescence levels for each cell from each patient sample (Figure 4-2). Briefly, an edge detection algorithm was used to locate the outline of the cell membrane (from the transmitted light image) and convert the outline to a binary image mask. The mask was then overlaid against the fluorescence images from each channel and utilized to identify the fluorescence per pixel in each cell. The sum of the pixel intensity of the PD-L1 channel (Alexa Fluor 647) in the area identified as the cell was calculated for each CTC, and ~100 control cells of each type. To normalize the fluorescence intensity of the CTCs, we utilized the lung cancer line H1703 as these cells had the highest expression of PD-L1 of the three lung cancer lines used (A549, H1703, and H3255) (24). Staining a fixed batch of these cells along with each sample, allowed normalization of the CTC data. We use the following equation to calculate the normalized intensity:

$$\frac{\left(\sum_{n=1}^{\#\,of\,pixels}\left(I_{pixel\,of\,CTC}-local\ background\right)\right)}{\frac{1}{K}\sum_{N=1}^{K}\left(\sum_{n=1}^{\#\,of\,pixels}\left(I_{pixel\,of\,a\,H1703\,cell}-local\ background\right)\right)},$$

where $I$ is the pixel value and $K$ is the total number of H1703 cells analyzed. This value shows the relative intensity of PD-L1 expression on CTCs to that of H1703 cells. If the CTC has much higher expression than H1703, then the normalized value would be greater than 1. Once the CTC fluorescence intensities were normalized, they were categorized as PD-L1 negative (normalized intensity between 0-0.05) or PD-L1 positive. The quantity of PD-L1 expression was further categorized as either low (normalized intensity between 0.05-0.4), medium (0.4-0.7), or high (>0.7) as defined in the cutoff values in Figure 4-5.B. These descriptor bins were set initially by visual inspection.

To quantify PD-L1 expression on the tumor biopsy sections when available, the thin biopsy specimens were analyzed using the positive pixel count algorithm in HALO software (Indica Labs). The intensity signal from each cell was categorized as negative for PD-L1 expression (intensity between 0-0.04) or as positive (0.04-1). Positive cells were further categorized into low (intensity between 0.04-0.1), medium (0.1-0.2) and high levels (0.2-1), as indicated by the cutoff values shown in Figure 4-5.B. The lymphocytes at the periphery of the tumor were excluded by the software based on the cell size and nucleus.

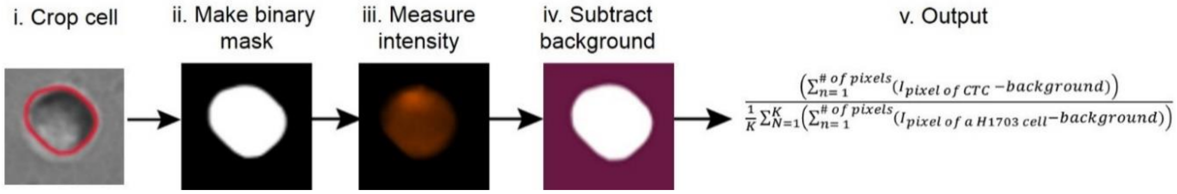

**Figure 4-2 Semi-automated quantification of fluorescence.** A semi-automated image detection algorithm was developed in MATLAB to quantify the PD-L1 intensity on individual cells. After cells were manually classified as either CTCs or WBCs, their centers were marked. (i) The algorithm used these center coordinates to crop a 80x80 pixel box around the cells, both WBCs and CTCs. (ii) An edge detection algorithm located the outline of the cell membrane (from the transmitted light image) and then made a binary image mask. (iii) The mask overlay on the fluorescence images was used to identify the fluorescence intensity per pixel in each cell. (iv) The local background was subtracted. (v) The sum of all pixel intensity in the PD-L1 channel in the overall area identified as being the cell and control cells of each type was calculated. The final normalized PD-L1 intensity value included the sum of intensity per cell divided by the average integrated intensity for H1703 cells stained in parallel.

## 4.3. Results

### 4.3.1. CTCs can be enriched from NSCLC patient blood samples

We first confirmed that CTCs could be enriched from metastatic NSCLC patients with Vortex technology. A total of 22 patients were enrolled in this study, with 31 samples collected, processed with Vortex technology and enumerated for CTCs. 30/31 (96.8%) samples had at least 1 CTC, 15/31 (48.4%) samples at least 10 CTCs, with CTC total counts ranging from 0.1 to 9.67 CTCs/mL of blood (Table 4-1, Figure 4-3.B). Besides the CTCs, between 1 and 93 WBCs were collected per mL, which indicates a high-purity (Table 4-1, Figure 4-3.C). As negative controls, we tested blood samples from 10 healthy volunteers, male and female, of different ages (Table 4-1, Figure 4-3.B). Using the same enumeration criteria described for the patients, 0 to 1.25 cells per mL were isolated from healthy controls and characterized as CTCs. Based on these enumeration data, a “healthy” cut-off value was defined as the mean number of CTCs + 2SD, calculated to be 1.32 CTCs/mL. Using this threshold, 14 of 31 patient samples (45%) were considered positive for CTCs.

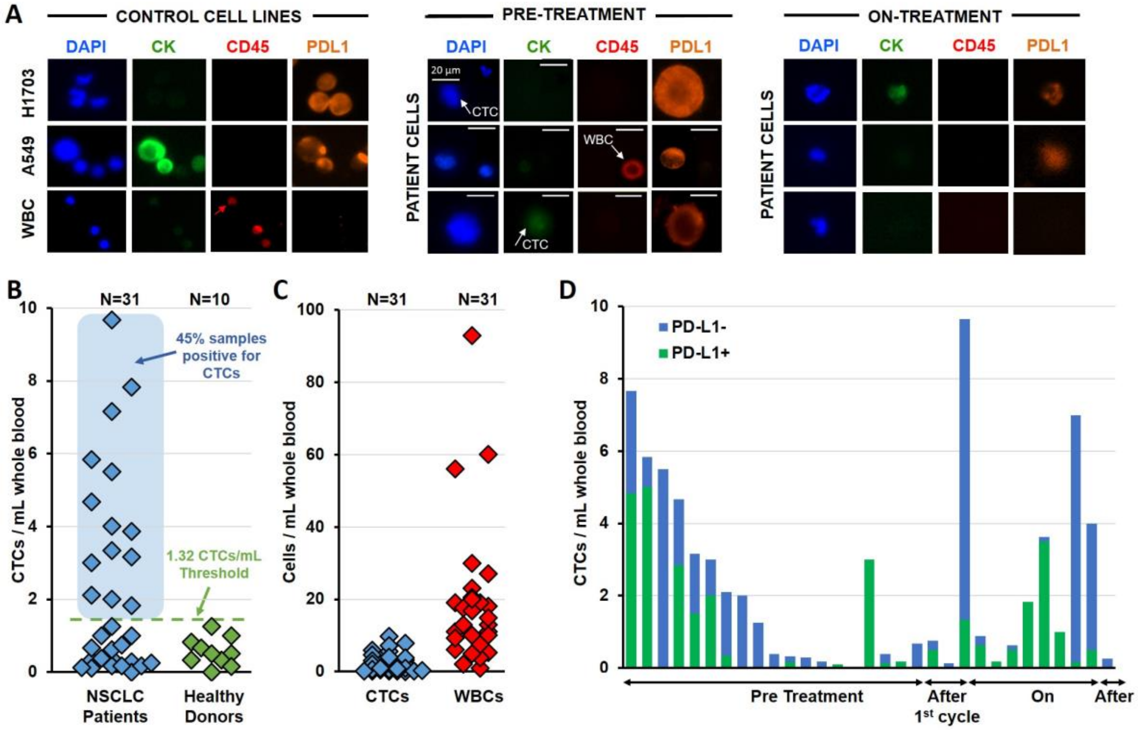

**Figure 4-3. CTC Immunostaining, enumeration, and PD-L1 expression analysis.** (A) Gallery of cells collected through Vortex technology from patient samples. Healthy WBCs and lung cancer cell lines are used as staining controls. Cells were immunostained for PD-L1-AF647, CK-FITC, CD45-PE and DAPI, then classified according to quantitative criteria previously published (23). (B) Following this method, 10 healthy donors blood samples and 31 samples from 22 patients were processed and CTCs enumerated. A healthy threshold can be defined from the healthy donors as 1.32 CTCs/mL (average + 2SD). Using such a threshold, 14 of 27 patient samples were positive for CTCs (52%). (C) CTCs are collected with high purity, with 0 - 9.67 CTCs/mL among 1 – 93 WBCs/mL. (D) CTCs display varying levels of PD-L1 expression.

### 4.3.2. PD-L1 can be quantified on CTCs prior to treatment with PD-1 inhibition

We then developed a method for quantifying PD-L1 expression on lung cancer cells using immunofluorescence staining. To identify the optimal primary and secondary antibody concentrations, we utilized HeLa cells as a positive control and RBCs as a negative staining control for PD-L1 (Lee) We tested three commercially available PD-L1 antibodies (ProSci Ref# 4059, BioLegend clone: 29E.2A3, and eBioscience clone: MIH1) and determined that the ProSci antibody had the most intense specific staining while maintaining the least non-specific staining (Figure 4-4.A).

We used the three lung cancer cell lines A549, H1703 (adenocarcinoma), and H3255 (squamous cell carcinoma) to develop and validate the PD-L1 fluorescence immunostaining protocol and quantification algorithms. The H1703 line was found to have the highest overall expression of PD-L1 while H3255 had minimal to no PD-L1 expression (Figure 4-4.B-C); we thus decided to use H1703 as the positive staining control, whereas leukocytes (WBC) were used as the negative staining control.

Once these parameters had been determined, we then implemented this protocol to quantify PD-L1 expression on the isolated lung cancer patient CTCs; with examples of patient sample staining shown in Figure 4-3.A. For each patient, the number of CTCs positive and negative for PD-L1 were counted (Table 4-1, Figure 4-3.D). Of patient samples with CTCs, 30/31 had one or more PD-L1+ CTCs (Figure 4-3.D). The fraction of PD-L1 positive CTCs among these patients ranged from 2.2 to 100% (Table 4-1, Figure 4-3.D).

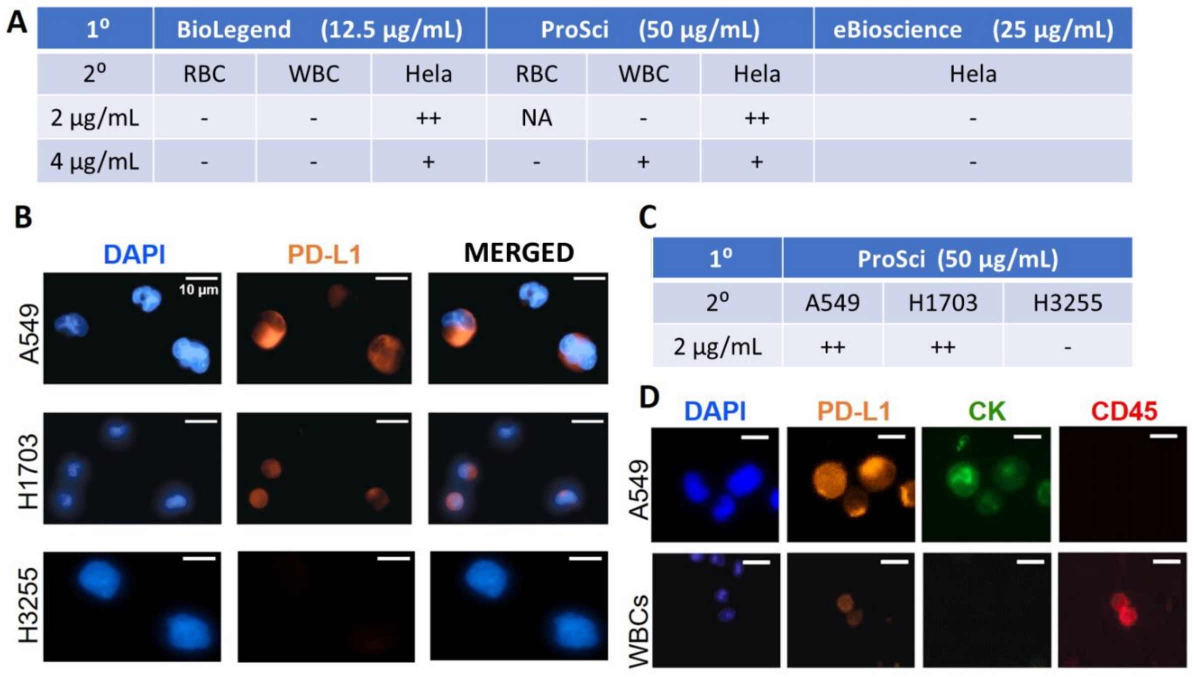

A

| $1^{o}$ | BioLegend (12.5 μg/mL) | | | ProSci (50 μg/mL) | | | eBioscience (25 μg/mL) |
|---|---|---|---|---|---|---|---|
| $2^{o}$ | RBC | WBC | Hela | RBC | WBC | Hela | Hela |
| 2 μg/mL | - | - | ++ | NA | - | ++ | - |
| 4 μg/mL | - | - | + | - | + | + | - |

C

| $1^{o}$ | ProSci (50 μg/mL) | | |
|---|---|---|---|
| $2^{o}$ | A549 | H1703 | H3255 |
| 2 μg/mL | ++ | ++ | - |

**Figure 4-4. Optimization of PDL-1 immunostaining.** (A) Several antibody brands were first tested with RBCs, WBCs, and HeLa cells: BioLegend, ProSci, and eBioscience. ProSci was chosen as it provided the highest staining intensity. (B, C) Using the optimal conditions of anti-PDL1 (ProSci Inc) at a concentration of 50µg/mL, and goat anti-rabbit Alexa Fluor 647 (Cell Signaling) at a concentration of 2µg/mL, respectively as primary and secondary antibodies, PDL-1 staining was tested on several lung cancer cell lines: A549 (adenocarcinoma), H1703 (adenocarcinoma), H3255 (squamous) and WBCs as a control. (D) Once validated, patient samples were stained for PD-L1, CK, CD45, DAPI. CTCs were identified using a classification criterion previously described (23). For each CTC sample, 2 independent controls were used to confirm the validity of the staining: A549 as positive expression for PD-L1 and CK, WBCs as positive control for CD45.

### 4.3.3. PD-L1 expression on tumor biopsy sections can be quantified and compared with CTC expression prior to treatment

We next examined the concordance of PD-L1 staining between CTCs and tumor biopsy sections, as PD-L1 positivity in these sections has been shown to be a predictor for outcome in lung cancer and the PD-1 inhibitor pembrolizumab requires a patients' tumor biopsy to be positive for PD-L1 prior to administration (as determined by an FDA-approved companion diagnostic). Tumor biopsies prior to treatment were only available for 4 patients from the 22 patients in this study. For these 4, thin sections of tumor were cut from the paraffin block, stained and the resulting PD-L1 levels quantified as described above. Sample images for negative, low, medium, and high PD-L1 staining are shown in Figure 4-5.A. Although all 4 tumor biopsies were initially scored as PD-L1 positive, we quantified PD-L1 levels and found that the majority of positive cells had low expression (Figure 4-5.C). Patient P07 had the lowest fraction of medium (7.64%) and high (0.46%) staining cells in the corresponding biopsy, with 91.9% of the cells being either low or negative for PD-L1. This was reflected within the CTCs as well, as P07 had the lowest fraction of PD-L1 positive CTCs (15.8%, i.e. 3 of 19, these 3 cells being even identified as low PD-L1 expression). Two patients (P05 and P06) with the highest fraction of positive PD-L1 cells in their tumor (P05: 99.5%, P06: 99.9%) also had the highest fraction of PD-L1 positive CTCs (P05: 47.4%, P06: 66.7%), with a significant part of CTCs having medium or high PD-L1 expression (P05: 26.3%, P06: 12.5%) and (P06: 4 of 24 in P06). For Patient P01, tumor and CTCs provided again a similar pattern, with respectively 18.6% and 37% of the tumor cells and CTCs being PD-L1 negative, while 67.3% and 63% of the cells were PD-L1 positive but with a low expression level. Interestingly, for all 4 patients, the fraction of CTCs that were negative for PD-L1 staining was always higher than the fraction of negative cells in the corresponding biopsy.

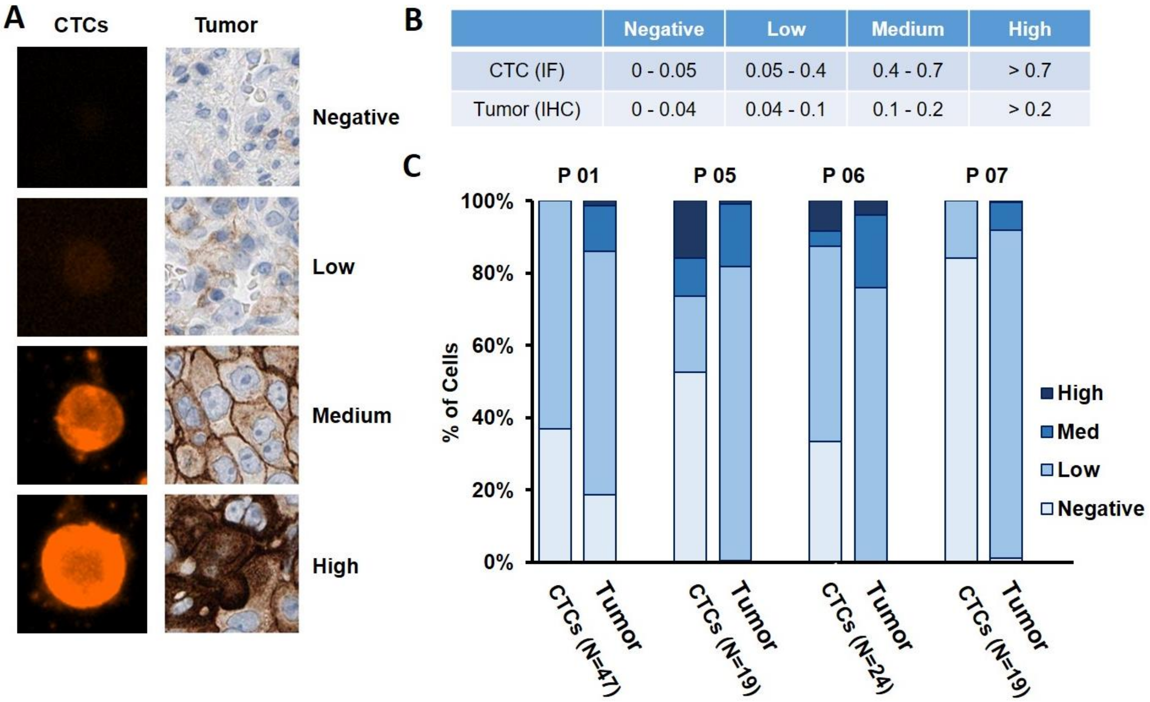

| | Negative | Low | Medium | High |
|---|---|---|---|---|
| CTC (IF) | 0 - 0.05 | 0.05 - 0.4 | 0.4 - 0.7 | > 0.7 |
| Tumor (IHC) | 0 - 0.04 | 0.04 - 0.1 | 0.1 - 0.2 | > 0.2 |

**Figure 4-5. Comparison of PD-L1 expression in CTCs and matched primary tumor prior to anti-PD1 immunotherapy.** (A) Tumor specimens were analyzed by IHC staining for PD-L1, using DAB Peroxidase (HRP) staining technique. PD-L1 tumor score is the percentage of cells in each category: negative, low, medium, high. CTCs were analyzed by IF and semi-automated quantification of PD-L1 staining intensity (Figure 4-4), with CTC intensity normalized by the average staining intensity of H1703 as a control cell line. (B) PD-L1 CTC threshold level and IHC PDL1 threshold levels are quantified based on the percentage of cells in four different categories. (C) Bar plots showing percentage and PD-L1 level of matched tumor biopsy and CTC specimens (n=4 patients).

Although for this initial study, we did not serially collect blood in all patients, we did so for two patients (Patients #16 and 19, Figure 4-6). For Patient P19, the first collection was after the first dose of pembrolizumab (Figure 4-6.top). The patient continued to receive pembrolizumab as he was having decrease in tumor burden as measured by radiographic scan. However, a blood draw two and a half month after the first draw revealed an increase in CTC count from 0.67 to 9.67 CTCs/mL, with a low fraction of PD-L1+ CTCs (13.7%) (Table 4-1). Imaging conducted one month later demonstrated new brain metastases; the patient expired one year later. For Patient P16, 5 blood draws were collected at the beginning and during the course of avelumab therapy. Tumor burden was measured as well and decreased over time. Patient was indicated as stable at the last CT scan. During the 5 blood draws, CTC number varied from 0.62 to 3.87 CTCs/mL, but always with high proportion of the

CTCs being PD-L1 positive (between 80.6% and 100%). Interestingly, at the exact beginning of the PD-L1 inhibitor therapy, 100% of the CTCs collected were defined as PD-L1 positive. Despite the longitudinal study of only 2 patients, these cases suggest that CTC number and potentially PD-L1 expression may correlate with clinical status and response to inhibitor therapy. Further work will involve serially tracking patients to see how CTC monitoring (both total and PD-L1+ CTC level) may help to predict efficacy or loss of efficacy of treatment.

**P 19**

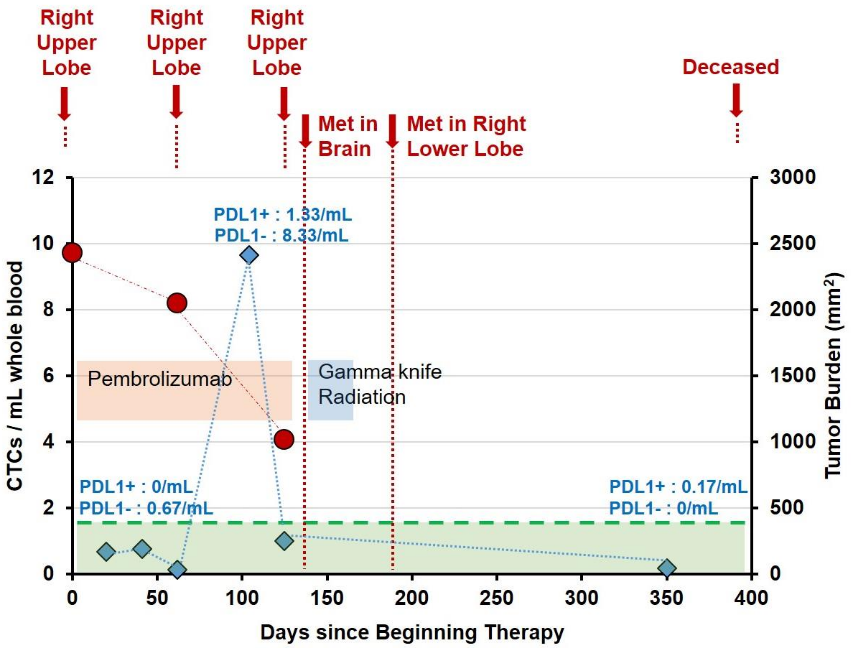
Right Upper Lobe
Right Upper Lobe
Right Upper Lobe
Met in Brain
Met in Right Lower Lobe
Deceased
PDL1+ : 1.33/mL
PDL1- : 8.33/mL
Pembrolizumab
Gamma knife Radiation
PDL1+ : 0/mL
PDL1- : 0.67/mL
PDL1+ : 0.17/mL
PDL1- : 0/mL
CTCs / mL whole blood
Tumor Burden (mm$^2$)
0
2
4
6
8
10
12
0
500
1000
1500
2000
2500
3000
0
50
100
150
200
250
300
350
400
Days since Beginning Therapy

**P 16**

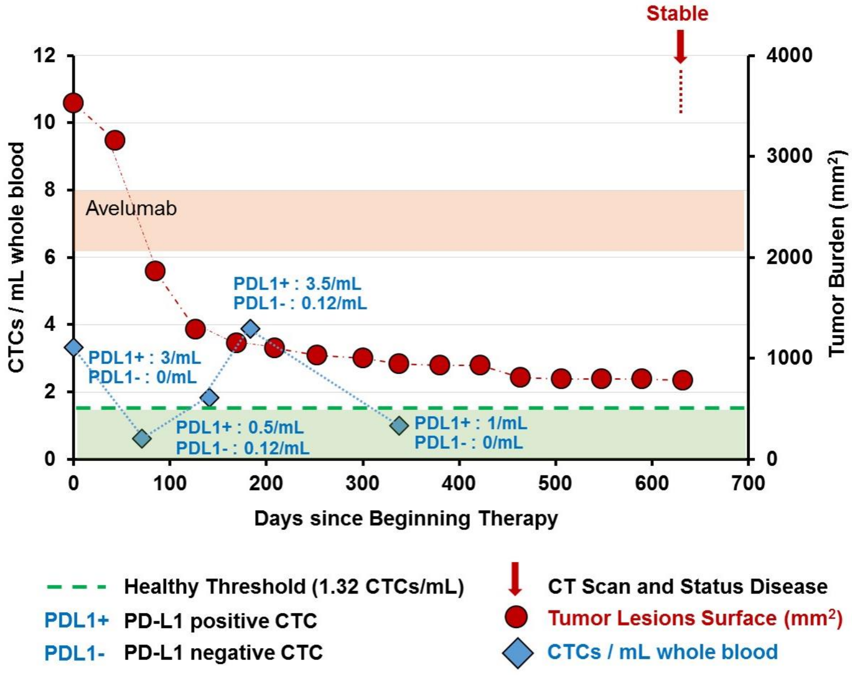
Stable
Avelumab
PDL1+ : 3.5/mL
PDL1- : 0.12/mL
PDL1+ : 3/mL
PDL1- : 0/mL
PDL1+ : 0.5/mL
PDL1- : 0.12/mL
PDL1+ : 1/mL
PDL1- : 0/mL
CTCs / mL whole blood
Tumor Burden (mm$^2$)
0
2
4
6
8
10
12
0
1000
2000
3000
4000
0
100
200
300
400
500
600
700
Days since Beginning Therapy
Healthy Threshold (1.32 CTCs/mL)
PDL1+ PD-L1 positive CTC
PDL1- PD-L1 negative CTC
CT Scan and Status Disease
Tumor Lesions Surface (mm$^2$)
CTCs / mL whole blood

**Figure 4-6. CTC counts during the clinical course and treatment of Patients 16 and 19, since initiation of treatment.** Orange and blue bars represent periods when patients were receiving inhibitor therapy, either avelumab or pembrolizumab and radiation respectively. Green dotted line represents the healthy threshold of 1.32 CTCs/mL above which patients are defined as positive for CTCs. Blue marker indicates the CTC number at the time of blood collection, with indication of PD-L1 positive and negative CTCs. The red circle marker indicates the tumor burden, i.e. the index tumor lesions summed cross-sectional area. (Top) In Patient P19, tumor burden initially decreased over time indicating a shrinking of the right upper lobe tumor and a potential response of the patient to the treatment. However, the patient soon after was found on imaging to have developed metastases to the brain and lung, which was preceded by the increase of CTC number from 0.67 to 9.67 CTCs/mL. The patient died at day 538. (Bottom) In Patient P16, tumor burden decreased over time and was stable at the last time point. CTC number varied from 0.62 to 3.87 CTCs/mL but always with a high proportion of the CTCs being PD-L1 positive (between 80.6% and 100%).

## 4.4. Discussion

Immunotherapy may represent a breakthrough in the treatment of selected cancers and specific patients. Despite the efficacy of therapies like ipilimumab, nivolumab, and pembrolizumab, only a fraction of patients responds. In metastatic NSCLC, the overall response rate is approximately 20% (7, 14). Although several studies have indicated that selected biomarkers (such as tumor PD-L1 expression or the presence of CD8+ infiltrating lymphocytes) are correlated with patient response, there is still a need for other ancillary and non-invasive biomarkers that can predict response and/or be used to monitor response to ultimately help guide the treatment course. CTCs have recently gained momentum as a non-invasive liquid biopsy for monitoring of treatment response and as a source of genetic material to understand treatment failures. Although the analysis of circulating cell-free tumor DNA (ctDNA) is also being explored, especially in identifying the presence of known druggable mutations, such an approach is not suited for identifying phenotypic changes such as levels of PD-L1 on tumor cells. There are no known consistent genetic lesions associated with up-regulated expression of PD-L1. Also, a variety of other cell types express PD-L1 (for example macrophages (13)) and could release protein, extracellular vesicles, or mRNA into the blood stream. CTCs are ideally suited to characterize PD-L1 expression through a non-invasive liquid biopsy in that they are short-lived markers of the active invasive tumors, with holistic phenotypic and proteomic information.

This study represents one of the first to examine PD-L1 expression on NSCLC CTCs in the context of anti-PD1/PD-L1 treatment. Some of the newly approved checkpoint inhibitors either require (pembrolizumab) or strongly encourage (nivolumab) a companion diagnostic indicative of tumor positivity for PD-L1 prior to administration. So, in this pilot study, we wished to determine whether CTC PD-L1 expression was correlated with tumor expression and also indicative of response. We also developed several algorithms to quantify PD-L1 expression on CTCs and tumor biopsies respectively and utilized these to compare PD-L1 levels in matched liquid and tumor biopsies. Although PD-L1 expression alone was not predictive of progression free survival, we did note several potentially important trends in CTC count and PD-L1 expression. Even given a limited sample size, we did note that for patients with >10 CTCs, those with >50% PD-L1+ had improved overall response (3 of 4 patients). Heterogeneity of PD-L1 levels could indicate intra-tumoral or intra-patient heterogeneity, as each of these patients had multiple metastatic sites and the CTCs could break off from any or multiple of these sites.

Nevertheless, the trends we find here are suggesting that PD-L1 status on CTCs may track that of tumor tissue and that this may be a useful correlate in helping to assess potential for response to immunotherapy. However an assessment of tumor infiltrating lymphocytes are likely a much better indicator of potential response to immunotherapy.

One limitation of this study or any CTC study in general is that it can be difficult to draw correlations with few cells, and excluding samples with <10 cells led to a total sample size that was smaller. In many cases, CTCs are present prior to treatment but their numbers can be limited, due in part to previous chemotherapeutic treatment or the fundamental patient-to-patient heterogeneity of tumor behavior. This fundamental issue is exacerbated by practical challenges with the limited number of patient samples that are available from patients on clinical trials for new therapies.

## 4.5. Conclusions

CTC PD-L1 levels when combined with the tumor biopsy results could aid in identifying patients likely to respond to therapy or likely to have become resistant to treatment when tracking levels over time. This study indicates that continued work is warranted to analyze and compare more CTC samples from patients on anti-PD-1 pathway treatment to more robustly determine how PD-L1 expression correlates to tumor levels, fluctuates in response to treatment, and is predictive of response. The methods we describe here are potentially applicable to any tumor type and to potentially any treatment course, as the size-based approach does not exclude cells on the basis of presence or absence of surface markers and the size selectivity criteria can be tuned based on the cancer type known to be present.

## 4.6. References

1. Verdegaal EM*, et al.* (2016) Neoantigen landscape dynamics during human melanoma-T cell interactions. *Nature*.
2. van Rooij N*, et al.* (2013) Tumor exome analysis reveals neoantigen-specific T-cell reactivity in an ipilimumab-responsive melanoma. *J Clin Oncol* 31(32):e439-442.
3. Topalian SL, Taube JM, Anders RA, & Pardoll DM (2016) Mechanism-driven biomarkers to guide immune checkpoint blockade in cancer therapy. *Nat Rev Cancer* 16(5):275-287.
4. Ribas A (2012) Tumor immunotherapy directed at PD-1. *N Engl J Med* 366(26):2517-2519.
5. Ribas A (2015) Adaptive Immune Resistance: How Cancer Protects from Immune Attack. *Cancer Discov* 5(9):915-919.
6. Brahmer JR*, et al.* (2012) Safety and activity of anti-PD-L1 antibody in patients with advanced cancer. *N Engl J Med* 366(26):2455-2465.
7. Garon EB*, et al.* (2015) Pembrolizumab for the treatment of non-small-cell lung cancer. *N Engl J Med* 372(21):2018-2028.
8. Larkin J*, et al.* (2015) Combined Nivolumab and Ipilimumab or Monotherapy in Untreated Melanoma. *N Engl J Med* 373(1):23-34.
9. Motzer RJ*, et al.* (2015) Nivolumab versus Everolimus in Advanced Renal-Cell Carcinoma. *N Engl J Med* 373(19):1803-1813.
10. Topalian SL*, et al.* (2012) Safety, activity, and immune correlates of anti-PD-1 antibody in cancer. *N Engl J Med* 366(26):2443-2454.

11. Lisberg A & Garon EB (2016) The Value of PD-L1 Testing in Non-Small-Cell Lung Cancer. *JAMA Oncol*.
12. Sacher AG & Gandhi L (2016) Biomarkers for the Clinical Use of PD-1/PD-L1 Inhibitors in Non-Small-Cell Lung Cancer: A Review. *JAMA Oncol* 2(9):1217-1222.
13. Tumeh PC*, et al.* (2014) PD-1 blockade induces responses by inhibiting adaptive immune resistance. *Nature* 515(7528):568-571.
14. Herbst RS*, et al.* (2016) Pembrolizumab versus docetaxel for previously treated, PD-L1-positive, advanced non-small-cell lung cancer (KEYNOTE-010): a randomised controlled trial. *Lancet* 387(10027):1540-1550.
15. Gettinger S*, et al.* (2016) Nivolumab Monotherapy for First-Line Treatment of Advanced Non-Small-Cell Lung Cancer. *J Clin Oncol*.
16. Mazel M*, et al.* (2015) Frequent expression of PD-L1 on circulating breast cancer cells. *Mol Oncol* 9(9):1773-1782.
17. Cristofanilli M*, et al.* (2004) Circulating tumor cells, disease progression, and survival in metastatic breast cancer. *N Engl J Med* 351(8):781-791.
18. Danila DC*, et al.* (2007) Circulating tumor cell number and prognosis in progressive castration-resistant prostate cancer. *Clin Cancer Res* 13(23):7053-7058.
19. Sollier E*, et al.* (2014) Size-selective collection of circulating tumor cells using Vortex technology. *Lab Chip* 14(1):63-77.

20. Anantharaman A*, et al.* (2016) Programmed death-ligand 1 (PD-L1) characterization of circulating tumor cells (CTCs) in muscle invasive and metastatic bladder cancer patients. *BMC Cancer* 16(1):744.
21. Satelli A*, et al.* (2016) Potential role of nuclear PD-L1 expression in cell-surface vimentin positive circulating tumor cells as a prognostic marker in cancer patients. *Sci Rep* 6:28910.
22. Nicolazzo C*, et al.* (2016) Monitoring PD-L1 positive circulating tumor cells in non-small cell lung cancer patients treated with the PD-1 inhibitor Nivolumab. *Sci Rep* 6:31726.
23. Che J*, et al.* (2016) Classification of large circulating tumor cells isolated with ultra-high throughput microfluidic Vortex technology. *Oncotarget* 7(11):12748-12760.
24. Stanciu LA*, et al.* (2006) Expression of programmed death-1 ligand (PD-L) 1, PD-L2, B7-H3, and inducible costimulator ligand on human respiratory tract epithelial cells and regulation by respiratory syncytial virus and type 1 and 2 cytokines. *J Infect Dis* 193(3):404-412.
25. Hodi FS*, et al.* (2016) Evaluation of Immune-Related Response Criteria and RECIST v1.1 in Patients With Advanced Melanoma Treated With Pembrolizumab. *J Clin Oncol* 34(13):1510-1517.
26. Wolchok JD*, et al.* (2009) Guidelines for the evaluation of immune therapy activity in solid tumors: immune-related response criteria. *Clin Cancer Res* 15(23):7412-7420.

27. Dhar M*, et al.* (2015) High efficiency vortex trapping of circulating tumor cells. *Biomicrofluidics* 9(6):064116.

# Chapter 5. Functional Analysis of Protease Secretion from CTCs

## 5.1. Introduction

Thus far we have discussed immunofluorescent based methods for CTC characterization and enumeration. Here we present a new assay that goes beyond the static measurement of protein expression, and allows us to interrogate secretions from CTCs.

Although the presence of CTCs is correlated with the aggressive spread of a tumor, and negative prognosis in breast, colon, and prostate cancer, using current methods to identify CTC number based on immunofluorescence (IF) staining has led to mixed success in predicting disease state following treatment[58–61]. For example, surface marker identified CTC number did not predict treatment effectiveness in clinical tries done with the CellSearch system[62]. Heterogeneity in CTC phenotype is likely one contributing factor in discrepancies between CTC counts and prognosis. Many CTCs shed from tumors during treatment with cytotoxic agents may in fact be non-viable, and not all CTCs are expected to possess a phenotype optimized for extravasation and spread. An extravasation-competent phenotype is hypothesized to include high motility and deformability to squeeze through cell and extracellular matrix (ECM) layers, low cell-adhesiveness, and high protease secretion to degrade ECM barriers [63]. Potentially, the measurement of MMPs or other proteases secreted by CTCs can improve prognosis of cancer aggressiveness and help determine the relative importance of CTC protease secretion in extravasation and metastasis. Understanding the activity of MMPs and other proteases secreted by CTCs may also provide new, more selective, targets for anti-metastatic therapies, whereby the measurement approaches described could serve in a companion diagnostic role to indicate when treatment is warranted.

Measuring the secretions of individual CTCs is extremely challenging given the rarity of CTCs and the significant dilution of the few secreted molecules from single cells when isolated into a large volume of solution. Current techniques that enable measurement of single-cell secretions confine cells into a small volume of surrounding fluid using microwells or droplet microfluidics[64,65]. Both techniques increase the concentration of the secreted analyte by orders of magnitude, which increases the sensitivity of the system. However, current microwell and drop-generating systems are not integrated with purification or solution exchange operations necessary to measure secretions of individual cells without background contamination or significant cell loss in transfer steps [66–70]. This may limit analyses to non-rare populations of cells. As an example, Yao et al. used a microwell plate system to measure MMP and PSA secretions from CTCs isolated using RosetteSep. As they mention, many CTCs are during negative depletion in RosetteSep, and some cells lose viability due to the long processing time for serial steps of CD45 positive cell depletion, RBC lysis, and several washes. The series of manual steps in RosetteSep takes approximately 1 hour to complete[71]. During the 1 hour time frame cells can modify their protein expressions and degrade mRNA[72]. Droplet generating systems offer a high throughput technique that is easier to integrate into cell isolation systems, and they allow downstream sorting based on a secretion profile with established techniques such as fluorescence-activated droplet sorting (FADS).

Two main classes of droplet generators have been applied to single-cell encapsulation- (i) an aqueous/oil co-flow geometry where droplet size depends on flow rate and (ii) step emulsification designs where droplet size has been shown to be less dependent on flow rate, making them more amenable to integration [73–76]. Flow focusing droplet generators have been used to encapsulate immortalized cancer cells and leukocytes and measure protease production [67,68,77]. [67,68,77]. Jing et al. highlight the importance of washing out background proteases in media or plasma around cells to obtain a cell-specific signal without substantial background fluorescence. Their device achieves washing by transitioning a stream of sample with leukocytes into a reaction buffer using deterministic lateral displacement (DLD). The droplet generator junction is located downstream of the reaction buffer channel. Due to the continuous generation of droplets, a large number of empty droplets are made during the entire sample processing time [78]. In a rare cell analysis application, a very small percentage of droplets would therefore have cells in them which would lead to extreme imaging and analysis times. These droplet platforms are compatible with cell lines and applications focusing on abundant cells; however, they are difficult to adopt for analyzing CTCs or other rare cells in large volumes of clinical blood samples with huge numbers of background cells. In order to study protease activity and release by CTCs, an integrated system that can isolate CTCs from blood, wash away contaminating blood cells and plasma, introduce new reagents, and encapsulate them into droplets without manual transfer steps will be enabling.

We have developed a technology we term Size based Purification and Encapsulation of Cells (SPEC) that integrates functions of isolation, reagent exchange, and isolation for single-cell secretion analysis of rare cells. The integrated device performs vortex trapping of larger rare circulating tumor followed by single-cell encapsulation using a novel extreme throughput droplet generator to measure proteases secreted by individual cells. Integration enables a whole blood sample to isolated CTCs in under 15 minutes, better preserving physiologic state of cells.. We characterize the sensitivity of the system to collagenase enzymes and find sensitivity down to ~ 7 molecules per droplet. We evaluate the differences in MMP secretion across a range of cancer cell lines and other circulating cells as well as demonstrate sensitivity to identify pharmacological interference of MMP secretion. Finally, we evaluate the secretions of CTCs and other circulating cells from late stage prostate cancer patients. We find that although heterogeneous, some CTCs from cancer patients actively secrete MMPs over a three hour time period after isolation. These results indicate cells may secrete these enzymes in vivo and open up the capability to study secretions from these unique cells. Such assays may ultimately lead to CTC secretions as a functional profiling approach for drug selection in the future.

## 5.2. Methods

### 5.2.1. Immunostaining

Prior to CTC isolation we stain whole blood samples directly in EDTA collection tubes to identify subpopulation of cells. For every 6mL of blood we use 10µL CD45-PE (BD Bioscience cat # 555483), 10µL CD66c-PE (eBioscience cat # 12-0667-41), 10µL PSMA-APC (Miltenyi Biotec cat # 130-106-609), and 6 µL of 50µg/mL Hoechst (Thermo Fisher H3570). All antibodies target surface epitopes such that membrane permeabilization is not necessary for access to each protein. We add the antibodies to 6mL of whole blood in the collection tube protected from light at room temperature for 30 minutes.

### 5.2.2. Vortex device operation

After staining the blood, we dilute it 20X in filtered PBS immediately before processing through the vortexHE chip. The vortexHE chip isolates CTCs from diluted whole blood at 2.6 mL/min. During CTC isolation the wash buffer and substrate runs at 0.3 mL/min and the sample runs at 2 ml/min. The wash and substrate needs to be on infuse mode to prevent blood backflow into the solutions. These flow rates were optimized for 20mL BD plastic pack syringes, processed on a Harvard apparatus syringe pump (cat # 71-2001).

After CTC trapping in vortices, a solution exchange to PBS washes out background molecules. While the wash buffer runs at 2.4 ml/min the sample withdraws simultaneously at a low flow rate of 0.1ml/min. The sample withdraw prevents remaining blood from infusing in the chip and contaminating the signal. After a 1 minute wash, we stop the wash buffer flow, and switch the substrate flow to 2.7 ml/min, this second solution change introduces the substrate. After 4 seconds the vortices fill with the substrate. We determined the time required to completely fill the vortices from high speed imaging of trypan blue as a contrast agent in the vortex chambers. The substrate is a peptide sequence FRET (Fluorescence Resonance Energy Transfer) based broad spectrum MMP substrate from AAT Bioquest (cat # 13510); it is specific for 11 different MMPs. We used a 0.5% dilution in RPMI base media (Invitrogen cat #11875119) of the stock substrate. For all MMP9 specific experiments, we used a different peptide FRET substrate from Biozyme (cat # PEPDAB052m001) at 10µM dilution in RPMI.

Once the substrate replaces all the solution around the cells, we divert captured cells to the second outlet of the pinch valve leading to a droplet generator. The valve switches the flow towards the droplet generator at time 0. At this time, the fluid splits between the forward vortex exit direction and the disengaged sample syringe. We can tune the ratio of flow split by reducing the resistance in the sample syringe tubing. By using a large lumen tubing for the sample, we can rapidly slow flow towards the vortex exit by driving a larger portion of the flow towards the sample syringe. The pinch valve has two input tubes, one is normally pinched in the off position while the other is open. The input of the droplet generator connects to the normally off tube, while the second tube goes to the waste outlet. When the valve receives 24V input, the switch alters pinch position such that the output from the Vortex chip goes to the droplet generator, and the waste tube is pinched off. The vortices dissipate when we release the actuation on the sample syringe and lower the substrate flow to 0.05 ml/min. The release step runs for 10-15 seconds, while the cells get encapsulated into droplets. The step emulsifier is highly parallelized with 100 channels, which allows it to operate at very high flow rates. Initially the droplet generator is 50% full with 0.5% pico-surf (Sphere Fluidics, cat # SF-000149) in Novec 7500 (3M, cat # 9802122937), and held at a 90-degree angle to allow droplets to move away from the inlet region and allow more droplets to form. After encapsulation, the droplet generator is filled completely with the 0.5% pico-surf in

Novec 7500 and put in a horizontal position. This allow the droplets to form a monolayer. The sequence of steps used is shown in Figure 5-1.

The reaction between protease and substrate occurs inside the droplets for 3 hours. After this incubation step we image the droplets in the reservoir. Imaging for all cell line experiments was done using the Axio Observer Z1 Zeiss fluorescence microscope, all imaging for the clinical samples were done using Nikon Ti-E fluorescence microscope. Both microscopes used Nikon CoolSnap HQ2 cameras. The substrate fluoresces in the FITC channel and was imaged with a 400ms exposure. An image processing algorithm was developed in MATLAB to detect the boundary of the droplets in brightfield and calculate the intensity of the secreted MMPs in the FITC channel. Droplets with specific cells in them were identified before calculating the fluorescent intensity. The SNAIL transfected cells contained GFP, therefore the cell area was masked and not included in calculating the fluorescent intensity of the droplets.

### 5.2.3. Cell line experiments

Cancer cell lines A549, HCC827, H1703, and LnCaP were cultured in RPMI media supplemented with 10% fetal bovine serum (FBS) and 1% penicillin-streptomycin- glutamine (P/S) at 37°C with 5% $CO_2$. VCaP cells were grown in DMEM (Thermo Fisher cat# MT-10-013-CM), 10% FBS, and 1% P/S. PC3 cells were grown in F-12K (Invitrogen cat # 21127022), 10% FBS, and 1% P/S. Endothelial cells were grown in MCDB131 complete growth media (VEC Technologies cat # MCDB131C). Once the cells were semi confluent, they were lifted from their adherent layer using 0.25% Trypsin EDTA (Gibco) and 3 minutes incubation at 37°C. The trypsin was neutralized with media and cells were spun down at 2300 rpm for 5 minutes, VCaP and endothelial cells were spun at 300g for 5 min. The trypsin and media were removed and the cells were suspended back in media before processing.

*Cell line spiking in PBS*

Cells were suspended in media and stained for viability with 1µM calcein red-orange (Thermo Fisher cat # C34851). Cell concentration was determined by hemocytometer and diluted to 100 cells per ml in PBS and 5ml of this cell solution was processed.

*Cell treatment with histamine*

A confluent flask of endothelial cells was grown in vascular basal media (Vascular Cell Basal Medium (ATCC PCS-100-030) for 16 hours. Then cells were put in suspension and processed for encapsulation. Cells were encapsulated with 10µM histamine that was added to the diluted substrate solution.

*Cell treatment with Monensin and Brefeldin*

A semiconfluent flask of PC3 cells were used. Protein Transport Inhibitor Cocktail (eBioscience cat # 00-4980-03) is a cocktail of monensin and brefeldin A. The stock solution of 500X was diluted to 2X and added to the growth media. The cells were incubated in 37ºC with 5%$CO_2$ for 15 hours before the cells were lifted and encapsulated intro droplets with the same concentration of the transport inhibitor dissolved along with the substrate solution.

### 5.2.4. Device fabrication

Devices were made with the polymer polydimethylsiloxane (PDMS) using replica molding. The vortexHE device is fabricated using methods described previously [49]. The droplet generator is fabricated using double layer photolithography. The mold structure was fabricated on a 4 inch silicon wafer (University Wafer Inc.) by photolithograpy. For the first layer containing the channels, KMPR 1050 (Microchem) was spun coated with spin speed of 3500 rpm, ramped at 300 rpm/s for 30s for 50µm heights and 30µm widths and 1000 µm lengths. Devices were soft baked for 15 minutes at 100ºC and cooled for 5 minutes. The exposure time was 120s at 8.5W power. They were post exposure baked for 3 minutes at 100ºC. The devices were cooled for 5 minutes on metal cooling bench. The second layer of KMPR was spun at 900 rpm ramped at 300 rpm/s for 30s, soft baked for 20 minutes. The wafer was cooled for 5 minutes and a third layer of KMPR was poured and previous step was repeated. The wafer was then protected from light and cooled for at least 15 hours at room temperature. The masks were aligned using alignment marks and the wafer was exposed for 200s. The post exposure bake was done for 10min. The wafer was cooled for 5 minutes, and developed using SU-8 developer. The container with the wafer and developer was put in a sonicator for 2 minutes, removed and unexposed photoresist was removed by agitation. The reservoirs had a height 500 µm – 1000 µm. Device features were measured with a Dektak profilometer. The PDMS droplet generator device was made with Sylgard 184 Elastomer (Dow Corning Corporation) with a cross-linker to polymer ratio of 1:10, and cured at 60°C for 21 hours. The devices were cut from the mold, and entry ports were punched using a 1.5mm biopsy needle (Integra Miltex cat # 33-38). The PDMS layer and a glass slide (VWR International, LLC) were $O_2$ plasma treated (Oxford Technics RIE) (for 30 seconds, at 500 mTorr, 80 W power before being bonded together to enclose the microchannels.

## 5.3. Results

### 5.3.1. Cell trapping and subsequent encapsulation into droplets

The CTC isolation component of our device consists of a series of channels that expand and contract to develop stable laminar vortices. Larger cells, such as CTCs, are stably trapped within the microvortices that form in the expansion regions, while smaller red and white blood cells enter but do not form stable limit cycles or orbits[37]. We then exchange solutions while under continuous flow to wash out plasma proteins and leave pure cells within a continuously exchanging reaction buffer (fluorogenic MMP-cleavable peptide substrate), reducing any nonspecific signals. The trapped cells are released along with the MMP-cleavable substrate into an inline connected droplet generator where they are encapsulated into uniform microdroplets without any manual transfer steps (Figure 5-1). The entire process, from cells starting in whole blood to encapsulation in droplets along with MMP detection reagent, is complete in less than 15 minutes.

Due to the seamless transition of fluid and cells, we have minimal loss of cells through all steps of the process (Figure 5-2c). The initial concentration step in microvortices dominates the yield of cells with an efficiency of >40% for spiked cancer cells. Further concentration is achieved through single-cell encapsulation, in which the overall efficiency is decreased slightly but remains >35%. Through this series of automated steps on chip we transfer rare cells from 20ml of diluted blood volume (1mL of whole blood) into individual droplets with a volume of ~2nL, and thus increase the concentration of trapped cells and their secreted molecules by six orders of magnitude. Importantly, the first vortex-based concentration step achieves an initial concentration of the diluted sample, such that a small number of droplets (<50,000) contain the captured cells reducing the analysis time.

Cell secreted proteases and the fluorescent reaction products accumulate in the 2nL droplets during an incubation period. Following incubation, we analyze the fluorescent intensity in each droplet using a fluorescent microscope or an imaging flow cytometer and correlate intensity in droplets to intensity of other cellular markers of each encapsulated cell. This approach allows us to investigate single-cell secretions of proteases from CTCs with high purity and low noise, and should be amenable to other single-cell secretion, genomic and proteomic analyses on CTCs with a seamless workflow.

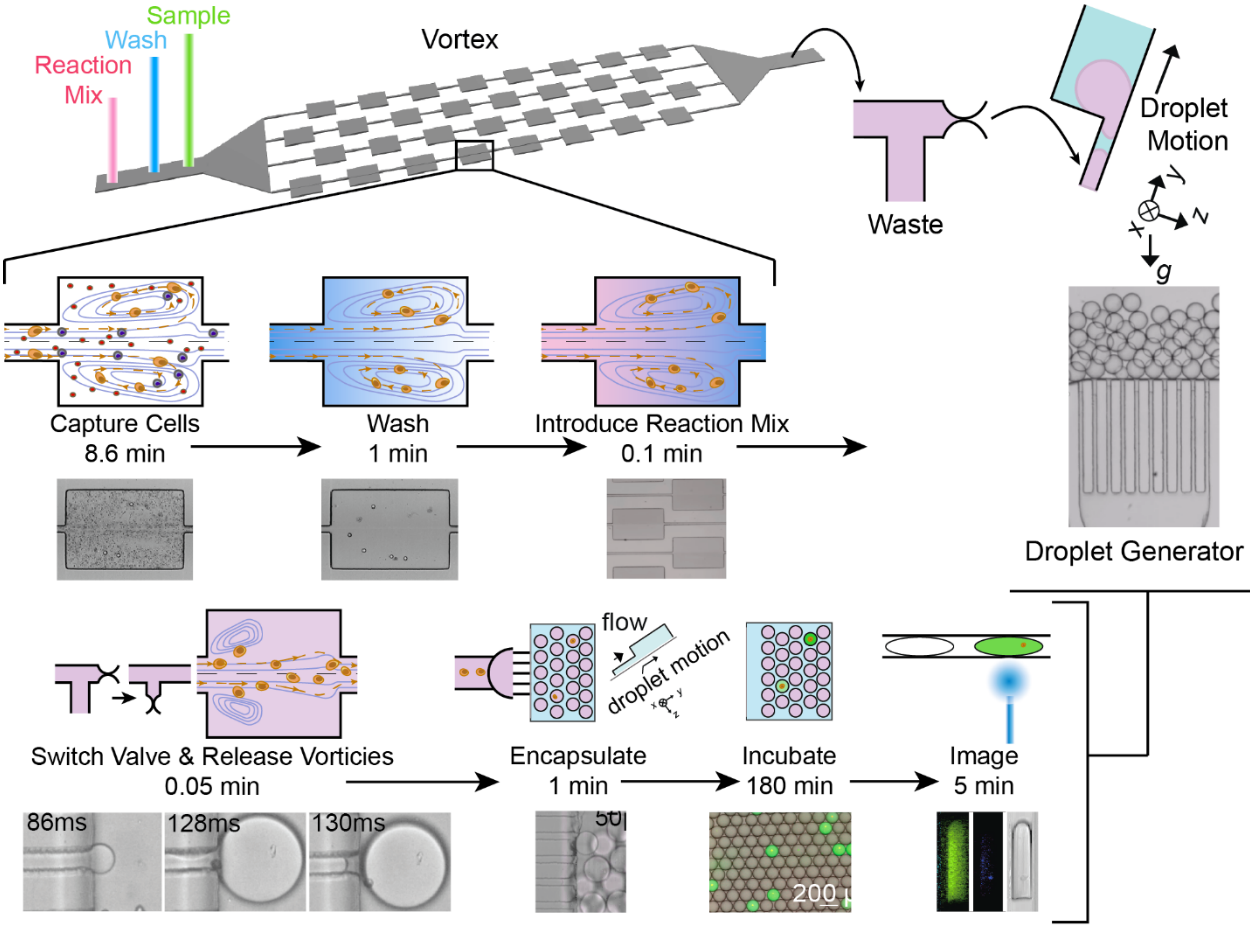
Sample
Wash
Reaction Mix
Vortex
Waste
Droplet Motion
y
z
x
g
Capture Cells
8.6 min
Wash
1 min
Introduce Reaction Mix
0.1 min
Droplet Generator
Switch Valve & Release Vorticies
0.05 min
86ms
128ms
130ms
flow
droplet motion
Encapsulate
1 min
50
Incubate
180 min
200
Image
5 min

**Figure 5-1.** Size based Purification and Encapsulation of Cells (SPEC) followed by fluorescence analysis of enzyme secretion. Large cells are trapped in microvortices, background smaller cells and molecules are then washed away with a wash buffer. After clearing background cells and enzymes, an MMP cleavable peptide substrate is introduced through solution exchange in the vortex. By lowering the flow rates, the vortices are allowed to dissipate, releasing captured cells. A pinch valve prevents extraneous droplets from being generated during the cell trapping process, but is opened in synchrony with vortex dissipation. At this stage the valve directs the flow towards the droplet generator and allows cells to be encapsulated with substrate solution in microdroplets. The droplets float away from the generation region due to buoyancy differences with the oil. The oil reflows back towards the inlet allowing continued droplet generation. The cells can then be incubated and imaged in the large reservoir section of the droplet generator. An imaging cytometer can also be used to image the droplets and contained cells in flow.

We developed a new droplet generator design that operates in a highly parallel manner, with low flow rate sensitivity and without any oil co-flow to be compatible with the variable flow rates during release of cells from the vortex device. Figure 5-2a provides a plot of the flow rate decay at the exit channel over time as the vortices dissipate indicating that the operating conditions should span an order of magnitude in flow rates from ~ 0.3 to 0.03 mL/min. As shown in Figure 5-2b the droplet generator stably produces relatively monodisperse droplets (CV = 4%) in the flow rate range from 0.001 ml/min to 0.003 ml/min per channel with dimensions of

50µm height and 30µm width. The droplet generator included 100 channels, to generate drops over the release flow rates while maintaining uniform size. Beyond this range polydispersity increases in the droplets, and eventually the flow jets and no droplets form above 0.006 ml/min per channel.

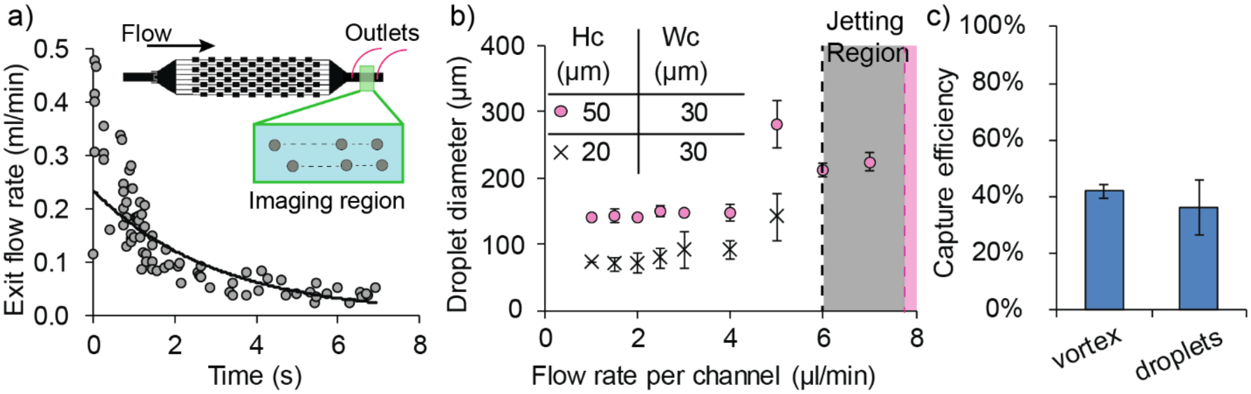

**Figure 5-2. Merging vortex-based cell release and step emulsification**. a) Flow rate decays quickly when the pressure is released to dissipate the vortices. Beads tracked in the exit region of the vortex were used to calculate the decay in flow. b) Droplet generation remains stable and monodisperse at flow rates from 0.001 ml/min to 0.003 ml/min per channel, while beyond these rates the droplet generation becomes unstable and polydisperse. These values were used to design parallel channels that would generate small stable droplets. c) There is minimal loss between the cells captured in the vortex device and the cells in the droplets because of the continuous flow integrated system.

### 5.3.2. Assay characterization

To characterize our protease secretion assay in droplets we first used purified collagenase (MMP1) introduced with the FRET based MMP cleavable peptide substrate in droplets. We evaluated the time-course of enzyme activity, detection limits and repeatability of the assay using known concentrations of collagenase. Over the course of three to seven hours, droplets loaded with an average 700 collagenase molecules and 0.5% diluted MMP substrate show enzyme activity saturates after three hours (Figure 5-3). The 0.5% substrate dilution is optimal and yields the highest signal for MMPs secreted by cells, therefore this dilution was used for all experiments (Figure 5-4a). For the same amount of substrate and three-hour incubation time, higher amounts of collagenase show more than six orders of magnitude intensity increase. The plateau in response of the collagenase molecules between 3 and 7 hours suggests the collagenase becomes inactivated, potentially through a self-digestion process. Past studies suggest collagenase contains a stretch of peptide sequence similar to its substrate which implicates its self-processing.[38,39] As concentration of collagenase increases, the signal is distinct from ~7 molecules to ~3x10$^5$ collagenase molecules per drop, and saturates beyond this point. These results indicate that the 0.5% diluted substrate is in excess when <~3x10$^5$ enzymes are used in the reaction. We assume single cells would release proteases within this detection regime. The linear correlation between intensity and number of molecules per droplet could be used to estimate the number of molecules secreted by single cells (Figure 5-3a).

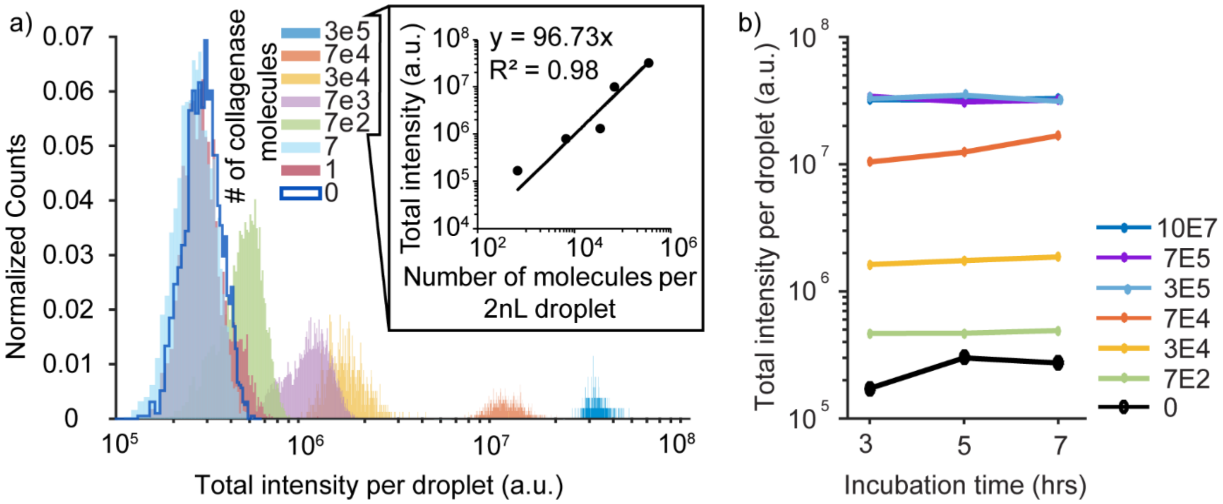

**Figure 5-3. MMP assay performance**. a) We test the detection limits of the assay using serial dilutions of known concentrations of collagenase. We find Poisson loading of droplets occurs at low concentrations where most droplets are empty and a few have enough collagenase to generate a signal. A linear correlation exists between droplet intensity and number of molecules reacted for greater than 700 molecules per droplet, indicating a large dynamic range for detection. These correlations can be used to extrapolate the minimal number of molecules secreted by single cells. b) The assay can clearly distinguish between a starting concentration of 100s to 300,000 collagenase molecules. The signal becomes indistinguishable and saturated for concentrations of greater than 300,000 molecules per droplet.

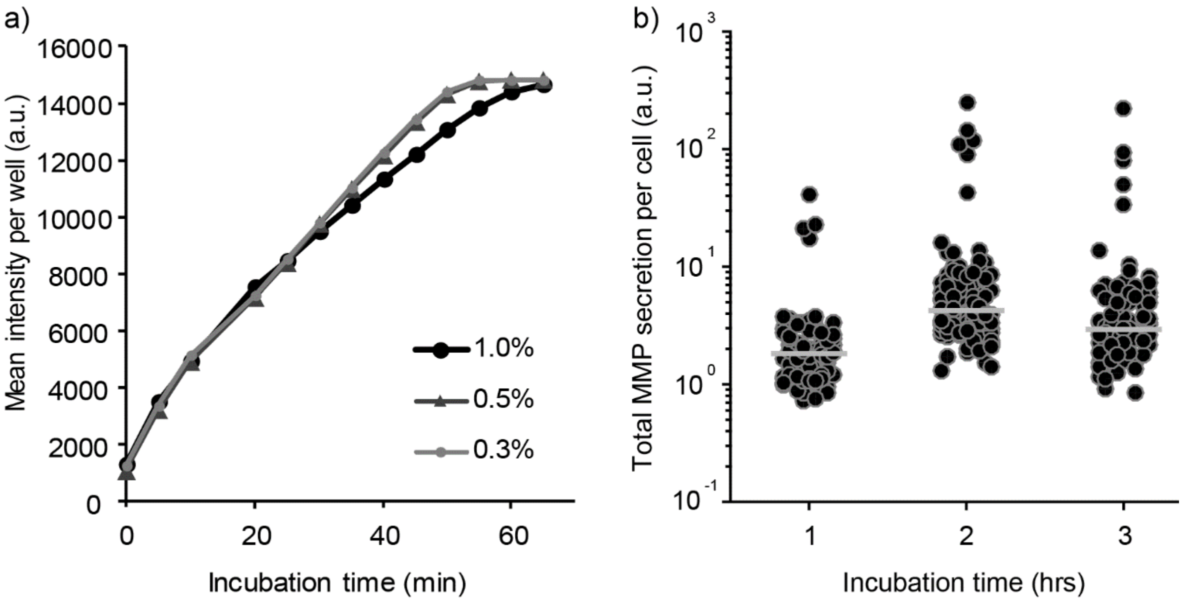

**Figure 5-4**. a) Three different concentrations of the substrate solution were used to measure substrate turnover. A549 cells were incubated in serum free media for 24 hours. The cells secreted MMPs into this media. The media containing the MMPs were mixed with the substrate at 0.25% to 1% dilutions and used to determine the best substrate concentration to use. The 0.5% MMP substrate had the higher turnover and signal generated by the MMPs from the A549 cells than the other dilutions. b) Several A549 cell secretions were tracked over a 3 hour time period. Over time cells secrete at different rates and increase the heterogeneity in secretion. The amount of secretion saturates at 3 hours.

### 5.3.3. Detection of single cell protease secretion

In order to model protease secretion from liquid biopsies, we used cancer cell lines and endothelial cells all of which are known to circulate and express MMPs [6,40–44]. A subpopulation of these cells secretes proteases after vortex capture and incubation for three hours. The fluorescent substrate remains contained in the droplets and does not leak out into surrounding empty droplets within three hours (Figure 5-6), however, longer incubation times may cause some amount of fluorescent substrate to transport into empty drops. Within 3 hours, the signal from cells also start to saturate (Figure 5-4b). These cells were alive as indicated by the positive intracellular calcein signal. Cells in which fluorescent cell tracker leaked out into the surrounding droplet were considered permeabilized during the processing and dying and therefore not included in our analysis. The empty droplets were used as an internal negative control, and used to normalize the intensity of each droplet. These negative controls eliminated variations in the optical system or auto fluorescence from PDMS. The baseline values are the median from several empty droplets. The intensity of empty droplets from cells in droplet experiments have similar levels as true negative droplets with only diluted substrate and no MMPs, indicating the use of empty droplets is a good measure of baseline values (Figure 5-5). Thus, droplets with intensities above the normalized baseline value of ‘1’, have a positive signal above background.

The fluorescence intensity of droplets encapsulating single cells possess a non-normal distribution with variation in the distribution shape depending on cell line. A549 cell secretion assays have comparable variance between different days and batches of the MMP substrates (Figure 5-8). The droplets having lower than “1” normalized values are likely due to the variance in substrate loading in droplets with non-secreting cells. At least an order of magnitude range of variation exists in the empty droplets. We determined the variation is not due to the differences in the droplet sizes. Figure 5-12a shows that the intensity variation on the droplets are not correlated with the droplet diameter.  Here we use the Gini coefficient to quantify the level of heterogeneity in the cell populations. The coefficient varies from 0 to 1, 0 being the case where all cells produce the same amount of protease, and 1 being the case where the cells have a high difference between the amounts of proteases produced. The cancer cells have a large heterogeneity, with a Gini coefficient ranging from 0.7 to 1 as well as a number of high secreting outlier cells. The prostate cancer lines VCaP, LnCaP, and mesenchymal stem cells have a much smaller Gini coefficient ranging from 0.13 to 0.68 with more cells secreting above baseline levels in a more homogeneous manner. Endothelial cells also have a low Gini coefficient (0.29), they have less outliers, and overall secrete less than the cancer cells.

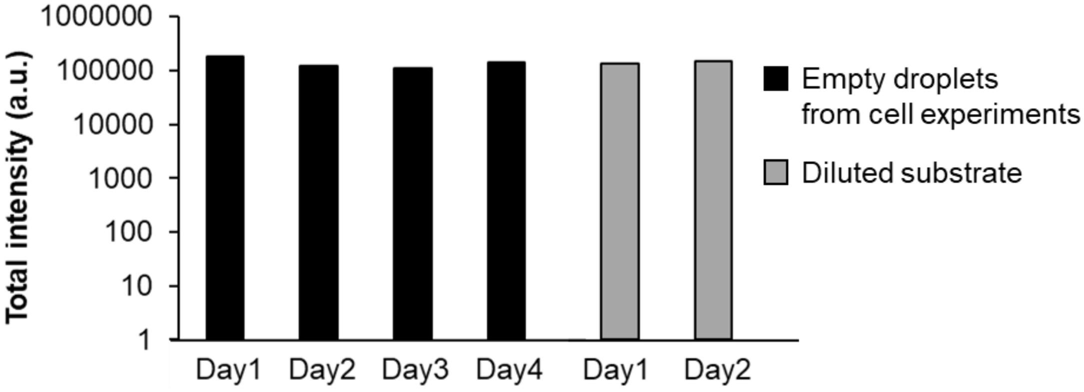

**Figure 5-5. Baseline values**. The baseline values are calculated from empty droplets. Empty droplets from cells in droplets experiments have similar levels as droplets from control experiments with only diluted substrate. Intensity values of droplets with only substrate and no MMPs (grey) are comparable to those with potential MMPs present from secreting cells (black).

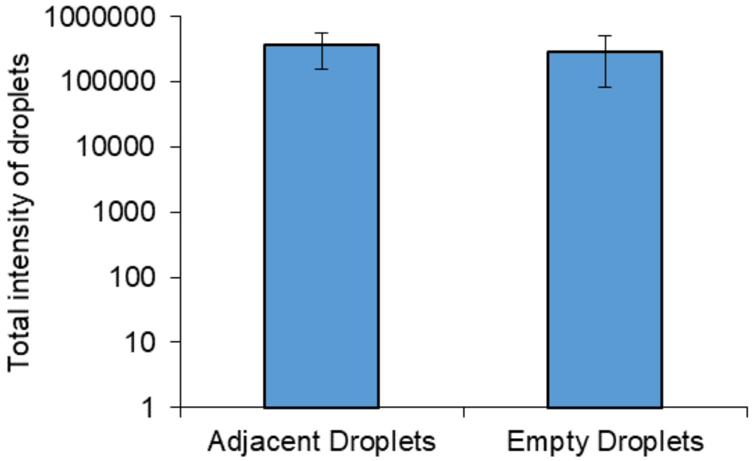

**Figure 5-6**. There is no significant transport of cleaved peptide substrate within the three hour incubation period. Adjacent droplets are droplets neighboring droplets surrounding a droplet containing an A549 cell that is secreting MMPs. In order to accurately quantify the amount of protease being secreted by cells, it is important that the end product generating the signal does not transport out of the droplets.

Cell secretions accumulate in droplets over time, however, a shorter time window ensures a cellular phenotype closer to the in vivo physiology. Theoretically longer incubation time would allow cells to secrete more proteases. We find that cells are still alive after 20 hours of incubation based on live staining, and the assay is able to determine the secretion from these cells. However, we find that following a 20 hour incubation time the background fluorescence increases due to the substrate nonspecifically degrading over time and a degree of fluorescent molecule leakage out of the droplets. Considering these factors, we determined significant results can be observed within a shorter 3 hour incubation window.

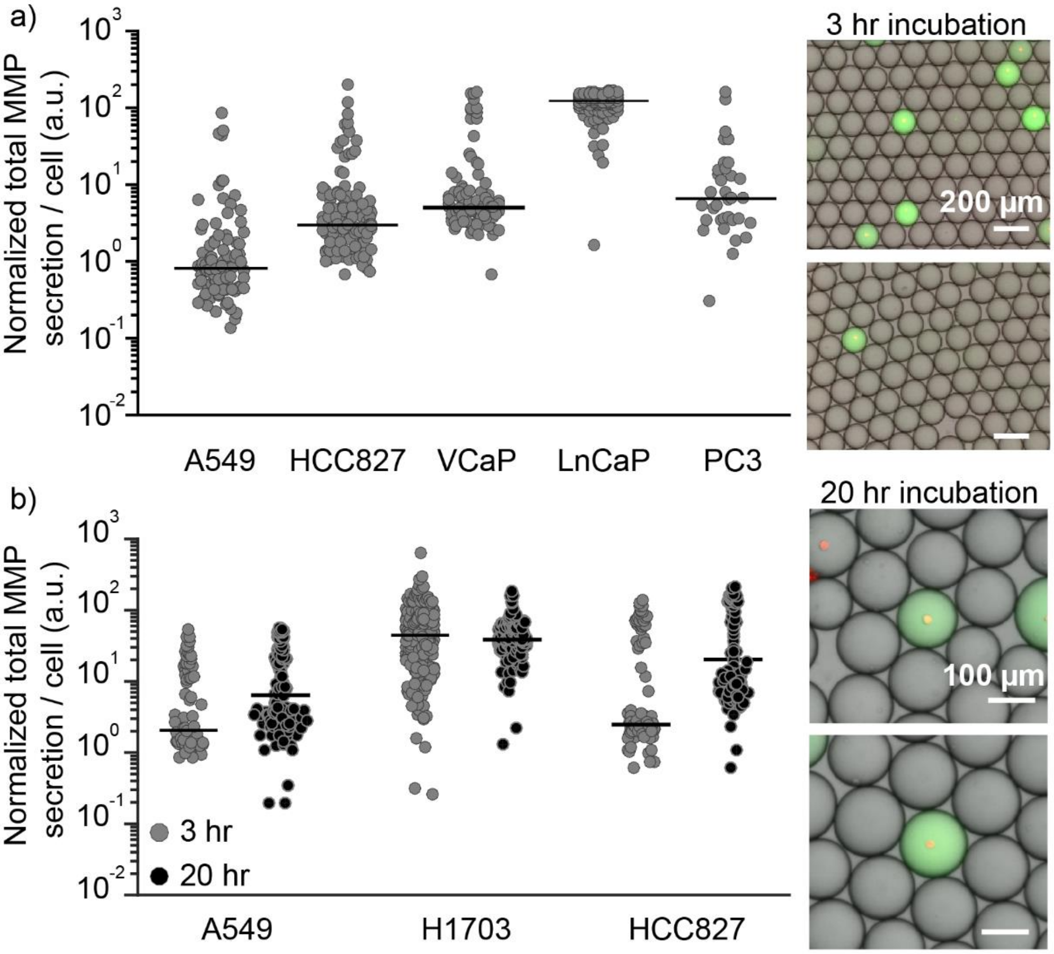

**Figure 5-7**. a) MMP secretion levels vary amongst cell lines. Lung cancer cell lines (A549, HCC827), prostate cancer cell lines (VCaP, LnCaP, and PC3) as well as endothelial cells secrete varying levels of MMPs. These cells were also stained with calcein to distinguish cell viability. Only droplets with single viable cells were measured. Cells that were dying had fluorescent calcein leak out into the surrounding droplet, and were not analyzed. The empty droplets were used as an internal negative control. We also observe a large variation at the single-cell level within a cell line. b) Lung cancer cells were interrogated for MMP secretion at 3 hours and 20 hours. There is no significant difference in signal generated by secretions over this time frame for A549 cells. However H1703 and HCC827 have some significant differences in secretion over a longer period of time.

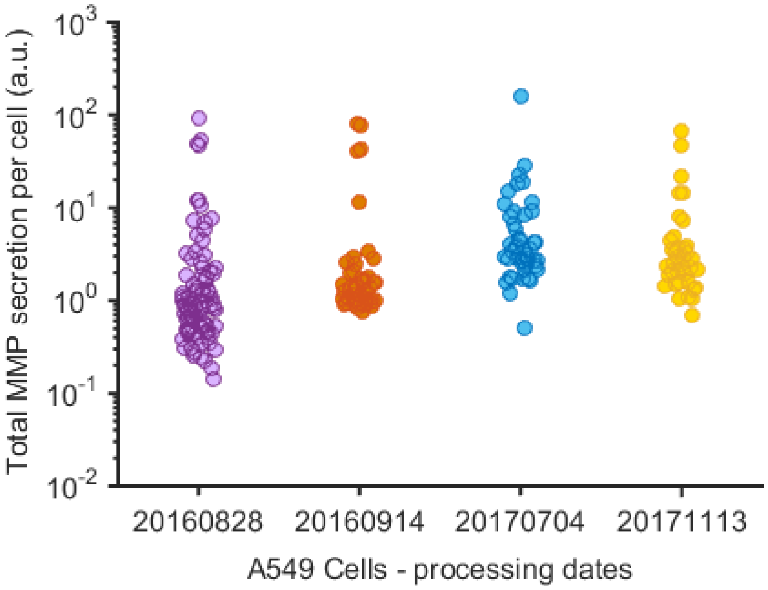

**Figure 5-8**. Assay repeatability. The A549 secretion assays have comparable variance between different days and batches of the MMP substrates. The droplets having lower than “1” normalized values are likely due to the variance in substrate loading in droplets with non-secreting cells. The droplets with cells also have a lower amount of substrate than empty droplets due to the excluded volume effect from the cells. These factors may contribute to lower intensity values in droplets with non-secreting cells than empty droplets.

### 5.3.4. Detecting modulation of single-cell MMP secretions

We conducted a series of experiments to up- and down-regulate MMP secretion and determined the ability to capture these phenotypes with our single-cell assay. Upregulation of the transcription factor SNAIL has been shown to modulate MMP-9 and MMP-2 secretion and transition cells towards mesenchymal phenotype [45,46]. We observed that MMP-9 secretion is either upregulated or remains the same in this assay (Figure 5-9). MMP upregulation can also be achieved through the exposure of endothelial cells to histamine. Histamine interacts with the H2 receptor on endothelial cell surface and has been found to trigger MMP secretion [47]. We find a 58% increase in secretion in cells treated with 10µM Histamine.

We also characterized cells subjected to pharmacological inhibition of MMP secretion, and observed a significant decrease in intensity in our assay (Figure 5-10). The expected effect of secretion inhibitors monensin and brefeldin is downregulation of MMP secretion. Prostate cancer cells PC3 that were encapsulated into droplets containing the drug cocktail (eBioscience 004980-003) show significant decrease in fluorescence intensity within droplets. We observe a 40% decrease in the median intensity from untreated to treated cells.

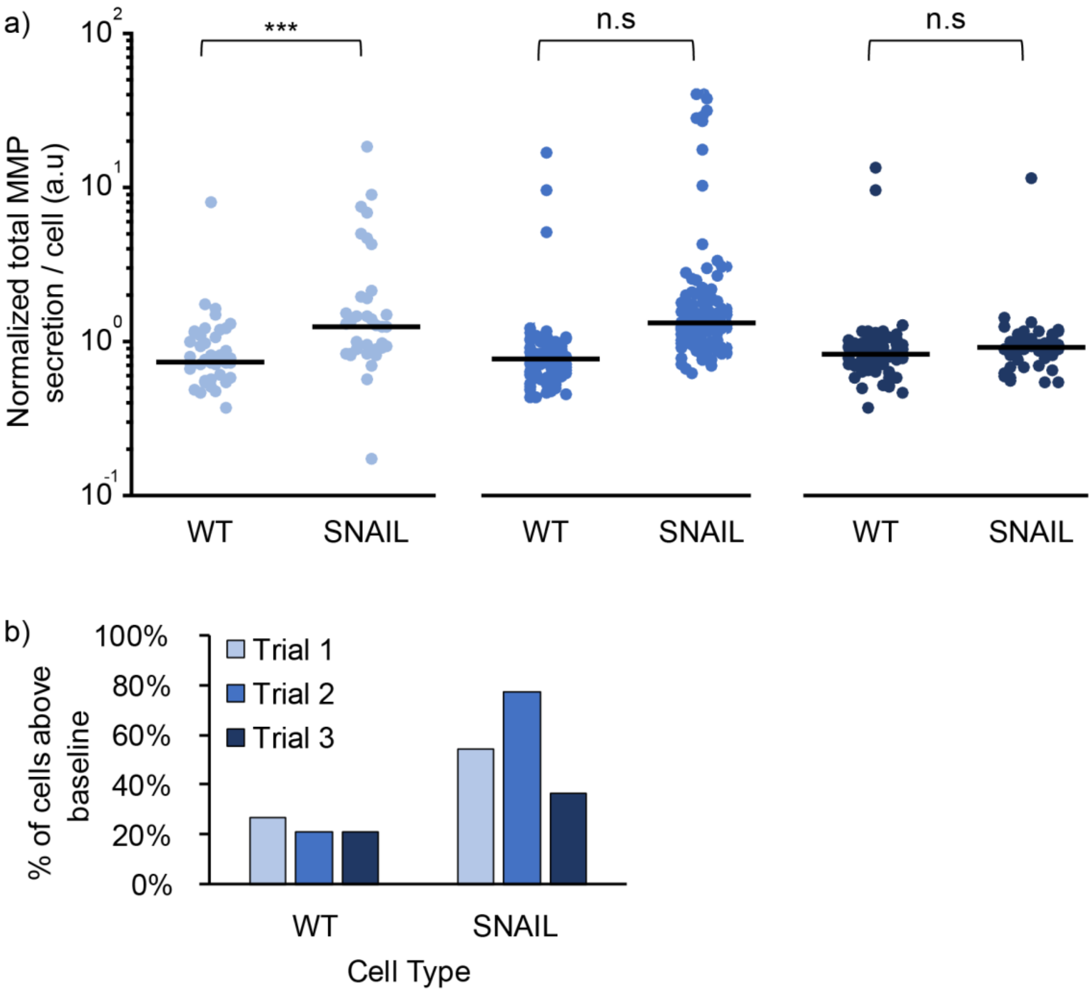

**Figure 5-9**. a) We studied the effects on MMP9 and broad spectrum MMP secretion in wild-type A549 lung cancer cells (WT) and A549 cells overexpressing SNAIL, a transcription factor involved in epithelial to mesenchymal transition (EMT). There is a significant increase in signal from a peptide substrate cleaved by a broad spectrum of MMPs in SNAIL overexpressing cells, indicating these cells secrete higher levels of MMPs, although not MMP9. b) Percentage of SNAIL overexpressing cells secreting above baseline levels of MMP-9 is higher than the percentage of wild-type cells secreting above baseline levels.

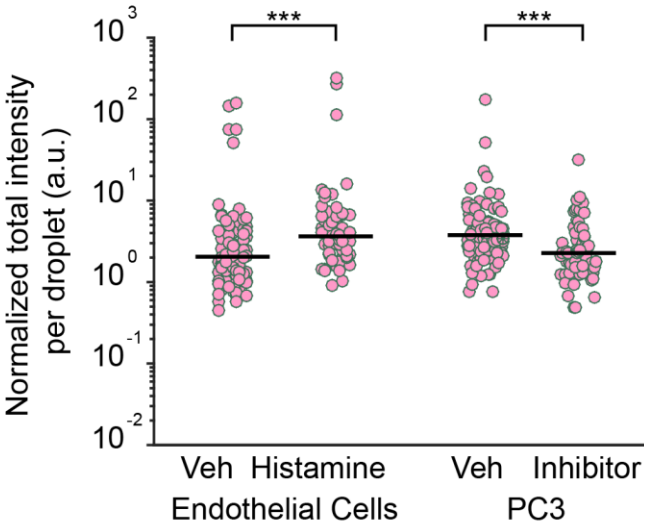

**Figure 5-10**. The assay can correctly detect modulation of MMP secretion from cells. Histamine is shown to upregulate MMP secretion when exposed to endothelial cells . PC3 prostate cancer cells were exposed to secretion inhibitors brefeldin and monensin. These drugs together sequester proteins in the golgi apparatus and prevent them from being secreted. As expected, there is a decrease in measured secretion in the presence of the inhibitors. *** $p < 0.001$.

### 5.3.5. Circulating tumor cells from prostate cancer patients secrete MMPs

We processed samples from seven metastatic castration resistant prostate cancer patients. Six out of seven patient samples contained CTCs; and 87% of these CTCs secreted MMPs, leading to fluorescence signals above baseline (Figure 5-11). One sample which contained no CTCs, corresponded with clinical results of no new metastasis (Patient 1). Patients with lower levels of PSA (Patients 2 and 4) and in a state of response to treatment (Patient 3) had CTCs that generally were found to secrete lower levels MMPs. Samples from patients with radiographic progression to the bone and lymph node correlated with the highest levels of CTC secreted MMPs in the cohort (Patients 6 and 7). These patients also had the highest levels of PSA as well (Table 5-1).

In addition to secretion from CTCs, leukocytes and clusters of RBCs and non-nucleated components obtained from blood of cancer patients, but not healthy patients, were found to secrete comparable amounts of MMPs to CTCs. As for cell lines and CTCs, population level behavior appears to be dominated by few high secreting cells. We also see a positive correlation between the highest levels of MMPs secreted by CTCs and the MMPs secreted by the same patient’s WBCs and ECs. This may indicate that there are patient-dependent baseline differences in MMP secretion levels, or overall inflammation is increased in highly metastatic patients, leading to higher levels of leukocyte MMP secretion.

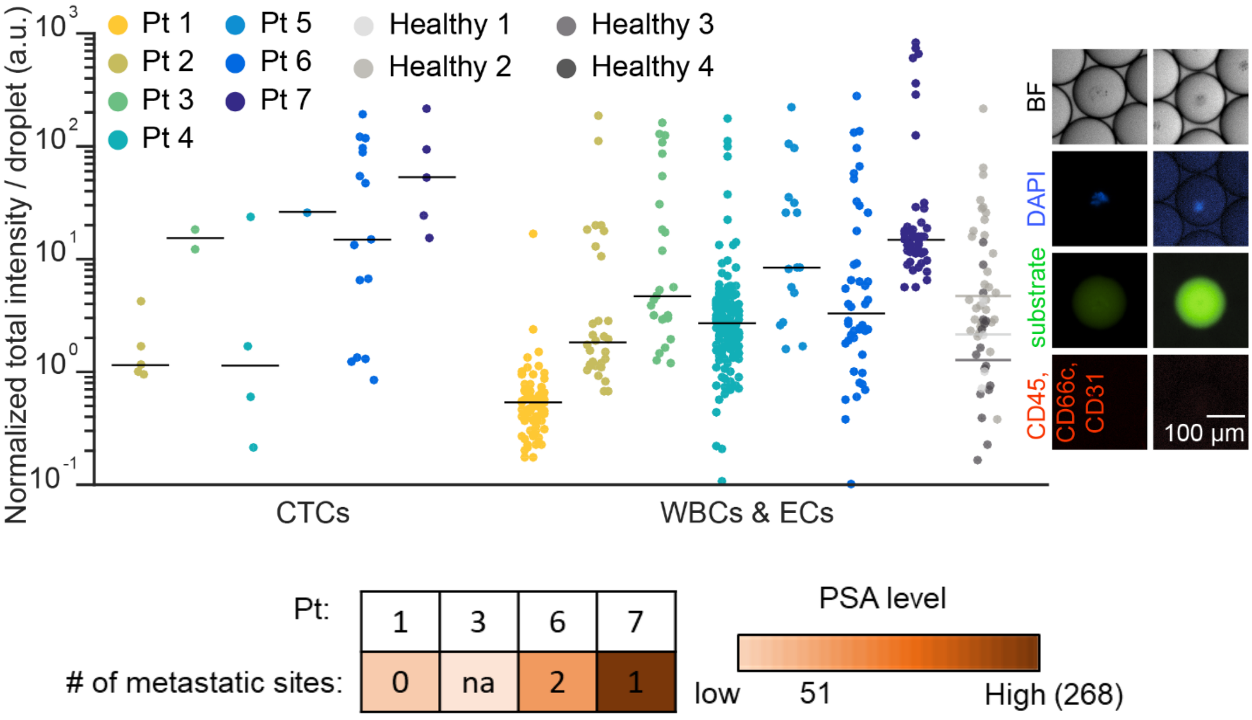

| Pt: | 1 | 3 | 6 | 7 |
|---|---|---|---|---|
| # of metastatic sites: | 0 | na | 2 | 1 |

**Figure 5-11**. Blood samples from prostate cancer patients and healthy volunteers were processed to determine MMP secretion levels from single cells. Cells that are negative for CD31 and CD45, positive for PSMA or had a large nucleus were classified as CTCs. Six out of seven patient samples were observed to have CTCs. Each of these samples had CTCs with above background levels of MMP secretion. WBCs and ECs from prostate cancer patient samples secrete more MMPs than WBCs and ECs from healthy samples. The sample with the lowest level of MMP secretion in WBCs and EC (Pt 1) had no CTCs and corresponded to a patient with no new metastases or radiographic progression. Patients with CTCs with a high range of MMP secretion that is over two orders of magnitude above baseline also had higher levels of PSA.

| Patients ID ranked from MMP level low to high | Clinical Information | PSA | Additional # of metastasis |
|---|---|---|---|
| 1 | No new metastases | 8.8 | 0 |
| 2 | Radiographic progression,<br>BET inhibitor ~3 wks prior to blood draw | N/A | N/A |
| 3 | Radiographic progression. PSA increasing but relatively low (lower PSA value may represent a more poorly differentiated cancer)<br>Germline BRCA2 mutation | low | N/A |
| 4 | State of response to treatment | N/A | N/A |
| 5 | Rising PSA and radiographic progression | N/A | N/A |
| 6 | Radiographic progression in bones and lymph nodes | 50.8 | 2 |
| 7 | Radiographic progression in bones | 267.7 | 1 |

**Table 5-1**. Blood samples from seven prostate cancer patients were assayed. The clinical state of each patient is reported here. The orange shades represent the levels of PSA. The patients samples containing CTCs with the highest level of MMP secretion also had the highest amounts of PSA.

## 5.4. Discussion

The SPEC platform has the ability to purify cancer cells from large volumes of blood in a high throughput manner, wash these captured cells, exchange solutions around them, and encapsulate them into microdroplets all in one integrated device. Our hands-free process allows for a seamless transition of cells to droplets, unlike current available tools. This proof of concept device enabled a single cell resolution assay for MMP secretion by living CTCs and other circulating cells from prostate cancer samples.

CTCs, leukocytes and cancer cell lines were all found to have a wide range of MMP secretion, with high secreting outlier cells. Inflamed leukocytes secrete MMPs at the site of inflammation. These cells often help other T-cells to enter the tumor site, or conversely certain signal pathways can inhibit T-cell proliferation.[5] These behaviors may explain why some subsets of WBCs and ECs from patient samples have high secreting MMPs compared to WBCs and ECs from healthy samples. For cultured cells, by performing cell cycle synchronization to quiescent G0 phase (via serum starvation) – we were able to reduce the amount of MMP secretion and induce a higher level of homogeneity in secretion. Cellular activity decreases during the G0 phase, thus secretory function becomes minimal on the majority of cells. However, other types of cell cycle synchronization did not show the same results- when the cells were synchronized to M phase through use of STLC (S-Trityl-L-Cysteine) or S phase through double thymidine block. Following treatment, we observed the same heterogeneous secretion as control groups. The gini coefficient remained the same. These results indicate that cell cycle may not be a major contributing factor to MMP secretion heterogeneity. Importantly, we found the heterogeneity appeared only when cells were used, and it was not inherent to the assay (Figure 5-12b). Such high MMP-secreting outlier cells would be of interest to select and better understand transcriptomic, and phenotypic differences in future studies on metastasis.

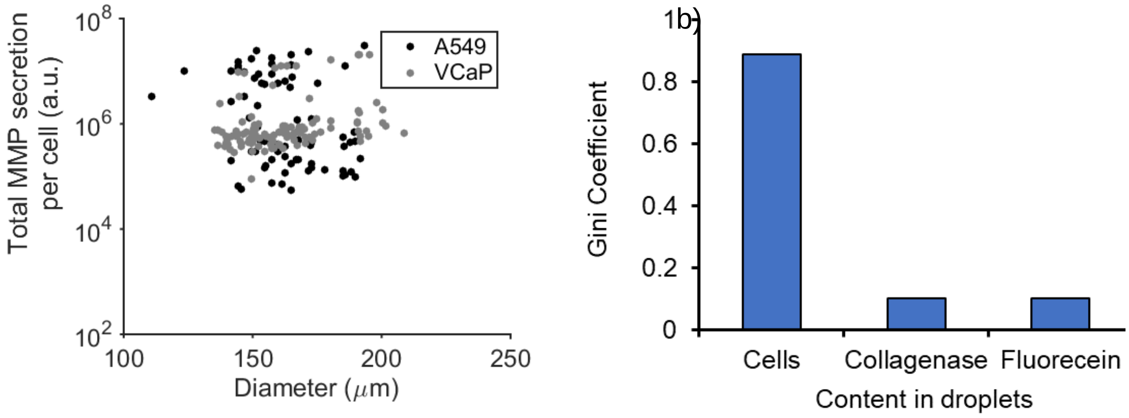

**Figure 5-12**. a) There is no correlation between the diameter of the droplets with cells and the fluorescent intensity. The observed heterogeneity is inherent to the cells and not the assay. b) The dispersion in signal intensity observed decreases as the content used to generate the signal becomes more controllable. Here we quantify the dispersion with the Gini coefficient. The signal from the A549 cells has a higher heterogeneity than that from droplets loaded with collagenase or fluorescein. This controlled experiment shows that the heterogeneity we observe is due to the cells and not the parameters of the assay.

Our initial clinical results show that all nucleated cells and platelets isolated from blood secrete above background levels of MMPs (Figure 5-13). A large majority of platelets from clinical samples secrete more MMPs than healthy samples. As previous studies have shown, platelets secrete different forms of MMPs, and these relate to platelet aggregation.[48] These results indicate that cellular components of blood other than CTCs may also be of interest in studying the mechanism of metastasis. In addition, future investigation that further differentiates between MMP subtypes may be warranted in further elucidating the invasive phenotype of CTCs. Applying this technology to study subcategories of specific MMPs and other cancer specific proteases such as Cathepsin D may be useful. Currently we are limited by the number of FRET peptide probes. New synthesis approaches for cleavable peptides will enable even better understanding of the metastatic process and development of anti-metastasis drugs.

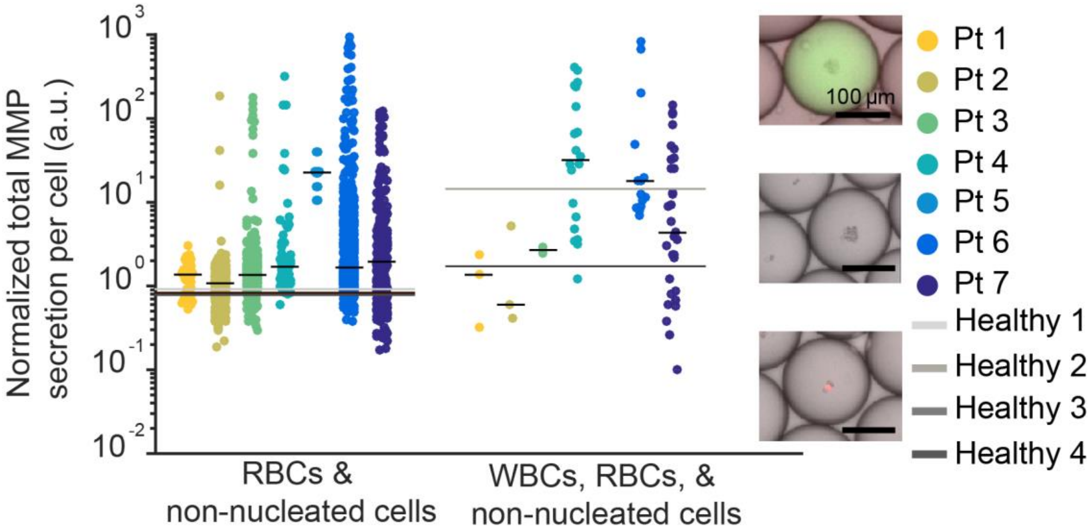

**Figure 5-13**. In addition to CTCs and WBCs a number of RBCs and non-nucleated cells (which may be clusters of platelets) were trapped droplets due to a small amount of dead volume in the connections to the pinch valve. These cells and other blood components secrete higher levels of MMP than the median level of MMP from the same type of cells in healthy samples.

## 5.5. Conclusion

We have demonstrated the use of SPEC – a novel, integrated device for cell purification and encapsulation as a single cell protease secretion assay. Using this technology, we were able to measure matrix metalloprotease secretion of CTCs at single cell resolution. The secretory phenotype of these cells in prostate cancer patients has not been studied in detail until now. Our results indicate that the majority of CTCs actively secrete MMPs, over a range that spans orders of magnitudes. This is the first time such a measurement has been done. We validate a long standing hypothesis that CTCs may use MMPs in their  secretion may be a mechanism of metastasis. Furthermore, initial results suggest a correlation between the MMP secretion and PSA level in patients. Leukocytes and clusters of platelets also secrete MMPs at varying levels in these cancer patients which may be similarly diagnostically important. A larger clinical study and multiplexing of analysis of multiple protease secretions can give more information on how proteases can be used for diagnostic and prognostic purposes. Ultimately, phenotypic liquid biopsies, such as those assaying protease secretions or cell deformability can provide more detailed clinical information and directly inform the use of anti-metastatic / anti-invasive therapies targeting hallmarks of invasive tumor phenotypes.

## 5.6. References

1. Groblewska, M. *et al.* Serum levels and tissue expression of matrix metalloproteinase 2 (MMP-2) and tissue inhibitor of metalloproteinases 2 (TIMP-2) in colorectal cancer patients. *Tumour Biol.* 35, 3793–802 (2014).
2. Upadhyay, J. *et al.* Membrane type 1-matrix metalloproteinase (MT1-MMP) and MMP-2 immunolocalization in human prostate: change in cellular localization associated with high-grade prostatic intraepithelial neoplasia. *Clin. Cancer Res.* 5, 4105–10 (1999).
3. Zhang, B. *et al.* Tumor-derived matrix metalloproteinase-13 (MMP-13) correlates with poor prognoses of invasive breast cancer. *BMC Cancer* 8, 83 (2008).
4. Kallakury, B. V *et al.* Increased expression of matrix metalloproteinases 2 and 9 and tissue inhibitors of metalloproteinases 1 and 2 correlate with poor prognostic variables in renal cell carcinoma. *Clin. Cancer Res.* 7, 3113–9 (2001).
5. Egeblad, M. & Werb, Z. New functions for the matrix metalloproteinases in cancer progression. *Nat. Rev. Cancer* 2, 161–174 (2002).
6. Aalinkeel, R. *et al.* Overexpression of MMP-9 Contributes to Invasiveness of Prostate Cancer Cell Line LNCaP. *Immunol. Invest.* 40, 447–464 (2011).
7. Tse, H. T. K. *et al.* Quantitative Diagnosis of Malignant Pleural Effusions by Single-Cell Mechanophenotyping. *Sci. Transl. Med.* 5, (2013).
8. Che, J. *et al.* Biophysical isolation and identification of circulating tumor cells. *Lab*

*Chip* 17, 1452–1461 (2017).

9. Brehmer, B., Biesterfeld, S. & Jakse, G. Expression of matrix metalloproteinases (MMP-2 and -9) and their inhibitors (TIMP-1 and -2) in prostate cancer tissue. *Prostate Cancer Prostatic Dis. Publ. online 01 Sept. 2003;* | *doi10.1038/sj.pcan.4500657* 6, 217 (2003).
10. Gondi, C. S. & Rao, J. S. Cathepsin B as a cancer target. *Expert Opin. Ther. Targets* 17, 281–91 (2013).
11. Westermarck, J. & Kähäri, V. M. Regulation of matrix metalloproteinase expression in tumor invasion. *FASEB J.* 13, 781–92 (1999).
12. Safranek, J. *et al.* Expression of MMP-7, MMP-9, TIMP-1 and TIMP-2 mRNA in lung tissue of patients with non-small cell lung cancer (NSCLC) and benign pulmonary disease. *Anticancer Res.* 29, 2513–2517 (2009).
13. Kim, Y. H., Kwon, H.-J. & Kim, D.-S. Matrix metalloproteinase 9 (MMP-9)-dependent processing of βig-h3 protein regulates cell migration, invasion, and adhesion. *J. Biol. Chem.* 287, 38957–69 (2012).
14. Manish A. Shah, Alexander Starodub, Zev A. Wainberg, Meihua Wu, Victoria Smith, Julia D. Maltzman, J. C. B. Results of a phase I study of GS-5745 in combination with mFOLFOX in patients with advanced unresectable gastric / GE junction tumors. ASCO Annual Meeting. Abstracts.(2016).
15. Marshall, D. C. *et al.* Selective Allosteric Inhibition of MMP9 Is Efficacious in Preclinical Models of Ulcerative Colitis and Colorectal Cancer. *PLoS One* 10,

e0127063 (2015).

16. Cristofanilli, M. *et al.* Circulating tumor cells: a novel prognostic factor for newly diagnosed metastatic breast cancer. *J. Clin. Oncol.* 23, 1420–30 (2005).
17. Pierga, J.-Y. *et al.* Circulating Tumor Cell Detection Predicts Early Metastatic Relapse After Neoadjuvant Chemotherapy in Large Operable and Locally Advanced Breast Cancer in a Phase II Randomized Trial. *Clin. Cancer Res.* 14, 7004–7010 (2008).
18. Danila, D. C. *et al.* Circulating Tumor Cell Number and Prognosis in Progressive Castration-Resistant Prostate Cancer. *Clin. Cancer Res.* 13, 7053–7058 (2007).
19. Galletti, G. *et al.* Circulating tumor cells in prostate cancer diagnosis and monitoring: an appraisal of clinical potential. *Mol. Diagn. Ther.* 18, 389–402 (2014).
20. Liu, J. F. *et al.* Predictive value of circulating tumor cells (CTCs) in newly-diagnosed and recurrent ovarian cancer patients. (2013). doi:10.1016/j.ygyno.2013.08.006
21. Park, E. S. *et al.* Continuous Flow Deformability-Based Separation of Circulating Tumor Cells Using Microfluidic Ratchets. *Small* 12, 1909–1919 (2016).
22. Yamanaka, Y. J. *et al.* Single-cell analysis of the dynamics and functional outcomes of interactions between human natural killer cells and target cells. *Integr. Biol.* 4, 1175 (2012).
23. Torres, A. J., Hill, A. S. & Love, J. C. Nanowell-based immunoassays for

measuring single-cell secretion: characterization of transport and surface binding. *Anal. Chem.* 86, 11562–9 (2014).

24. Yao, G. Modelling mammalian cellular quiescence. *Interface Focus* 4, 20130074 (2014).

25. Jing, T. *et al.* Jetting micro fl uidics with size-sorting capability for single-cell protease detection. *Biosens. Bioelectron.* 66, 19–23 (2015).

26. Jing, T. *et al.* Single Cell Analysis of Leukocyte Protease Activity Using Integrated Continuous-Flow Microfluidics. *Anal. Chem.* 88, 11750–11757 (2016).

27. Abatemarco, J. *et al.* RNA-aptamers-in-droplets (RAPID) high-throughput screening for secretory phenotypes. *Nat. Commun.* 8, 332 (2017).

28. Mazutis, L. *et al.* Single-cell analysis and sorting using droplet-based microfluidics. *Nat. Protoc.* 8, 870–91 (2013).

29. Peters, C. E., Woodside, S. M. & Eaves, A. C. in *Handbook of ELISPOT* 095–116 (Humana Press, 2005). doi:10.1385/1-59259-903-6:095

30. Schwanhäusser, B. *et al.* Global quantification of mammalian gene expression control. *Nature* 473, 337–342 (2011).

31. Stone, Z. N. and M. S. and S. X. and P. C. L. and M. M. and E. K. and G. M. W. and P. G. and H. A. Emulsification in a microfluidic flow-focusing device: effect of the viscosities of the liquids. *Microfluid. Nanofluid.* 585--594 (2008).

32. Garstecki, P., Fuerstman, M. J., Stone, H. A. & Whitesides, G. M. Formation of

droplets and bubbles in a microfluidic T-junction-scaling and mechanism of break-up. *Lab Chip* 6, 437–46 (2006).

33. Riche, C. T., Roberts, E. J., Gupta, M., Brutchey, R. L. & Malmstadt, N. Flow invariant droplet formation for stable parallel microreactors. *Nat. Commun.* 7, 10780 (2016).
34. Dangla, R., Kayi, S. C. & Baroud, C. N. Droplet microfluidics driven by gradients of confinement. *Proc. Natl. Acad. Sci.* 110, 853–858 (2013).
35. Ng, E. X., Miller, M. A., Jing, T. & Chen, C.-H. Single cell multiplexed assay for proteolytic activity using droplet microfluidics. *Biosens. Bioelectron.* 81, 408–414 (2016).
36. JING, T. *et al.* Single Cell Analysis of Leukocyte Protease Activity using Integrated Continuous-Flow Microfluidics. *Anal. Chem.* acs.analchem.6b03370 (2016). doi:10.1021/acs.analchem.6b03370
37. Haddadi, H. & Di Carlo, D. Inertial flow of a dilute suspension over cavities in a microchannel. *J. Fluid Mech.* 811, 436–467 (2017).
38. Kurtz, S. M. *UHMWPE Biomaterials Handbook: Ultra High Molecular Weight Polyethylene in Total Joint Replacement and Medical Devices*. (Elsevier, 2015).
39. Matsushita, O., Yoshihara, K., Katayama, S., Minami, J. & Okabe, A. Purification and characterization of Clostridium perfringens 120-kilodalton collagenase and nucleotide sequence of the corresponding gene. *J. Bacteriol.* 176, 149–56 (1994).

40. Ries, C. *et al.* MMP-2, MT1-MMP, and TIMP-2 are essential for the invasive capacity of human mesenchymal stem cells: differential regulation by inflammatory cytokines. *Blood* 109, (2007).

41. Tian, T. V *et al.* Identification of novel TMPRSS2:ERG mechanisms in prostate cancer metastasis: involvement of MMP9 and PLXNA2. *Oncogene* 33, 2204–2214 (2014).

42. Atkinson, J. M. *et al.* Membrane type matrix metalloproteinases (MMPs) show differential expression in non-small cell lung cancer (NSCLC) compared to normal lung: Correlation of MMP-14 mRNA expression and proteolytic activity. *Eur. J. Cancer* 43, 1764–1771 (2007).

43. Ramanujum, R., Lin, Y., Liu, J. & He, S. Regulatory expression of MMP-8/MMP-9 and inhibition of proliferation, migration and invasion in human lung cancer A549 cells in the presence of HGF variants. *Kaohsiung J. Med. Sci.* 29, 530–9 (2013).

44. Kiran, M. S., Viji, R. I., Kumar, S. V., Prabhakaran, A. A. & Sudhakaran, P. R. Changes in expression of VE-cadherin and MMPs in endothelial cells: Implications for angiogenesis. *Vasc. Cell* 3, 6 (2011).

45. Lin, C.-Y. *et al.* Matrix metalloproteinase-9 cooperates with transcription factor Snail to induce epithelial-mesenchymal transition. *Cancer Sci.* 102, 815–827 (2011).

46. Jin, H. *et al.* Snail is critical for tumor growth and metastasis of ovarian carcinoma. *Int. J. Cancer* 126, n/a-n/a (2009).

47. Doyle, J. L. & Haas, T. L. Differential role of β-catenin in VEGF and histamine-induced MMP-2 production in microvascular endothelial cells. *J. Cell. Biochem.* 107, 272–283 (2009).

48. Kazes, I., Elalamy, I., Sraer, J. D., Hatmi, M. & Nguyen, G. Platelet release of trimolecular complex components MT1-MMP/TIMP2/MMP2: involvement in MMP2 activation and platelet aggregation. *Blood* 96, 3064–3069 (2000).

49. Dhar, M. *et al.* High efficiency vortex trapping of circulating tumor cells. *Biomicrofluidics* 9, 64116 (2015).

# Chapter 6. In-Flow Cell Modification

## 6.1. Single cell DNA amplification

Our studies of the protein expression on CTCs has shown the dominating behavior of outlier cells, which is similarly important when looking at genomic mutations. Investigating the underlying genomic heterogeneity, and preventing loss of signal from rare sub-populations is important for improved companion diagnostics and biological understanding in cancer. In order to conduct experiments demonstrating the genomic diversity in rare CTCs, we must distinguish the mutational profile from each CTC. Currently techniques that uniquely barcodes cells for sequencing are DropSeq, inDrop and Seq-Well.[93–95] Here cells are co-encapsulated with oligo-barcoded beads or hydrogels in droplets and cell lysis agents. Alternatively, the unique barcodes are contained in individual nanowells for the Seq-Well platform. During amplification, target amplicons from each cell gets barcoded with a unique sequence.[93–96] The DropSeq method can successfully barcode 2-4% of the cells and inDrop can barcode 75% of thousands to tens of thousands of cells. Due to large number of starting volume of cells necessary, barcoding methods are not amenable for use with rare cells. There is a high probability many of the droplets with CTCs will not have a barcoded bead.

We address the challenge of preserving CTC heterogeneity in genomic studies by pre-processing cells trapped in vortices and keeping them spatially segregated in droplets during amplification. We adapt the assay presented in Chapter V to process cells for genomic amplification.

## 6.2. Gaining access to the DNA within a cell

In order to gain access to the DNA of a cell, we must permeabilize the cells. The parameters necessary to sufficiently permeabilize cells and remove contaminating proteins to enable DNA amplification involve removing proteins, lipids and carbohydrates from the cell and nuclear membrane. Detergents break the lipid barrier surrounding cells by solubilizing proteins and disrupting lipid:lipid, protein:protein and protein:lipid interactions. Enzymes such as proteinase-K degrades DNase, RNase and histones. DNase can degrade the amplicons and are therefore important to remove.[97] Histones condense DNA into packed chromatins, its degradation is necessary to access portions of the DNA.[98] In addition to removing proteins, past work on in-cell PCR has shown the necessity to fix cells in order to allow polymerases to enter the cell.[99–101] We find that aspects of cell permeabilization and protein degradation can be achieved in microvortices while cells are trapped in flow.

After cell capture in vortices, we introduce detergents, enzymes and paraformaldehyde to permeabilize and fix the cells in flow. The strong mixing action of the vortex coupled with surfactants aid in removing lipids and proteins from the cell and nuclear membrane. This is evidenced by the loss of contrast of cells in vortices treated with surfactant mixture (Figure 6-1), while cell “ghosts” remain stably orbiting. We investigate what ratios of surfactants (SDS, Triton-X100) and enzymes (Proteinase K) are required to have sufficient accessibility for primers and polymerases to initiate amplification. We perform a solution exchange on the vortex chip with the wash/permeabilization buffer, then the amplification buffer followed by lowering the flow rate to collect treated cells for a bulk reaction.

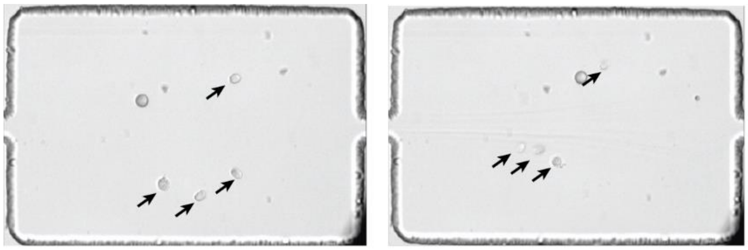

Cells trapped in Vortex

Cells remain trapped after 11 seconds in RIPA buffer

**Figure 6-1**. Solution exchange in vortices allows for rapid and complete fluid exchange. Exchange with lysis buffer results in maintenance of permeabilized cells.

The degree of permeabilization down to the nuclear membrane is characterized using DNA intercalating dye EvaGreen. Figure 6-2 shows the mean intensity of EvaGreen in the PC3 cells increases as we apply concentrations of reagents. We find that proteinase-K is a harsh reagent that completely lyses a cell in-flow within 10 seconds if used at higher than 0.6% concentration.

We were also able to detect cell fixation using DAPI. DAPI selectively attaches to A-T rich regions of the DNA. Because has a larger molecular mass than EvaGreen, it is able to efficiently pass through the cell membrane of fixed cells, and less efficiently stain live cells. We found DAPI successfully stains the nucleus of cells fixed with PFA in flow trapped in the vortex device. Cells treated with no PFA and just PBS were not able to stain the nucleus.

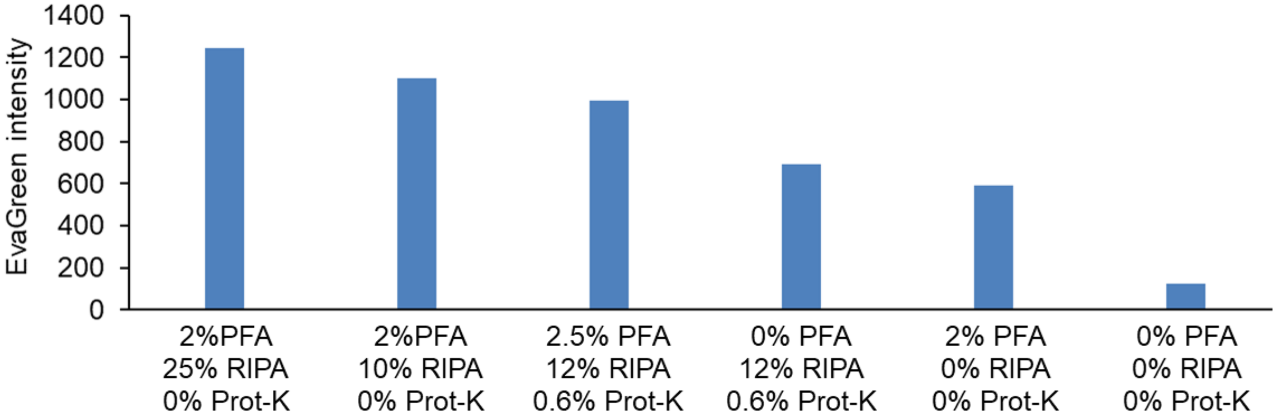

**Figure 6-2**. Intensity of EvaGreen shows the amount of dye that was able to enter the nucleus of the cell when treated with various reagents. The cells maintain their orbits in the vortex during solution exchange with reagents of different viscosities.

For the first time we have shown that cells in-flow can be permeabilized and fixed within a few minutes using several different types of reagents. We are able to leverage the shear forces from the vortex mixing to speed up this process that usually takes several minutes in a well plate. Even after treating the cells with several buffers, the cells maintain their orbit within the vortex, allowing us to release them into droplets for further processing. This method of in-flow cell permeabilization and fixation is a first step towards performing in drop CTC mutational analysis.

## 6.3. References

1. Macosko, E. Z. *et al.* Highly parallel genome-wide expression profiling of individual cells using nanoliter droplets. *Cell* 161, 1202–1214 (2015).

2. Zilionis, R. *et al.* Single-cell barcoding and sequencing using droplet microfluidics. *Nat. Protoc.* 12, 44–73 (2016).

3. Gierahn, T. M. *et al.* Seq-Well: portable, low-cost RNA sequencing of single cells at high throughput. *Nat. Methods* 14, 395–398 (2017).

4. Rotem, A. *et al.* High-throughput single-cell labeling (Hi-SCL) for RNA-Seq using drop-based microfluidics. *PLoS One* 10, 1–14 (2015).

5. Amidzadeh, Z. *et al.* Assessment of different permeabilization methods of minimizing damage to the adherent cells for detection of intracellular RNA by flow cytometry. *Avicenna J. Med. Biotechnol.* 6, 38–46 (2014).

6. Massion, P. P., Sequist, L. V. & Pao, W. in *Murray and Nadel's Textbook of Respiratory Medicine* 912–926.e6 (Elsevier, 2016). doi:10.1016/B978-1-4557-3383-5.00051-8

7. Bagasra, O. Protocols for the in situ PCR-amplification and detection of mRNA and DNA sequences. *Nat. Protoc.* 2, 2782–2795 (2007).

8. Testoni, N. *et al.* A New Method of &quot; In-Cell Reverse Transcriptase-Polymerase Chain Reaction &quot; for the Detection of BCRIABL Transcript in Chronic Myeloid Leukemia Patients.

9. Larsson, C. *et al.* In situ genotyping individual DNA molecules by target-primed rolling-circle amplification of padlock probes. *Nat. Methods* 1, 227–32 (2004).

# Chapter 7. Concluding Remarks

The phenotypic analysis of CTCs gives us much more information for prognosis beyond CTC enumeration. The technology developed here enables such analysis and demonstrates the power of automation and label-free cell sorting. The high throughput nature of the Vortex technology allows us to process large volumes of blood to quickly purify and concentrate CTCs. The label-free nature of the method allows for facile integration with downstream analysis of live cells. We show the clinically utility of CTCs using immunofluorescence analysis of surface protein expression and live cell function of protease secretion.

We have explored several clinical applications of CTCs. CTCs can be clinically useful in determining the range of PD-L1 expression for cancer immunotherapy screenings. The expression profiles of CTCs can potentially aide in determining a response to treatment.

Going beyond static protein expression, using the integrated assay SPEC, we were able to measure matrix metalloprotease secretion of CTCs at single cell resolution. The enzymatic behavior of these cells has not been studied in detail until now. For the first time we are able to prove that CTCs actively secrete a range of levels of MMPs. Leukocytes and clusters of platelets also secrete MMPs at varying levels in patients which may be diagnostically important. In the future applying this technology to study subcategories of specific MMPs and other cancer specific proteases such as Cathepsin D will be useful. Currently we are limited by the number of FRET based peptides. New synthesis of cleavable peptides will enable even better understanding of the metastatic process and development of anti-metastasis drugs.

We see the device described here as a platform technology that will be used for several assays. We have been able to use the solution exchange mechanism to introduce cell permeabilization and fixation reagents. These reagents are able to quickly permeabilize and fix cells that are trapped in the vortex. After treatment with low concentrations of these buffers, the cells maintain their orbit in the vortex. This process allows us to continue to exchange solution around the cell with other reaction mix for PCR or LAMP reaction and release them into well plates or droplets for incubation.

The applications of this platform can be extended beyond broad spectrum MMPs. Studying secretions from CTCs and leukocytes at a single cell level has revealed that both cell types secrete MMPs. We can now use this platform to study specific subsets of proteases that may be more prone to be secreted from CTCs rather than leukocytes. We can compare the secretion levels from CTCs to that from bulk tumor samples to aid in patient specific protease inhibitors. Eventually a multiplexed assay that differentiate between various types of proteases secreted from one cell may be the most informative study.

As we further characterize cells isolated from blood and differentiate them from healthy cells, we will need to continue moving beyond static immunofluorescence staining. The SPEC platform can enable monitoring single cell behaviors such metabolic activity through fluorometric enzymatic lactate and glucose sensors in drop. The driving factor here is tumor cells are known to have higher metabolic activity than healthy cells.

Single cell functional studies of cells add to our understanding of physiologic conditions. The tools described here can contribute to clinically relevant discoveries of cell behaviors and help clinicians make more informative decisions about personalized drug treatments.